

**CHARACTERIZATION OF VACANCY-TYPE DEFECTS IN SILICON AND  
THE APPLICATIONS TO PHOTONIC DEVICES**

**CHARACTERIZATION OF VACANCY-TYPE DEFECTS IN SILICON AND  
THE APPLICATIONS TO PHOTONIC DEVICES**

By  
PHILIP J. FOSTER, BSCE

A Thesis  
Submitted to the School of Graduate Studies  
in Partial Fulfillment of the Requirements  
for the Degree  
Master of Applied Science

McMaster University  
©Copyright by Philip J. Foster, 2005.

MASTER OF APPLIED SCIENCE (2005)  
(Engineering Physics)

McMaster University  
Hamilton, Ontario

TITLE: Characterization of Vacancy-Type Defects in Silicon and the Applications to  
Photonic Devices

AUTHOR: Philip J. Foster, BSCE (Queen's University, 2002)

SUPERVISORS: Prof. Andrew P. Knights and Prof. Peter Mascher

NUMBER OF PAGES: ix, 123

## Abstract

The excess optical attenuation at wavelengths around  $1.55\mu\text{m}$  induced by ion-irradiation of silicon-on-insulator rib waveguides was quantified. After  $2.8\text{MeV Si}^+$  implantation at a dose of  $6.3 \times 10^{13}\text{cm}^{-2}$ , the measured optical loss was  $430 \pm 15\text{dBcm}^{-1}$ , suggesting that selective implantation of a relatively low dose of inert ions provides a method for modal attenuation in silicon photonic circuits. This is particularly useful for reducing optical noise or crosstalk between devices integrated on the same substrate. It was concluded that this attenuation was related to the introduction of lattice defects, predominantly silicon divacancies, caused by the implantation. Fourier transform infrared spectroscopy measurements confirmed the  $1.8\mu\text{m}$  absorption band previously correlated to divacancies in silicon. Positron lifetime measurements of bulk silicon implanted with  $1.5\text{MeV H}^+$  indicated that divacancies are the dominant vacancy-type defect present. These measurements required the development of a new model for the implantation profile of positrons emitted from  $^{22}\text{Na}$ . This model was based on the theory of  $\beta^+$  decay in conjunction with Gaussian derivative distributions developed by Makhov. Beam-based positron annihilation spectroscopy was used to measure the divacancy concentration in bulk silicon also implanted with  $2.8\text{MeV Si}^+$ . This resulted in excellent agreement with an empirical model, developed by Coleman, Burrows and Knights (CBK), which has been used previously to predict vacancy-type defect concentrations in

bulk silicon for various implantation conditions. Based on the CBK model, a simple analytical expression that can be used to estimate excess optical absorption in ion implanted silicon was suggested. This expression predicts absorption of  $282\text{dBcm}^{-1}$  for  $2.8\text{MeV Si}^+$  implantation at a dose of  $6.3 \times 10^{13}\text{cm}^{-2}$ , considerably less than the measured attenuation in the irradiated waveguides. Reasons for this discrepancy are discussed and it was concluded that considerable attenuation is associated with radiation loss due to the implantation-induced refractive index modification in the waveguides. This radiation loss, which is not accounted for in the predictive analytical expression based on the CBK model, was verified using BeamProp simulations. Finally, it was demonstrated how implantation damage could be utilized to fabricate an integrated optical barrier. It was shown that a  $10\text{dB}$  barrier with a width of  $1000\mu\text{m}$  could be made with an implantation dose two orders of magnitude lower than that required for a barrier made using free carrier absorption.

# Acknowledgements

I would like to take this opportunity to express my appreciation to those who have helped and contributed to the success of this project. First and foremost, I'd like to thank both Dr. Peter Mascher and Dr. Andrew Knights for giving me the opportunity to take on this work, which turned out to be an enjoyable and invaluable experience.

I would also like to acknowledge the staff of the Centre for Electro-phonic Materials and Devices (CEMD) at McMaster University, in particular Doug Bruce and Doris Stevanovic, for their assistance in the waveguide device fabrication. Members of Interface Science Western at the University of Western Ontario, and Jack Hendricks in particular, must be mentioned for their crucial assistance with the ion implantation. Furthermore, the University of Bath U.K. and Paul Coleman should be recognized for performing the positron beam measurements.

All of my colleagues in the Engineering Physics department have been accommodating, especially Andrew Younker, Jon Bradley, and Joel Milgram, who each have been tremendously helpful with my work as well as great friends. These people really made this an entertaining and memorable experience.

Finally, much credit must go to my parents, who have always been there for support when I needed it. I cannot thank them enough for what they have done for me throughout my time here.

# Contents

<b>List of Figures</b>	<b>viii</b>
<b>1 Introduction</b>	<b>1</b>
1.1 Siliconizing Photonics	1
1.2 Defect-Engineering in Silicon Photonics	3
1.3 Objectives of this Work	5
<b>2 Background and Theory</b>	<b>9</b>
2.1 Light in Bulk Media	9
2.1.1 Wave Propagation	9
2.1.2 Refractive Index	11
2.1.3 Absorption	13
2.1.4 Scattering	17
2.2 Guided Wave Theory	18
2.2.1 Reflection and Refraction	19
2.2.2 Planar Waveguides	21
2.2.3 Rib Waveguides and the Effective Index Method	25
2.2.4 Mode Profiles and the Beam Propagation Method	28
2.3 Attenuation in Semiconductor Waveguides	32
2.3.1 Absorption	32
2.3.2 Scattering	33
2.3.3 Radiation	34
2.4 Ion Implantation Damage in Silicon	37
2.4.1 Ion Stopping Profile	38
2.4.2 Vacancy-Type Defects	40
2.4.3 Defect Accumulation	40
2.4.4 Influence of Implantation Parameters	44
2.4.5 Post-Implantation Annealing	46
2.5 Optical Properties of Damaged Silicon	47
2.5.1 Deep Levels Associated with the Silicon Divacancy	48
2.5.2 The 1.8 $\mu$ m Absorption Band	50
2.5.3 Implantation-Induced Index Modification	51

<b>3</b>	<b>Characterization of Implantation-Induced Defects in Silicon .....</b>	<b>52</b>
3.1	Beam-Based Positron Annihilation Spectroscopy .....	52
3.1.1	The Positron Beam .....	52
3.1.2	Doppler Broadening Technique .....	54
3.1.3	Beam Measurements made on MeV Ion-Irradiated Silicon .....	56
3.2	Positron Annihilation Lifetime Spectroscopy .....	61
3.2.1	The Lifetime Technique .....	62
3.2.2	Sandwich Configuration with $^{22}\text{Na}$ Source .....	64
3.2.3	Implantation Profile of Positrons from a $^{22}\text{Na}$ Source .....	66
3.2.4	Experimental Verification of New Model .....	68
3.2.5	Lifetime Measurements made on MeV Ion-Irradiated Silicon ...	77
3.3	Fourier Transform Infrared Spectroscopy .....	85
3.3.1	Observation of Defects using FTIR .....	85
3.3.2	FTIR Measurements made on MeV Ion-Irradiated Silicon .....	87
<b>4</b>	<b>Defect-Engineered SOI Rib Waveguide Devices .....</b>	<b>91</b>
4.1	Design and Fabrication .....	91
4.1.1	Waveguide Processing .....	91
4.1.2	Incorporation of Defects into Waveguides .....	93
4.1.3	Process Considerations of Implantation Mask .....	94
4.1.4	Facet Preparation .....	97
4.2	Static Attenuators .....	99
4.2.1	Measurement of Optical Loss .....	99
4.2.2	Response of Attenuation to Thermal Annealing .....	103
4.2.3	Analysis of Modal Loss Mechanisms Due to Defects .....	105
4.3	Other Devices for Future Work .....	111
4.3.1	Integrated Optical Barriers .....	111
4.3.2	Barriers Between Waveguides .....	113
4.3.3	Directional Couplers .....	114
<b>5</b>	<b>Summary .....</b>	<b>116</b>
5.1	Characterization of Defects .....	116
5.2	Defect-Engineered SOI Rib Waveguide Devices .....	117
	<b>Bibliography .....</b>	<b>120</b>

# List of Figures

2.1 Optical absorption via band-to-band transitions (a) free carrier transitions (b) and traps (c) .....	15
2.2 Photon stream incident on a distribution of atoms illustrating Rayleigh scattering .....	17
2.3 Reflection and Refraction .....	19
2.4 Total internal reflection in a planar waveguide .....	22
2.5 Cross-section of a SOI rib waveguide structure .....	25
2.6 Effective indices created in rib structure and causing confinement in lateral direction .....	27
2.7 Field distributions of the two lowest order even propagation modes in a planar waveguide .....	30
2.8 Two closely spaced rib waveguides and the overlapping of mode tails .....	35
2.9 TRIM simulations of the projected range (a) and straggle (b) of MeV Si <sup>+</sup> irradiation of silicon .....	39
2.10 TRIM simulation of the vacancy-type defect distribution created by 2.8MeV self-irradiation of silicon .....	43
2.11 Structure of the divacancy in the silicon lattice .....	48
2.12 Deep levels associated with the silicon divacancy .....	49
2.13 The 1.8μm infrared absorption band associated with silicon divacancies created by implantation of oxygen .....	50
3.1 S parameter data obtained for silicon irradiated with 2.8MeV Si <sup>+</sup> .....	57
3.2 Effective divacancy concentration versus ion dose for 2.8MeV Si <sup>+</sup> irradiation of silicon .....	58
3.3 S parameter data obtained for silicon irradiated with 1.5MeV H <sup>+</sup> .....	59
3.4 Effective divacancy concentration versus ion dose for 1.5MeV H <sup>+</sup> irradiation of silicon .....	60
3.5 The sandwich configuration used in conventional PAS .....	65
3.6 Setup required for optimum etching uniformity .....	71
3.7 Etch rate of silicon using the setup shown in Fig. 3.5 with a 23% KOH solution at 80°C .....	72
3.8 Measured fraction of positrons annihilating in various thicknesses of silicon used in the bi-layer sandwich configuration .....	74
3.9 Implantation profile of positrons emitted from a <sup>22</sup> Na source, modeled using Eq. 3.20 and an exponential .....	76
3.10 Concentration of divacancies in 1.5MeV H <sup>+</sup> irradiated silicon, measured using PALS and a positron beam and calculated using the CBK formula .....	80

3.11 Vacancy distribution in silicon obtained from TRIM. The solid curve represents the implantation of 1.5MeV H <sup>+</sup> ions. The dashed curve represents the formation of divacancies after recombination .....	81
3.12 Annealing response of defect concentration (a) and positron lifetime (b) for silicon irradiated with 1.5MeV H <sup>+</sup> to a dose of 3×10 <sup>15</sup> cm <sup>-2</sup> .....	83
3.13 FTIR absorption spectrum for silicon irradiated with 3MeV protons to a dose of 2×10 <sup>16</sup> cm <sup>-2</sup> .....	87
3.14 FTIR absorption spectra for silicon irradiated with 9.8MeV Si <sup>+</sup> to a dose of 7.9×10 <sup>13</sup> cm <sup>-2</sup> (higher peak) and 3MeV H <sup>+</sup> to a dose of 2×10 <sup>16</sup> cm <sup>-2</sup> (lower peak) .....	88
3.15 Annealing response of 1.8μm absorption band for silicon sample irradiated with 9.8MeV Si <sup>+</sup> to a dose of 7.9×10 <sup>13</sup> cm <sup>-2</sup> .....	89
3.16 Total absorption determined by integrating under the 1.8μm divacancy peaks in Fig. 3.15 .....	90
4.1 BPM simulation of the fundamental TE mode propagation in the fabricated waveguides used in this study .....	92
4.2 Overlap of damaged region (hatched area) with fundamental TE mode .....	94
4.3 Configuration of stress-compensated ion implantation mask .....	97
4.4 SEM image of a typical waveguide end facet made by a careful dicing procedure .....	98
4.5 Setup used to make waveguide loss measurements .....	99
4.6 Infrared camera images of the output mode from a waveguide with no defects (a) and the output mode from a defected waveguide (b) .....	100
4.7 Measured loss in Si <sup>+</sup> implanted waveguides versus length of implant window .....	102
4.8 Annealing results for the sample self-irradiated to a dose of 6.3×10 <sup>13</sup> cm <sup>-2</sup> .....	103
4.9 Modal attenuation versus temperature, found by the slope of each linear fit in Fig. 4.8 .....	104
4.10 Optical absorption $\alpha_a$ , derived from Eq. 4.2, versus implantation dose for 2.8MeV Si <sup>+</sup> ions (open squares) and total attenuation $\alpha_d$ measured in the irradiated SOI rib waveguides (closed squares) .....	106
4.11 BeamProp simulation of mode evolution due to the increase in the real part of the index of the defected layer in the SOI rib waveguide .....	109
4.12 BeamProp simulation of radiation loss (open squares) and total loss (closed squares) versus length of defected region using an implantation dose of 6.3×10 <sup>13</sup> cm <sup>-2</sup> .....	110
4.13 Design of an optical barrier between adjacent waveguides .....	113
4.14 Design for enhanced coupling between adjacent waveguides .....	114

# Chapter 1

## Introduction

### 1.1 Siliconizing Photonics

The development of fabrication processes for Integrated Optical Components (IOCs) continues to receive much attention [1]. It is clear that future devices must not only perform with high-level functionality, but in addition must have the capability for production in a high-volume, high-yield environment. The advantages of silicon as a base material for the manufacture of IOCs have been well described by a number of authors [2-4]. Silicon is virtually transparent at the important telecommunication wavelengths around  $1.55\mu\text{m}$ , has a relatively high refractive index allowing for the fabrication of compact device geometries, and has excellent and well-understood electrical properties permitting the seamless integration of electrical and optical functionality on the same chip. Of greatest significance is the established manufacturing infrastructure that was developed around Very Large Scale Integration (VLSI) circuit technology in the 1960's. Thus, advanced silicon processing techniques have been built upon many decades of research and high-volume, low-cost production for the microelectronics industry.

More recently, Silicon-On-Insulator (SOI) has become the material system of choice for many microelectronic applications [5]. In bulk silicon, the active devices are fabricated using a monocrystalline homogeneous substrate, whereas in SOI, the top

silicon active layer is separated from the underlying mechanical substrate by a thin insulating layer of silicon dioxide. This dielectric isolation provides reduced parasitic capacitances and leakage currents, leading to a number of advantageous device and circuit properties such as eased processing, excellent device scalability, higher speeds, lower costs, lower power consumption, and better performance at high temperatures [5].

SOI is also considered a strong candidate to fabricate IOCs for advanced telecom applications. Because of the large refraction index difference between silicon and silicon dioxide, the SOI structure supports pure guided modes without optical coupling to external radiation fields [6], meaning that low-loss optical waveguides can be integrated onto a chip. Much investigation has been focused on SOI structures because of the possibility of making optical functionalities fully compatible with advanced VLSI chips [7]. As described in [5], the most common methods of preparing SOI substrates are by Separation by IMplantation of OXYgen (SIMOX), Bonding and Etch-back SOI (BESOI), and Smart-Cut.

Over the past two decades a number of SOI optical devices have been proposed and demonstrated including simple rib waveguides, (de)multiplexers, and thermo-optic switches [3]. More recently, integrated opto-electronic devices in SOI have been achieved such as solid-state electronic variable optical attenuators [8] and monolithic optical modulators operating above 1GHz [9]. Future development of monolithic photodetectors and efficient silicon-based optical sources, both compatible with telecom wavelengths, will likely use SOI material systems as well [4].

## 1.2 Defect-Engineering in Silicon Photonics

It was recognized by Corbett *et al.* [10] that primary crystalline defects can arise during common silicon device fabrication processes such as thin film deposition or growth, plasma etching, ion implantation and thermal annealing, whereas combinations of implantation and high temperature annealing can result in the formation of complex secondary defect structures. Although process-induced defects are unwanted for most device applications, it is worth considering the potentially advantageous properties of defects that have been deliberately introduced. In this case, of primary importance is the use of ion implantation to create defects in a controllable way.

The study of implantation-induced defects is an important topic of research as many silicon properties are extremely sensitive to lattice imperfections. Corbett *et al.* [10] identified the defect-related levels in the band-gap and the defect/carrier interaction mechanisms, which relate to electrical conductivity, as being the most important. It has also been known for some time that defects in silicon have a measurable influence on the refractive index, as shown by Baranova *et al.* [11], and on optical absorption, as shown by Fan and Ramdas [12]. Moreover, sufficient implantation damage can result in the structural transformation of silicon from a crystalline to an amorphous phase. Recently, process engineers have utilized defects to create novel micro and nano-structures by means of so-called “defect-engineering” [13]. This is well established in microelectronics, for applications such as transition metal gettering [14] and minority carrier lifetime adjustment [15].

Defect-engineering has been shown to be important in silicon photonic applications as well. In recent work, the implantation of  $B^+$  ions into n-type silicon followed by high temperature annealing to produce a thin band of dislocations  $\sim 100\text{nm}$  from a p-n junction, enhanced the emission of infrared radiation at room temperature under forward bias [16]. The origin of this radiation was attributed to confinement of the injected carriers between the band of dislocations and the p-n junction itself, thus limiting the opportunity for non-radiative recombination. In other work, it was shown that a small amount of implantation damage produced by irradiation of  $H^+$  ions could enhance the photoconductivity of SOI waveguide p-i-n detectors [17]. Of particular relevance to this thesis is a study by de Dood and Polman [18] describing the fabrication of silicon waveguides using amorphizing  $Xe^+$  ion implantation. The amorphous silicon was reported to have an increase in the real part of the refractive index of 0.3 at and around  $1.55\mu\text{m}$ . Following thermal processing at  $500^\circ\text{C}$ , the waveguides were reported to have a modal loss of approximately  $300\text{dBcm}^{-1}$ , which is suitable for optical confinement in devices on a scale of  $<100\mu\text{m}$ .

Baranova *et al.* [11] demonstrated that the real part of the refractive index of silicon increases as a function of ion implantation dose for low doses (below the amorphization threshold). Hence, implantation-induced damage is a potential technique that could be used to form selected regions of various indices, potentially leading to diverse silicon IOC applications. For instance, it may be possible to perturb the guiding properties of SOI waveguide structures (eg. change the mode shape, adjust the number of modes, or even induce radiation modes) by creating damaged regions in the silicon

overlayer. To date, the formation of devices with regions of various indices has been achieved by multiple layer deposition and etching stages. In many situations, elegant processes that utilize ion implantation may replace this fabrication approach. Using standard photolithography techniques to fabricate implantation masks, defect regions can be created with high precision areal selectivity. Since implantation-induced damage creates infrared absorption bands in silicon, as demonstrated by Fan and Ramdas [12], this technique can also be used to fabricate passive devices that require absorption of an infrared signal, including integrated static attenuators (within a waveguide) and optical barriers (between waveguides and other devices).

The alternative to damage mediated, on-chip optical absorption is absorption via the free carrier effect [19], which requires the implantation of dopants followed by high temperature annealing (to activate the dopants). The annealing step adds to the processing thermal budget and results in dopant diffusion, which is significant when the silicon substrate is subjected to high temperatures [20]. By utilizing defects created by ion implantation, it is possible to eliminate the need for the high temperature annealing step (beneficial to the processing thermal budget) and hence the diffusion of the absorbing region (beneficial to the packing density of IOCs).

### **1.3 Objectives of this Work**

The impact of free carriers on optical absorption in silicon waveguides has been well described previously [21]. However, only a few studies have quantitatively addressed the issue of optical absorption caused by crystalline defects in silicon

waveguides [22,23]. It was demonstrated by Cheng *et al.* [24] that silicon divacancies cause excess absorption at near infrared wavelengths (i.e. for photon energies greater than the silicon bandgap). More recent studies such as those by Kauppinen and Corbel [25] and Uedono *et al.* [26] have shown that divacancies are the dominant vacancy-type defect structure formed by ion implantation doses well below the amorphization threshold. Thus, it seems reasonable to investigate the absorption of 1.55 $\mu\text{m}$  optical signals in silicon waveguides irradiated with low ion doses. The work here is primarily concerned with vacancy-type defects in SOI rib waveguide devices.

Before making measurements on SOI structures, comprehensive characterization methods were utilized on ion-irradiated bulk silicon. In order to fully exploit defect-engineering, a complete understanding of the properties of implantation-induced defects in silicon is required. Also, the effects of different implantation conditions must be understood. A technique that has contributed significantly to the experimental analysis of vacancy-type defects is Positron Annihilation Spectroscopy (PAS) [27]. It has been used successfully to investigate the concentration and size of vacancy-type defects in semiconductor materials. In the work here, measurements of Doppler broadening of the annihilation gamma-ray energy were performed on bulk silicon samples irradiated with various doses of MeV  $\text{Si}^+$  and  $\text{H}^+$ . Positron lifetime measurements were performed on the samples irradiated with  $\text{H}^+$ . The intentions of these measurements were to determine the concentrations of vacancy-type defects (while confirming the dominance of divacancies) following low doses of ion-irradiation and to deduce how these concentrations scale with dose. Lifetime measurements are not typically performed on

defect layers created in ion-irradiated semiconductors due to the incomplete absorption of high energy positrons emitted from conventional  $^{22}\text{Na}$  sources [27]. In this work, an accurate model for the positron implantation profile in silicon was developed and experimentally confirmed. This allowed, for the first time, qualitative assessment of a thin defect layer using the bulk lifetime technique. For optical characterization, Fourier Transform InfraRed (FTIR) spectroscopy was used to confirm the excess optical absorption as a function of wavelength in the near infrared region.

A small volume of high optical absorption in the overlayer of an SOI rib waveguide can be used as an integrated static attenuator, which can apply to special cases such as the protection of devices that are sensitive to high optical intensity. This thesis explores the impact of implantation-induced damage on the attenuation of light at and around  $1.55\mu\text{m}$  in SOI rib waveguides. Implantation of  $\text{Si}^+$  ions was employed in order to enable the decoupling of attenuation effects resulting from lattice damage and that potentially introduced as a result of chemical doping. Further, self-irradiation of silicon is commonplace and the processes used here can be described as being compatible with standard device fabrication. Since an increase in optical absorption is generally accompanied by an increase in the real part of the refractive index [3], modal radiation effects were investigated. Using predictions of absorption coefficient and change in refractive index associated with implantation-induced defects in bulk silicon, the total loss caused by a volume of defects in an SOI rib waveguide was simulated using BeamProp, a commercial software package developed by Rsoft [28].

It is also of some interest to discuss the potential of an integrated optical barrier created by a volume of defects in the region separating two waveguides, or separating any two devices for that matter. As IOCs become more complex and the packing of components becomes denser, the problem of undesired optical noise or crosstalk between adjacent devices becomes a significant design issue [19]. The solution to this problem involves integrated optical absorption, which is becoming an important design issue in silicon photonic circuits. Damage mediated, on-chip optical absorption can potentially be used as an optical barrier between any devices integrated on the same substrate. Specific requirements to minimize optical noise between two integrated components depend on the device application. This work compared the absorption at a wavelength of  $1.55\mu\text{m}$  created by self-irradiation of silicon with that created by the free carrier effect. The possibility of using implantation damage to reduce crosstalk between closely spaced SOI rib waveguides was also discussed.

## Chapter 2

# Background and Theory

### 2.1 Light in Bulk Media

This section reviews the behavior of electromagnetic waves in bulk media. Some of the basics of wave propagation are introduced, which are fundamental to the understanding of guided wave theory. Optical properties including refractive index, absorption coefficient and scattering are described. Much of this theory is discussed in significant detail within many standard texts including [3], [4], [29] and [30].

#### 2.1.1 Wave Propagation

When considering the propagation of light in a medium, it is important to keep in mind that light is in fact an electromagnetic wave with electric and magnetic fields that are orthogonal to each other and to the direction of propagation. The behavior of electromagnetic waves in bulk matter can be described by Maxwell's equations:

$$\nabla \times \mathbf{E} = -\frac{\partial \mathbf{B}}{\partial t} \quad (2.1)$$

$$\nabla \times \mathbf{H} = \mathbf{J} + \frac{\partial \mathbf{D}}{\partial t} \quad (2.2)$$

$$\nabla \cdot \mathbf{D} = \rho \quad (2.3)$$

$$\nabla \cdot \mathbf{B} = 0 \quad (2.4)$$

where  $\mathbf{E}$  (V/m) is the electric field vector,  $\mathbf{D}$  (C/m<sup>2</sup>) is the electric displacement vector,  $\mathbf{H}$  (A/m) is the magnetic field vector,  $\mathbf{B}$  (Wb/m<sup>2</sup>) is the magnetic displacement vector,  $\mathbf{J}$  (A/m<sup>2</sup>) is the electric current density, and  $\rho$  (C/m<sup>3</sup>) is the electric charge density. Assuming a lossless medium, these equations are combined with the relations:

$$\mathbf{D} = \epsilon\mathbf{E} \quad (2.5)$$

$$\mathbf{B} = \mu\mathbf{H} \quad (2.6)$$

where  $\epsilon$  and  $\mu$  are the electric permittivity and magnetic permeability of the medium, respectively. In the case of dielectric materials,  $\rho=0$  and  $\mathbf{J}=0$ . Now taking the curl of both sides of Eq. 2.1, and using the relations in Eqs. 2.2, 2.5 and 2.6, and using the vector identity:

$$\nabla \times \nabla \times \mathbf{E} = \nabla(\nabla \cdot \mathbf{E}) - \nabla^2 \mathbf{E} \quad (2.7)$$

the familiar wave equation for the electric field in the medium is obtained:

$$\nabla^2 \mathbf{E} = \mu\epsilon \frac{\partial^2 \mathbf{E}}{\partial t^2} \quad (2.8)$$

Assuming a harmonic wave solution, this expression is also written in the more familiar notation of the Helmholtz equation:

$$\nabla^2 \mathbf{E} + w^2 \mu\epsilon \mathbf{E} = 0 \quad (2.9)$$

where  $w=2\pi\nu$  and  $\nu$  is the frequency of the wave. Using the same approach, a similar expression is found for the magnetic field:

$$\nabla^2 \mathbf{H} + w^2 \mu\epsilon \mathbf{H} = 0 \quad (2.10)$$

The solutions for the electric and magnetic fields of a wave propagating in the  $z$  direction take the general form:

$$E = E_0 \exp[j(kz \pm \omega t)] \quad (2.11)$$

$$H = H_0 \exp[j(kz \pm \omega t)] \quad (2.12)$$

where  $k$  is the wavevector of the electromagnetic wave in the medium. Hence, the phase of the wave:

$$\phi = kz \pm \omega t \quad (2.13)$$

varies with both time and distance. The angular frequency  $\omega$  therefore describes how the phase varies with time. The wavevector, which defines the rate at which the phase changes in the propagation direction of the wave, is also known as the propagation constant in the direction of the wavefront, and follows the relations:

$$k = \omega \sqrt{\mu\epsilon} = \frac{\omega}{c} = \frac{2\pi}{\lambda} \quad (2.14)$$

where  $c$  and  $\lambda$  are the speed and wavelength of the light in the medium, respectively. Thus, with longer wavelengths, there is less spatial variation of the phase as the wavefront propagates.

### 2.1.2 Refractive Index

The most fundamental approach to describing the refractive index of a medium is by considering its dielectric properties. A dielectric medium will respond to an electric field  $\mathbf{E}$  and create a polarization density  $\mathbf{P}$  (C/m<sup>2</sup>). This does not happen instantaneously and hence all materials are dispersive, i.e. have frequency dependent responses, although in some idealized situations the material is assumed to be nondispersive. The medium is linear if  $\mathbf{P}$  is linearly related to  $\mathbf{E}$ , homogenous if the relation is independent of the

position in the material, and isotropic if the relation is independent of the direction of the applied field. In this discussion, the material is assumed to be dispersive, linear, homogeneous, and isotropic. Since the medium is dispersive, the response to the applied field is frequency dependent. The resulting polarization density is given by:

$$\mathbf{P} = \epsilon_0 \chi(\nu) \mathbf{E} \quad (2.15)$$

where  $\epsilon_0$  is the electric permittivity of free space,  $\chi(\nu)$  is the frequency dependent electric susceptibility of the material. Physically, the electric field of an electromagnetic wave induces oscillations of the weakly bound electrons with respect to the positive nuclei in the atoms of the medium. This constitutes oscillating dipoles, which collectively create the polarization density. The system will begin to emit a secondary electromagnetic wave at the same frequency. With many atoms (and hence oscillating dipoles) in a given volume, the material is said to have an appreciable optical density. The refractive index  $n(\nu)$  is related to the electric susceptibility and is therefore frequency dependent as well. It is defined as:

$$n(\nu) = (1 + \chi(\nu))^{1/2} \quad (2.16)$$

and can be thought of as a parameter that quantifies the optical density of the material. The refractive index can also be represented by:

$$n(\nu) = \left( \frac{\epsilon(\nu)}{\epsilon_0} \right)^{1/2} \quad (2.17)$$

where  $\epsilon(\nu)$  is the frequency dependent permittivity of the medium and the ratio inside the brackets is known as the dielectric constant. As the frequency of the primary wave increases, the oscillating dipole will fall behind, lagging in phase by a proportionately

larger amount. The secondary wave will lag the primary wave and their sum will also lag the primary wave. Each such event introduces a phase lag into the light field, which ultimately shows up as a decrease in the phase velocity, or speed, of the electromagnetic wave. The speed of light in a material follows the relation:

$$c = \frac{c_0}{n(\nu)} \quad (2.18)$$

where  $c_0$  is the speed of light in free space in which the susceptibility is zero. The refractive index of a medium is therefore always greater than unity. The propagation constant in the material is related to that in free space by:

$$k = n(\nu)k_0 \quad (2.19)$$

where  $k_0$  is defined by the free space wavelength  $\lambda_0$ . In effect, the refractive index of a material is the factor by which the optical path length increases relative to that in free space and determines the rate of phase change with propagation distance.

### 2.1.3 Absorption

Dielectric materials that absorb light are often represented phenomenologically by a complex susceptibility:

$$\chi(\nu) = \chi'(\nu) + j\chi''(\nu) \quad (2.20)$$

and hence Eq. 2.16 takes the form:

$$n_R(\nu) + jn_I(\nu) = (1 + \chi'(\nu) + j\chi''(\nu))^{1/2} \quad (2.21)$$

where  $n_R(\nu)$  and  $n_I(\nu)$  are now the real and imaginary parts of the refractive index. Using a complex refractive index in Eq. 2.19, the electric field of the electromagnetic wave described in Eq. 2.11 can then be written as:

$$E = E_0 \exp[j((n_R(\nu) + jn_I(\nu))k_0z \pm \omega t)] \quad (2.22)$$

which can be rearranged to:

$$E = E_0 \exp[-n_I(\nu)k_0z] \exp[j(kz \pm \omega t)] \quad (2.23)$$

noting that  $n_R(\nu)$  is equivalent to  $n(\nu)$ . The power, or intensity, of the wave is proportional to the square of the amplitude:

$$I = I_0 \exp[-2n_I(\nu)k_0z] \quad (2.24)$$

indicating that the intensity of the light attenuates exponentially in the direction of propagation at a rate given by:

$$\alpha(\nu) = 2n_I(\nu)k_0 \quad (2.25)$$

where  $\alpha(\nu)$  is the frequency dependent absorption coefficient.

The mechanisms of absorption are best explained by considering the interactions of photons with electrons and holes in a semiconductor. There are a number of ways that photons can transfer their energy to the semiconductor material including band-to-band (interband) absorption, free carrier (intraband) absorption, absorption via traps, and absorption through direct phonon transitions. The latter is not significant to this discussion although long-wavelength photons, or photons with very low energy, will release their energy by directly exciting lattice vibrations, i.e. by creating phonons. The other three types of absorption are illustrated in Fig. 2.1.

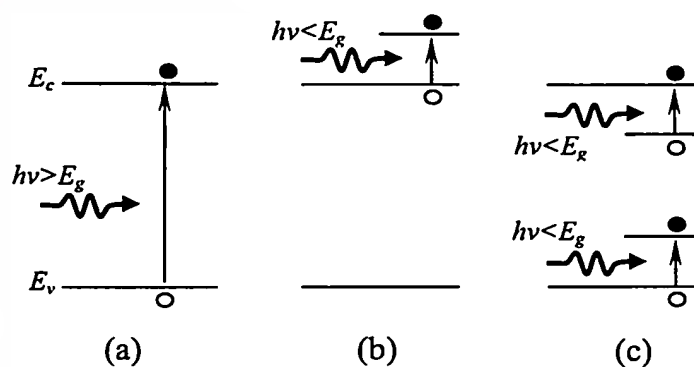


Figure 2.1: Optical absorption via band-to-band transitions (a) free carrier transitions (b) and traps (c).

In band-to-band transitions, photons having energy  $h\nu > E_g$ , where  $E_g = E_c - E_v$  is the bandgap of the material, can transfer their energy to electrons, which are excited from the valence band to the conduction band leaving behind holes. This is followed by thermalization, a process whereby the electron relaxes down to the bottom of the conduction band while releasing its energy in the form of lattice vibrations, or phonons. The electron-hole pairs will then recombine and energy is released either nonradiatively (in the form of phonons) or radiatively (in the form of emitted photons). In an indirect semiconductor, like silicon, photon emission is unlikely since it requires a change in momentum of the electron before recombination. Hence the radiative recombination lifetime  $\tau_r$  in silicon is much greater than its nonradiative recombination lifetime  $\tau_{nr}$ . Assuming that the Fermi level lies within the bandgap but away from the band edges by an energy of at least several times  $k_B T$ , the band-to-band component of the absorption coefficient is given by:

$$\alpha(\nu) = \frac{\sqrt{2}c^2 \left( \frac{m_h m_e}{m_h + m_e} \right)^{3/2}}{\tau_r (\hbar\nu)^2} (\hbar\nu - E_g)^{1/2} \quad (2.26)$$

where  $m_h$  and  $m_e$  are the effective masses of the holes and electrons in the valence and conduction band, respectively.

Free carrier absorption is a process whereby a photon with  $\hbar\nu < E_g$  imparts its energy to an electron or hole in the conduction or valence band, respectively, causing the carrier to move to a higher energy level within the band. This includes transitions from electrons or holes out of shallow donor or acceptor states, respectively. This is, again, followed by thermalization. The free carrier component of the absorption coefficient in semiconductors is given by the Drude-Lorenz equation:

$$\alpha(\nu) = \frac{e^3}{4\pi^2 \epsilon_0 c_0 \nu^2 n(\nu)} \left( \frac{N_e}{\mu_e m_e^2} + \frac{N_h}{\mu_h m_h^2} \right) \quad (2.27)$$

where  $e$  is the electronic charge,  $N_e$  and  $N_h$  are the free electron and free hole concentrations, respectively, and  $\mu_e$  and  $\mu_h$  are the electron and hole mobilities. The concentration of free carriers will affect both the real and imaginary parts of the refractive index, which demonstrates the interdependence of some parameters in this equation, so care must be taken when evaluating the effect of free carrier absorption.

Absorption can also occur via carrier traps in the semiconductor material. Traps are associated with impurities or lattice defects having energy levels that lie within the energy bandgap but away from the band edges by several  $k_B T$ . These are usually referred to as deep levels. For example, a photon with energy  $\hbar\nu < E_g$  can excite a carrier into a deep level defect, where it is trapped and eventually releases its energy by either

nonradiative or radiative recombination. These deep levels can trap either holes or electrons.

### 2.1.4 Scattering

Since attenuation refers to the intensity reduction in the direction of wave propagation, it can also be caused by scattering, which redirects some of the light away from the primary path. As mentioned previously, an electromagnetic wave will induce oscillating dipoles in the atoms of a medium and these will in turn re-emit light. In other words, a photon is absorbed and without delay another photon of the same frequency is emitted. The light is therefore elastically scattered. Generally, the photons scatter out in random directions from the atom, as shown in Fig. 2.2, forming spherical wavelets.

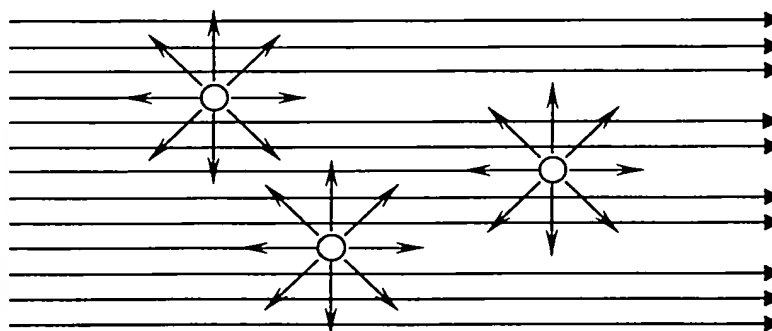


Figure 2.2: Photon stream incident on a distribution of atoms illustrating Rayleigh scattering.

Scattering from particles smaller than the wavelength of light is referred to as Rayleigh scattering and it has been shown that the intensity of the scattered light is proportional to  $\lambda^{-4}$ . It can be shown that in any medium (gas, liquid, or solid) the

interference of the scattered wavelets will be almost completely constructive in the forward direction, which explains why the primary electromagnetic wave advances. The denser the material through which the light advances, the less the lateral scattering. With a tremendous number of close-together atoms, the interference of the scattered wavelets will be almost completely destructive in the lateral direction. This does not imply attenuation since interference produces a redistribution of energy, out of regions where it is destructive into regions where it is constructive. In a perfectly homogeneous solid, i.e. uniform and ordered, destructive interference will predominate in all directions other than forward and hence most of the energy will go into the forward direction, advancing the beam essentially undiminished. The significance of Rayleigh scattering, in terms of attenuation of light in a semiconductor, depends on the degree of uniformity and order in the material. Imperfections such as voids, impurity atoms, or crystalline defects can result in increased destructive interference of the scattered wavelets in the forward direction. Hence energy is redistributed from the propagation direction into other directions resulting in the attenuation of the primary wave. The contribution of scattering to attenuation is related to the number of defects and their size with respect to the wavelength of propagation.

## 2.2 Guided Wave Theory

This section discusses structures that can be used to confine electromagnetic waves and hence guide them in the desired direction. The methods used to solve for the optical modes are described. This work is primarily focused on rib waveguide structures

however simple planar (slab) waveguides are first introduced. Also described are the attenuation mechanisms in waveguides and the coupling from one guide to another. Much of this theory is discussed in significant detail within many standard texts including [3], [4], [29] and [30].

### 2.2.1 Reflection and Refraction

The processes of reflection and refraction are macroscopic manifestations of scattering that occurs on a submicroscopic level. In order to understand these processes, and hence the basics of guided wave propagation, it is worthy to employ the ray optics approach. One must begin by considering what happens when a ray of light impinges on an interface between two media with different refractive indices. This situation is illustrated in Fig. 2.3. The angle of reflection is equal to the angle of incidence while the angle of refraction follows Snell's law:

$$n_1 \sin \theta_1 = n_2 \sin \theta_2 \quad (2.28)$$

where  $n_1$  is the index of the first medium,  $n_2$  is the index of the second medium,  $\theta_1$  is the

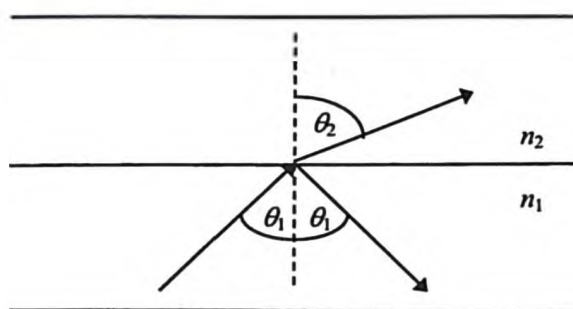


Figure 2.3: Reflection and refraction.

angle of incidence, and  $\theta_2$  is the angle of refraction. The light is said to be partially reflected and partially transmitted. At the critical incident angle  $\theta_c$ , the refraction angle will reach  $90^\circ$  and no light will be transmitted. Hence this angle is given by the equation:

$$\theta_c = \sin^{-1}\left(\frac{n_2}{n_1}\right) \quad (2.29)$$

and for incident angles greater than this value the light is totally internally reflected.

As mentioned above, light is in fact an electromagnetic wave with electric and magnetic fields that are orthogonal to each other and to the direction of propagation. The polarization of such a wave is the direction of the electric field vectors. Thus, two special conditions arise when considering the behavior of electromagnetic waves at an interface. The first condition is the transverse electric (TE) condition in which the electric field vectors are orthogonal to the plane of incidence (i.e. orthogonal to the page in Fig. 2.3). The second is the transverse magnetic (TM) condition in which the magnetic field vectors are orthogonal to the plane of incidence. The partial reflection and transmission are then given for each polarization condition by the Fresnel formulae:

$$r_{TE} = \frac{n_1 \cos \theta_1 - n_2 \cos \theta_2}{n_1 \cos \theta_1 + n_2 \cos \theta_2} \quad (2.30)$$

$$t_{TE} = 1 + r_{TE} \quad (2.31)$$

$$r_{TM} = \frac{n_2 \cos \theta_1 - n_1 \cos \theta_2}{n_2 \cos \theta_1 + n_1 \cos \theta_2} \quad (2.32)$$

$$t_{TM} = \frac{n_1}{n_2}(1 + r_{TM}) \quad (2.33)$$

where  $r_{TE}$  and  $t_{TE}$  are the reflection and transmission coefficients for TE polarization while  $r_{TM}$  and  $t_{TM}$  are those for TM polarization. These are the factors by which the incident field amplitude is altered. However, we are typically more interested in the amount of power (or intensity) that is reflected or transmitted, therefore we use the reflectance  $R=r^2$ . Conservation of power requires that the transmittance  $T=1-R$ . These values represent the portions of the incident field intensity that are reflected and transmitted. It can be shown that the reflection and transmission coefficients are generally complex quantities, thus are accompanied by phase shifts. Since we are interested in the total reflection phenomenon, for the purpose of guiding light, the condition  $n_1 > n_2$  must be met in order to satisfy Eq. 2.29. Under this condition, total reflection is possible and is accompanied by phase shifts given by:

$$\tan \frac{\phi_{TE}}{2} = \frac{\sqrt{(\sin^2 \theta_1 - \sin^2 \theta_c)}}{\cos \theta_1} \quad (2.34)$$

$$\tan \frac{\phi_{TM}}{2} = \frac{\sqrt{(\sin^2 \theta_1 - \sin^2 \theta_c)}}{\cos \theta_1 \sin^2 \theta_c} \quad (2.35)$$

where  $\phi_{TE}$  and  $\phi_{TM}$  are the phase shifts for the TE and TM polarizations, respectively.

### 2.2.2 Planar Waveguides

The simplest form of waveguide is a slab of material with index  $n_1$  sandwiched between two (cladding) materials with smaller indices  $n_2$  and  $n_3$ . With the appropriate propagation angle, relative to the interface normal, the light can be confined in the high index core material by total internal reflection. The light wave zigzags back and forth

between the upper and lower claddings as illustrated in Fig. 2.4. In this diagram, the waveguide (i.e. the core) height is  $h$ , and the propagation is in the  $z$  direction with confinement in the  $y$  direction. The wavevector  $k$  can be decomposed into two components, in the  $y$  and  $z$  directions. These are:

$$k_y = n_1 k_0 \cos \theta_1 \quad (2.36)$$

$$k_z = n_1 k_0 \sin \theta_1 \quad (2.37)$$

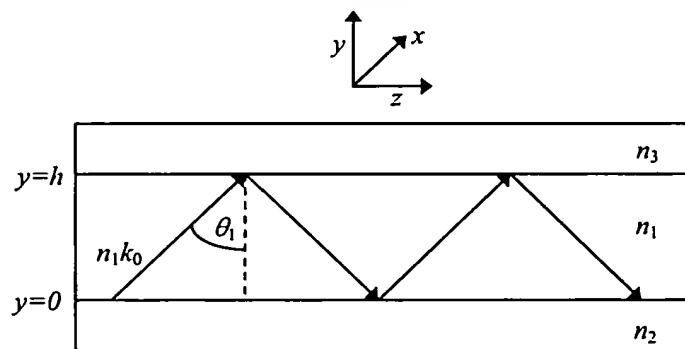


Figure 2.4: Total internal reflection in a planar waveguide.

Considering the  $y$  component of the wavevector, this wave will be reflected at each interface with the potential of forming a standing wave across the waveguide in the  $y$  direction. Summing up the phase shifts introduced by making a complete round trip across the waveguide in the  $y$  direction gives:

$$\phi_t = 2k_y h - \phi_u - \phi_l \quad (2.38)$$

where  $\phi_u$  and  $\phi_l$  are the phase changes introduced upon reflection at the upper and lower waveguide interfaces, respectively. From Eqs. 2.34 and 2.35, we know that these phase

changes will depend on the indices of the cladding material. In the case of an SOI planar waveguide, the lower cladding layer is silicon dioxide ( $n_2=1.5$ ) and the upper is typically air ( $n_3=1.0$ ). Since these indices are both very different from that of the core silicon ( $n_1=3.5$ ), this type of planar waveguide can be approximated as symmetrical, written  $n_2 \approx n_3$ . This means we can assume that  $\phi_u = \phi_l$  and these can both be referred to as the phase change due to reflection  $\phi_r$ . For preservation of the standing wave, the total phase shift must be a multiple of  $2\pi$ , thus it is possible to re-write Eq. 2.38 as:

$$2m\pi = 2k_0 n_1 h \cos \theta_1 - 2\phi_r \quad (2.39)$$

By substituting in the phase change due to reflection for the TE and TM polarizations given in Eqs. 2.34 and 2.35, respectively, Eq. 2.39 can be rearranged for both polarizations to give:

$$\tan \left[ \frac{k_0 n_1 h \cos \theta_1 - m\pi}{2} \right] = \left[ \frac{\sqrt{\sin^2 \theta_1 - \sin^2 \theta_c}}{\cos \theta_1} \right] \quad (2.40)$$

$$\tan \left[ \frac{k_0 n_1 h \cos \theta_1 - m\pi}{2} \right] = \left[ \frac{\sqrt{\sin^2 \theta_1 - \sin^2 \theta_c}}{\cos \theta_1 \sin^2 \theta_c} \right] \quad (2.41)$$

which are known as the eigenvalue equations for the TE and TM polarizations, respectively. Since  $m$  is an integer, there will be a series of discrete incident angles (or propagation angles) for which these eigenvalue equations can be solved. For each solution, there will be a corresponding propagation constant in both the  $y$  and  $z$  directions given by Eqs. 2.36 and 2.37, respectively. Thus, light cannot propagate at any angle, but only at allowed discrete angles. At other angles, the phase shifts will result in destructive interference of the standing wave. The solutions are referred to as the modes of

propagation, with mode numbers given by the integer values of  $m$ . For example, the lowest order (fundamental) TE and TM modes are called TE<sub>0</sub> and TM<sub>0</sub>, respectively. It is useful to know the number of modes supported by a waveguide structure. We do know that the minimum possible propagation angle  $\theta_1$  corresponds to the critical angle  $\theta_c$  and this corresponds to the highest possible order mode  $m_{max}$ . In this case, the right sides of both Eq. 2.40 and Eq. 2.41 reduce to zero and solving for  $m_{max}$  gives:

$$m_{max} = \frac{k_0 n_1 h \cos \theta_c}{\pi} \quad (2.42)$$

The highest order mode number  $(m_{max})_{int}$  is the nearest integer that is less than  $m_{max}$ . The number of modes will be  $(m_{max})_{int} + 1$  since the lowest order mode has a mode number  $m=0$ . Since there is always a solution for  $m=0$  in the case of symmetrical waveguides, the fundamental mode will always propagate and the waveguide is never cut-off. This is not generally true for asymmetrical waveguides, except for special cases such as SOI planar structures in which symmetrical behavior is apparent. It is often convenient for a waveguide to support only a single mode. For a symmetrical planar waveguide, it can be shown that the single-mode condition is given by:

$$h < \left( \frac{\lambda_0 / 2}{n_1 \sqrt{1 - (n_2 / n_1)^2}} \right) \quad (2.43)$$

which is valid for both TE and TM polarizations. Therefore, single-mode planar structures generally require small dimensions. For instance, for a wavelength of 1.55  $\mu\text{m}$  in SOI, the height  $h$  must be less than about 0.23  $\mu\text{m}$ .

### 2.2.3 Rib Waveguides and the Effective Index Method

The planar waveguides mentioned in section 2.2.2 provide confinement in the  $y$  direction but not in the  $x$  direction and are not practical structures since any light wave will just spread throughout the horizontal plane. For many applications two-dimensional confinement is required. In SOI, this is most commonly achieved by etching regions of the silicon, forming the so-called rib waveguide. The cross-section of a rib waveguide is shown in Fig. 2.5. In this diagram, the propagation direction is now orthogonal to the page. It may not be obvious why this structure achieves optical confinement in the lateral direction. To explain this, we must first introduce the effective index of a mode.

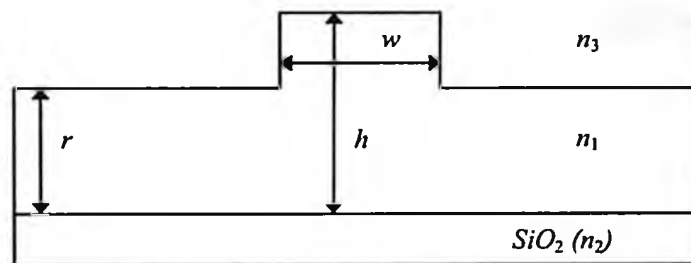


Figure 2.5: Cross-section of a SOI rib waveguide structure.

The mode propagation constant, given by Eq. 2.37, indicates the rate at which the wave propagates in the  $z$  direction. This is often referred to as  $\beta$  instead of  $k_z$ . We now define a parameter  $N$ , called the effective index of the mode, such that:

$$N = n_1 \sin \theta_1 \quad (2.44)$$

and hence Eq. 2.37 becomes:

$$\beta = Nk_0 \quad (2.45)$$

This is equivalent to thinking of the mode as propagating straight down the waveguide with refractive index  $N$ , and without zigzagging back and forth between the upper and lower cladding. The effective index can be used to find approximate solutions for the propagation constants of two-dimensional (rectangular) waveguides. The general approach is to regard the two-dimensional structure as a combination of two planar waveguides, one horizontal and one vertical. We then successively solve the planar waveguide eigenvalue equations first in one direction and then the other, taking the effective index of the first as the core refractive index of the second. This is known as the effective index method, which is a good approximation in many situations but tends to become less accurate for more complex structures and/or larger index steps.

Nevertheless, the effective index method can be used to approximate the solutions for SOI rib structures such as that in Fig. 2.5. In this case, the index on either side of the core, of width  $w$ , is not constant over the height of the core  $h$ . Hence, we need to find the effective indices of two horizontal planar waveguides, one with height  $h$  and another with height  $r$ . We will call these effective indices  $N_h$  and  $N_r$ , respectively. To solve these parameters (for different wavelengths  $\lambda_0$  and allowed modes  $m$ ) we use the TE eigenvalue equation given by Eq. 2.40 and then the effective index equation given by Eq. 2.44. For both waveguides,  $n_1$  is used as the (silicon) core index and  $n_2=n_3$  as the ( $\text{SiO}_2$  or air) cladding indices. Typically, SOI rib waveguides are large (dimensions on the order of several  $\mu\text{m}$ ), resulting in only a slight decrease in the effective indices  $N_h$  and  $N_r$  for the fundamental mode compared to the index of silicon. Also,  $N_h$  is slightly greater than  $N_r$ , meaning there is some confinement in the lateral direction. The effective indices

effectively create a vertical planar waveguide as illustrated in Fig. 2.6. This is solved as before but now using  $N_h$  and  $N_r$  as the indices of the core and cladding, respectively, and  $w$  as the core height. Also, the TM eigenvalue equation given by Eq. 2.41 must be used in order to account for the change in orientation. This yields an effective index for the rib geometry, which can be used in Eq. 2.45 to calculate the propagation constant of the mode for this two-dimensional structure.

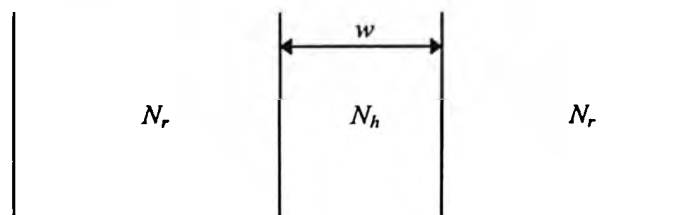


Figure 2.6: Effective indices created in rib structure and causing confinement in lateral direction.

It was mentioned above that planar waveguides generally require small dimensions in order to be single-mode. This is surprisingly not the case for rib waveguides. In the case of SOI, it is common that single-mode operation is possible with silicon layer thicknesses on the order of several  $\mu\text{m}$ . The reason for this is that with properly designed geometries of the rib waveguide, higher-order modes leak out of the waveguide over a very short distance, leaving only the fundamental mode propagating. Theoretical studies by Soref *et al.* [31] led to the rib waveguide single-mode condition:

$$\frac{a}{b} \leq \frac{r}{\sqrt{1-r^2}} \quad (2.46)$$

where  $a$ ,  $b$ , and  $r$  are normalizing parameters for the rib geometry in Fig. 2.5 with  $w$  replaced by  $2a\lambda$ ,  $h$  replaced by  $2b\lambda$ , and  $r$  replaced by  $2br\lambda$ . This equation is valid for  $0.5 \leq r < 1.0$  and is intended for large waveguides ( $b > 0.16$  for SOI).

### 2.2.4 Mode Profiles and the Beam Propagation Method

Thus far, the ray optics approach has made it straightforward to solve for the number of guided modes and the associated propagation constants in a given waveguide structure. However, it is not possible to solve for the electric field distributions, or the mode profiles, in a waveguide cross-section using this method. One must solve the Helmholtz equation, given by Eq. 2.9, with the appropriate boundary conditions in order to describe the mode fields and to visualize them.

In the case of the planar waveguide shown in Fig. 2.4, the boundary conditions for a TE polarized wave require continuity of the electric field and its derivative at the interfaces between the core and claddings ( $y=0$  and  $y=h$ ). With TE polarization, the electric field only exists in the  $x$  direction and its amplitude varies in the  $y$  direction. The wave propagates in the  $z$  direction with propagation constant  $\beta$ . Thus, the Helmholtz equation reduces to:

$$\frac{\partial^2 E_x}{\partial y^2} + \frac{\partial^2 E_x}{\partial z^2} + \omega^2 \mu \epsilon E_x = 0 \quad (2.47)$$

and the general solution takes the form:

$$E_x = E_x(y) \exp[j(\beta z \pm \omega t)] \quad (2.48)$$

Substituting Eq. 2.48 back into Eq. 2.47 and using the relations given in Eqs. 2.14 and 2.19, results in:

$$\frac{\partial^2 E_x}{\partial y^2} - (\beta^2 - k_0^2 n^2) E_x = 0 \quad (2.49)$$

Regarding Eqs. 2.36 and 2.37, one can derive the relation:

$$k_y^2 = k_0^2 n^2 - \beta^2 \quad (2.50)$$

and therefore Eq. 2.49 can be rewritten as:

$$\frac{\partial^2 E_x}{\partial y^2} + k_y^2 E_x = 0 \quad (2.51)$$

where  $k_y$  is a real number in the core but imaginary in the upper and lower claddings (corresponding to the condition that total internal reflection is satisfied at both interfaces).

The solution to Eq. 2.51 gives the variation of the field in the  $y$  direction  $E_x(y)$ , which takes the general form:

$$E_x(y) = \begin{cases} E_u \exp[-k_{y,u}(y-h)] & y \geq h \\ E_c \exp[-jk_{y,c}y] & 0 \leq y \leq h \\ E_l \exp[k_{y,l}y] & y \leq 0 \end{cases} \quad (2.52)$$

where the subscripts  $c$ ,  $u$  and  $l$  are used to represent the parameters in the core, upper and lower claddings, respectively. Thus, the field distribution is sinusoidal in the core, and exponentially decaying in the claddings. The terms  $k_{y,u}$  and  $k_{y,l}$  are referred to as decay constants (not propagation constants) and they determine the degree to which the field penetrates the claddings. In the core, modal solutions that are cosine functions are

referred to as even propagation modes and, similarly, sine functions are referred to as odd propagation modes.

As mentioned above, the boundary conditions are that the electric field and its derivative are continuous at both core-cladding interfaces ( $y=0$  and  $y=h$ ). Applying these boundary conditions to the components of Eq. 2.52 leads to the equation:

$$\tan^{-1} \left[ \frac{k_{yl}}{k_{yc}} \right] + \tan^{-1} \left[ \frac{k_{yu}}{k_{yc}} \right] = k_{yc} h + m\pi \quad (2.53)$$

and since  $k_{yc}$ ,  $k_{yu}$  and  $k_{yl}$  can be written in terms of  $\beta$  using Eq. 2.50, we obtain the eigenvalue equation for determining the guided modes  $m$ . Solving the propagation constants for each allowed mode allows us to determine the values of  $k_{yc}$ ,  $k_{yu}$  and  $k_{yl}$  for each mode. Using these values and the same boundary conditions, the field distribution  $E_x(y)$  given in Eq. 2.52 can be determined for each mode  $m$ . Fig. 2.7 shows the two lowest order even propagation modes. Since some of the field penetrates into the

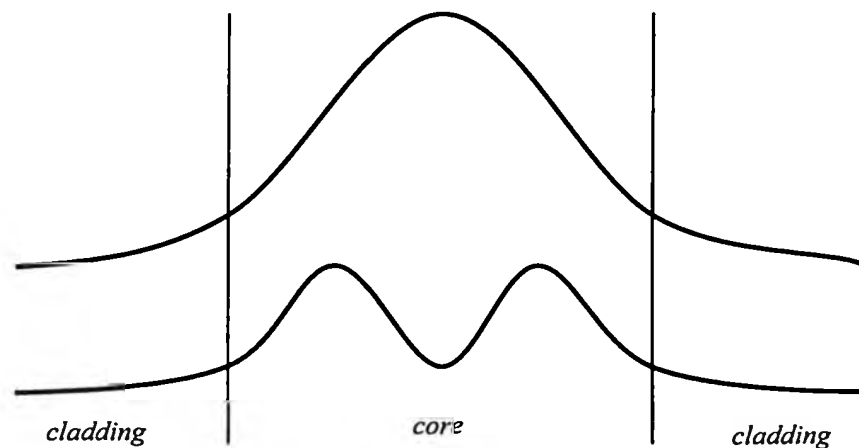


Figure 2.7: Field distributions of the two lowest order even propagation modes in a planar waveguide.

claddings, not all of the power propagating in a guided mode is contained inside the core. The part of the field outside of the core is called the evanescent field, or tail. The proportion of power in a given mode that lies within the core is known as the confinement factor, which is one way to quantify the modal confinement of a waveguide structure. This confinement is an intricate function of the index difference between the core and claddings, the polarization, the waveguide thickness, the wavelength of the light, and the mode number  $m$ .

Analytically solving mode profiles becomes considerably more complicated for complex waveguide structures such as the rib geometry. In cases such as this, numerical techniques are commonly employed, the most popular being the Beam Propagation Method (BPM) [32]. The BPM takes the Helmholtz equation given by Eq. 2.9 and factors out the rapid phase variation in the propagation direction by introducing a so-called slowly varying field  $u$ . This leads to the basic BPM equation:

$$\frac{\partial u}{\partial z} = \frac{j}{2k_r} \left( \frac{\partial^2 u}{\partial x^2} + \frac{\partial^2 u}{\partial y^2} + (k^2 - k_r^2)u \right) \quad (2.54)$$

where  $k_r$  is the reference wavenumber, which represents the average phase variation of the field. Given an input field, the BPM equation determines the evolution of this field in the propagation direction  $z$ . The BPM equation is a first order initial value problem that can be solved by simple “integration” along the  $z$  direction. This integration can be performed by a number of standard numerical techniques, the most popular being the finite-difference approach. In this approach, the field in the transverse ( $xy$ ) plane is represented only at discrete points on a grid, and at discrete planes along the  $z$ -axis.

Given the discretized field at one  $z$  plane, the goal is to derive numerical equations that determine the field at the next  $z$  plane. This elementary propagation step is then repeated to determine the field throughout the structure. It is possible to perform this computation quickly and accurately using commercial software packages such as BeamProp [28]. There are many advantages to the BPM technique, which make it very attractive for modeling photonic devices. The factoring of the rapid phase variation allows the slowly varying field to be represented numerically on a  $z$ -axis grid that can be much coarser than the wavelength for many problems. This means that faithful computations can be made in very little time. Also, structures with varying refractive index profiles in the propagation direction can be analyzed.

## 2.3 Attenuation in Semiconductor Waveguides

It was described previously how light is attenuated in bulk media. It is also worth considering the various mechanisms for attenuation in semiconductor waveguide structures, which are designed to confine light. This section discusses waveguide losses originating from three sources: absorption, scattering, and radiation. These forms of loss can all be linked to the processing (imperfections) of the waveguide and its material system during design and fabrication.

### 2.3.1 Absorption

As in bulk material, the absorption loss of confined light is due to band-to-band (interband) transitions, free carrier (intraband) transitions, and transitions via traps.

These mechanisms are discussed in section 2.1.3. The purpose of a waveguide is to confine light without absorbing it, therefore interband transitions are avoided by choosing a wavelength that is greater than the band edge wavelength of the material. For instance, telecom wavelengths around  $1.55\mu\text{m}$  are far enough from the band edge in silicon ( $1.1\mu\text{m}$ ) that SOI structures are virtually transparent in this range. The other types of absorption loss are more difficult to avoid but can be tolerated in most cases. Free carrier absorption is related to the concentration of dopants in the semiconductor waveguide and is typically negligible when using lightly doped silicon. Absorption via deep level traps is related to the concentration of lattice defects in the waveguide. With advanced wafer growth techniques and VLSI device processing, silicon waveguides can be fabricated with a very small amount of defects, so this form of absorption is also normally insignificant.

### 2.3.2 Scattering

Volume scattering is caused by perturbations such as voids, impurity atoms, or crystalline defects. The significance of this form of scattering is related to the number of defects and their size with respect to the wavelength of propagation. Volume scattering is negligible for defects much smaller than the wavelength. As mentioned in section 2.1.4, Rayleigh scattering is the dominant loss mechanism in bulk material, and it exhibits a  $\lambda^{-4}$  dependence. However, for confined waves, the wavelength dependence is related to the axial correlation length of the defects [33]. For correlation lengths shorter than or on the order of the wavelength, the scattering loss exhibits a  $\lambda^{-3}$  dependence,

because the reduction of confinement for longer wavelengths partially counters the Rayleigh scattering. For long correlation lengths compared to the wavelength, a  $\lambda^{-1}$  dependence is observed.

Interface scattering is another loss mechanism present in waveguide structures and is due to roughness at the interfaces between the core and the claddings. Modeling this type of scattering is complex, however it was simplified in [34] by considering the specular reflection of power from a surface and its dependence on the variance of the surface roughness (or r.m.s. roughness). Higher-order modes suffer more interface scattering loss than does the fundamental mode. This is due to differences in optical confinement, and to more reflections per unit length in the direction of propagation for the higher-order modes. This is one of the motives for desiring single-mode operation.

### 2.3.3 Radiation

Radiation loss implies leakage of light from the waveguide into the surrounding media, typically the upper and lower cladding or, for a rib structure, the planar region adjacent to the guide. In addition to guided modes, waveguide structures can also support radiation modes. Optical power carried by the radiation modes disperses as the light propagates and eventually vanishes into the surrounding media. Over a certain distance, all the optical power coupled to the radiation modes will be lost by radiation. These are also known as leaky modes. For a perfect waveguide, the refractive index profile remains the same in the propagation direction and optical power carried by the guided modes cannot be coupled to the radiation modes because of mode orthogonality [35]. In this

case, there is no radiation loss within the waveguide. However, perturbations due to the imperfect fabrication of the waveguide can cause variations in the index profile along the propagation direction. Optical power carried by the guided modes can then be coupled to the radiation modes, and radiation loss occurs. This radiation loss is greater for higher-order modes. Also, waveguides that are not well designed can be leaky. For instance in SOI, if the buried oxide layer is not sufficiently thick, then there can be significant radiation loss into the substrate.

When two waveguides are fabricated in close proximity, each one will act as a perturbation to the other. Although individually these waveguides do not suffer radiation loss, when close enough their evanescent fields overlap, as illustrated in Fig. 2.8, and energy is transferred from one waveguide to the other by radiation (also known as optical tunneling or coupling in this case). This process involves synchronous coherent coupling between the exponential tails of the modes guided in each waveguide. Unwanted coupling becomes more of an issue as the packing density of optical devices on a chip

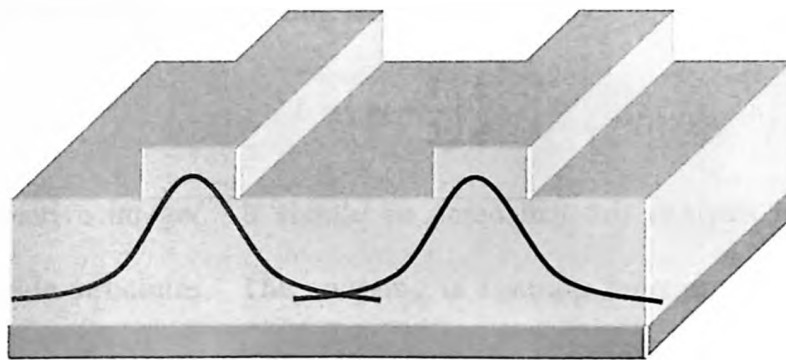


Figure 2.8: Two closely spaced rib waveguides and the overlapping of mode tails.

becomes greater. The coupling of light from one waveguide to another is desired for devices such as directional couplers, beam-splitters and optical switches. The fraction of power coupled per unit length is determined by the overlap of the modes in the separate guides. Thus it depends on the waveguide separation  $s$ , the mode penetration into the space between the guides, which is characterized by the lateral decay constant  $q$ , and the interaction length in the direction of propagation. By using the coupled mode theory approach [36], it can be shown that the normalized power flow in the guides is given by:

$$P_1(z) = \cos^2(\kappa z) \exp(-\alpha z) \quad (2.55)$$

and

$$P_2(z) = \sin^2(\kappa z) \exp(-\alpha z) \quad (2.56)$$

where  $P_1(z)$  and  $P_2(z)$  represent the power in each waveguide,  $\kappa$  is the coupling coefficient, and  $\alpha$  is the attenuation coefficient. From these equations, it can be seen that the power transfers back and forth between the two guides as a function of distance in the propagation direction  $z$ . The total power attenuates exponentially. The length necessary for complete transfer of power (coupling length) is given by:

$$L = \left( m + \frac{1}{2} \right) \frac{\pi}{\kappa} \quad (2.57)$$

where  $m$  is a positive integer. It should be noted that this analysis is based on two identical waveguide structures. The coupling is a strong function of the shape of the mode tails between the waveguides. It was shown in [37] that, for buried channel waveguides, the coupling coefficient is given by:

$$\kappa = \frac{2k_x^2 q \exp(-qs)}{\beta w (q^2 + k_x^2)} \quad (2.58)$$

where  $k_x$  and  $\beta$  are the propagation constants in the  $x$  and  $z$  direction, respectively, and  $w$  is the channel width. The coupling coefficient is a strong function of  $\Delta n$ , which is the difference in index between the channel core and the surrounding semiconductor. It can be shown that for decreasing  $\Delta n$ , the value of  $\kappa$  increases. This means that the coupling length will decrease with more weakly confined electromagnetic waves. This effect would be similar in the rib waveguide coupler shown in Fig. 2.8.

## 2.4 Ion Implantation Damage in Silicon

Lattice defects can arise during common silicon device fabrication processes such as thin film deposition or growth, plasma etching, ion implantation, and combinations of ion implantation and high temperature annealing. This thesis is primarily interested in vacancy-type defects created by ion implantation. This section describes the mechanisms of energy loss experienced by ions in target silicon and the structural modifications (damage) induced by the interactions between the bombarding ions and the silicon atoms. It is discussed how the vacancy-type defect concentration, size, and distribution are determined and how these are influenced by different implantation conditions and subsequent annealing.

### 2.4.1 Ion Stopping Profile

Before discussing the kinetics of damage accumulation in ion-irradiated silicon, it is important to present that of the ion itself. The thickness of a defected layer is related to the ion profile and hence the energy and mass of the implantation species. As the ion penetrates the silicon sample, it will lose energy by means of elastic collisions and electronic drag forces [20]. The rate of ion energy loss with distance traveled in the solid is given by:

$$\frac{dE}{dx} = -N[S_n(E) + S_e(E)] \quad (2.59)$$

where  $S_n(E)$  and  $S_e(E)$  are the nuclear and electronic stopping powers, respectively, and  $N$  is the target atomic density. Since the interactions of moving ions with the nuclei and electrons in the material are strongly dependent on velocity [38], the stopping powers are energy dependent. In general,  $S_n(E)$  increases as the ion loses energy while  $S_e(E)$  decreases. Also,  $S_n(E)$  increases with the atomic mass  $Z$  of the ion, hence nuclear collisions are the dominant energy loss mechanism for heavy ions. For lighter ions,  $S_e(E)$  can be significant especially at higher energies. Since the rate of energy loss is a function of the target silicon density, it will therefore change slightly with crystal orientation. The wafer can be tilted off its crystal axis during implantation such that it "appears" amorphous to the ions and therefore prevents channeling through planes [20].

The projected range  $R_p$  of an ion in silicon is the distance (measured parallel to the incident ion direction) required to reduce its energy to about 15eV such that the ion ceases to move and becomes trapped by cohesive forces in the crystal [38]. Since elastic

collisions are random in nature, the implanted ions will have a distribution about  $R_p$ . This can be modeled by a Gaussian distribution given by:

$$C(x) = C_p \exp\left(-\frac{(x - R_p)^2}{2\Delta R_p^2}\right) \quad (2.60)$$

where  $C(x)$  is the ion concentration at depth  $x$ ,  $C_p$  is the peak concentration, and  $\Delta R_p$  is the standard deviation or straggle about the projected range [20]. The peak concentration can be found by the equation:

$$C_p = \frac{Q}{\sqrt{2\pi}\Delta R_p} \quad (2.61)$$

where  $Q$  is the ion dose. The dose is controlled by the ion implanter, but may not include backscattering effects. Determining the projected range of an ion and its straggle requires a statistical approach. These values can be predicted with Monte-Carlo simulations such as TRansport of Ions in Matter (TRIM) [39]. Fig. 2.9 shows simulations of the projected range (a) and straggle (b) for various energies of  $\text{Si}^+$  ions implanted into silicon.

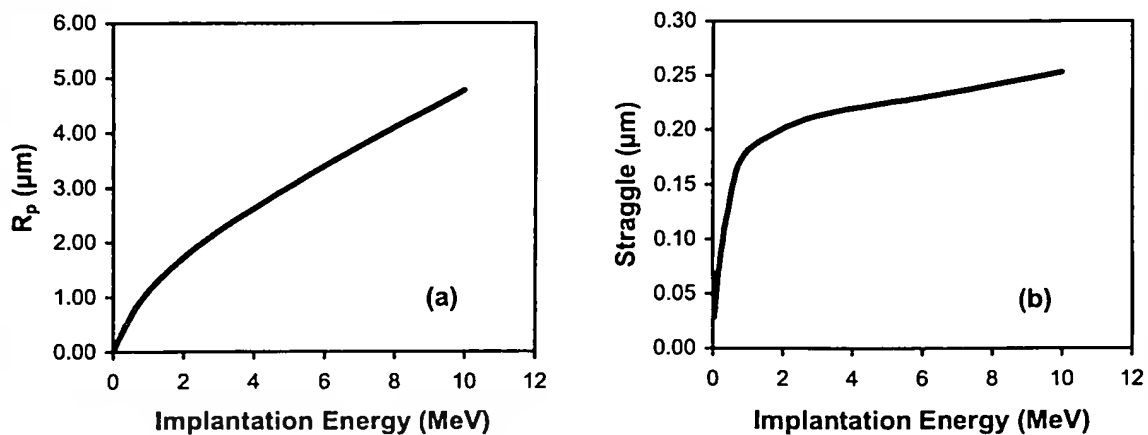


Figure 2.9: TRIM simulations of the projected range (a) and straggle (b) of MeV  $\text{Si}^+$  irradiation of silicon.

### 2.4.2 Vacancy-Type Defects

Implantation-induced damage in crystalline silicon is essentially an accumulation of native point defects, i.e. vacancies  $V$  and interstitials  $I$  [20]. A vacancy is a missing silicon atom at a lattice site while an interstitial is an extra silicon atom that can either sit unbonded between lattice sites or share one lattice site with another silicon atom. A collection of vacancies can agglomerate and form small clusters or even voids in the silicon crystal. A sufficient concentration of vacancies and interstitials can cause silicon to completely amorphize, i.e. lose its crystal structure and become a random assortment of atoms. Vacancy-type defects can also form complexes with the implanted ions or with the impurity ions already in the silicon. Many vacancy-type defects can exist in different charge states, i.e. can exist in neutral states as well as positively or negatively charged states. The dominant charge state will depend on the position of the Fermi level (and hence the original doping of the silicon) relative to the energy level of the defect trap. Evidently, there are a variety of vacancy-type defect structures that can form during ion-irradiation of silicon and these ultimately depend on the chosen implantation parameters, namely the mass and energy of the ion species, the temperature of the substrate, the ion dose, and the dose rate.

### 2.4.3 Defect Accumulation

The interactions between an ion and a solid induce structural modifications due to the transfer of energy from the bombarding ions to the atoms in the target material. In silicon, an energy threshold of around 15eV is required to create a neutral vacancy-

interstitial  $V-I$  pair, also known as a Frenkel pair [40]. If the energy transfer is lower than this threshold, also known as the displacement energy  $E_d$ , then only local heating of the target will occur. When ions transfer much higher energy to target silicon atoms than needed to create a Frenkel pair, the interaction of displaced atoms with other lattice atoms can lead to further displacements, known as recoils. Frenkel pair production is therefore a cascade process. The incident ion is simply the initial damage-producing particle that creates the primary knock-on atoms (PKAs). The total of all subsequent events is commonly referred to as the collision cascade of the ion. The total number of displaced atoms created by a single ion is approximately:

$$n = \frac{E_n}{2E_d} \quad (2.62)$$

where  $E_n$  is the energy lost in nuclear collisions [20]. Some of the defects generated can recombine with defects from other cascades, so the damage accumulation depends on the existing local defect density. The increment in the primary damage in a volume element for an additional implanted ion is given by:

$$\Delta n(x) = n f_r \left( 1 - \frac{N_d}{N_\alpha} \right) \quad (2.63)$$

where  $f_r$  is the fraction of defects that recombine within an isolated cascade and from overlapping cascades,  $N_d$  is the local defect density, and  $N_\alpha$  is the threshold defect density where the crystal is considered to be amorphous. Once amorphized, there is no incremental disorder introduced by further implantation.

Since each ion follows a random trajectory, the associated accumulation of damage, which covers the entire distance traveled by the ion, is inherently a random process. Statistical models permit us to estimate the number of atoms displaced by an ion as it comes to rest and provide an approximate indication of the vacancy profile produced by implantation. For instance, molecular dynamics simulation methods [42], computer simulation codes based on the Kinchin-Pease model [43], and analytical descriptions based on linear Boltzmann transport theory [44] have generally been used for this purpose. The Kinchin-Pease model predicts the number of displaced atoms for a collision cascade starting with initial PKAs and assuming that the collisions are binary, elastic, and made between similar atoms. Molecular dynamics techniques treat the full dynamics of the collision processes, and are consequently more precise for low recoil energies (<200eV) at the expense of being more computationally demanding. TRIM, for example, uses both techniques and allows the user to perform either fast simulations (at the expense of damage detail) or detailed simulations (at the expense of time). It is very difficult to experimentally investigate the displacement cascades generated along the path of an energetic ion beam due to their small volume ( $\sim 10^{-25} \text{cm}^3$ ) and short lifetime ( $\sim 10^{-11} \text{s}$ ). Only indirectly can the primary state of damage be inferred.

Since damage is created throughout the entire ion stopping process, the thickness of the defected layer  $x_d$  is approximately the end-of-range of the ion, which can be approximated by rearranging Eq. 2.60 to give:

$$x_d = R_p \left[ 1 + \sqrt{2 \ln \left( \frac{C_p}{C(x_d)} \right) \frac{\Delta R_p}{R_p}} \right] \quad (2.64)$$

where  $C_p$  is given by Eq. 2.61 and  $C(x_d)$  is the ion concentration that is considered to have a negligible effect on the properties of the silicon sample. Fig. 2.10 shows an example of a fully detailed TRIM simulation of vacancy-type defects produced by

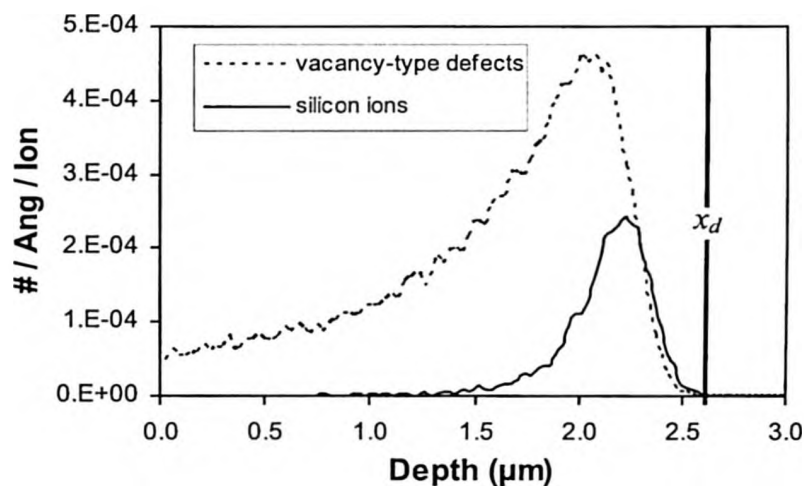


Figure 2.10: TRIM simulation of the vacancy-type defect distribution created by 2.8MeV self-irradiation of silicon.

2.8MeV self-irradiation of silicon. The total thickness of the defect layer  $x_d$  is approximately  $R_p + 3\Delta R_p$ , which is deduced from Fig. 2.9 at an energy of 2.8MeV. From Eq. 2.64, this corresponds to  $C_p/C(x_d)=100$ . The vacancy-type defect concentration  $C_d$  is not uniform throughout this layer. High defect densities are generally located in the vicinity of the ion trajectory. The peak defect density occurs at a depth close to the projected range of the ion, where its velocity is sufficiently slow such that nearly every nuclear interaction results in a displacement event [41]. For heavy ions, the profile of  $C_d$  is relatively flat compared to that caused by lighter ions, which dissipate much of their energy by electronic drag forces before producing significant nuclear displacements.

#### 2.4.4 Influence of Implantation Parameters

The kinetics of damage accumulation is controlled by a competition between displacement cascades and dynamic annealing and is hence influenced by the many parameters associated with the implantation. The mass and energy of the ion species, temperature of the silicon substrate, ion dose, and dose rate all play an interdependent role [45-48]. It is beneficial to be able to reproducibly control the vacancy-type defect concentration  $C_d$  by simply adjusting the implantation parameters as desired. To be able to do this accurately, it is necessary to study the effects of these different parameters on  $C_d$ , which can be measured by various experimental techniques such as InfraRed (IR) spectrometry, X-Ray Diffraction (XRD), Rutherford Backscattering Spectroscopy (RBS), and PAS.

It was demonstrated in [49-51] that during self-irradiation of silicon,  $C_d$  as a function of ion dose is composed of three distinct stages. Initially, the damage accumulates slowly with a sublinear dependence on dose until a critical dose is reached. This stage is associated with relatively simple point defects in crystalline silicon. Then, a rapid superlinear accumulation within a very narrow dose range occurs, which is likely the result of a mixture of point defects, vacancy clusters, and amorphous silicon zones. Finally, the damage saturates beyond a given dose and the silicon is identified as being completely amorphous. Further implantation only causes the widening of the amorphous layer. The work in [51] reported that the initial sluggish increase of  $C_d$  is due to the considerable recombination of point defects at room temperature while the rapid growth

of  $C_d$  that originates at the critical dose is attributed to the reduction of the threshold energy for atomic displacements in a predamaged crystal.

As confirmed by Baranova *et al.* [11],  $C_d$  and the associated change in refractive index increases as the atomic number of the bombarding ion  $Z$  is increased. Also, the onset of amorphization is shifted towards lower dose values for higher values of  $Z$ . In the case of heavier ions, a larger fraction of the incident energy is used in nuclear collisions thus causing more atomic displacements for the same implant energy. Also, heavier ions create a greater variety of damage and larger vacancy clusters. The increase in the observed damage not only comes from the amount of generated vacancies, but mostly because the morphology of the defects strongly influences dynamic annealing and therefore the rate of damage accumulation. For light ions, the electronic losses are higher than in the case of heavy ions, and thus a greater fraction of the total ion energy goes into electronic processes. Also, light ions produce mostly isolated point defects or small vacancy clusters, which have a higher probability of dynamic annealing.

The reduction of implant temperature has effects similar to those associated with the increase in  $Z$  of the bombarding ion. At lower implant temperatures,  $C_d$  increases and amorphization can be achieved at lower doses [52]. The temperature dependence of  $C_d$  is due to the competition between defect accumulation in the energetic collision cascade and damage shrinking associated with defect annihilation or outdiffusion from the damaged region. Beam heating effects could lead to variable results under nominally "identical" conditions unless special care is taken to thermally couple the target silicon to a temperature-controlled holder. For very low implant temperatures (e.g. liquid nitrogen

temperatures), most of the generated damage is retained and the damage rapidly increases with dose.

It was observed in [53] that  $C_d$  increases with increasing dose rate during self-irradiation of silicon at room temperature. This behavior is understood, again, in terms of the balance between damage generation and annihilation. At low temperatures, no dose rate dependence is observed because the dynamic annealing is negligible in the time range of practical dose rates. However, at the critical temperature (close to room temperature in the case of self-irradiation), the dynamic annealing rate will have a significant influence. Low dose rates will produce relatively small net amounts of damage. As the dose rate increases, the time between the arrivals of overlapping cascades decreases, thus resulting in increased damage accumulation. For very high dose rates, the rise in sample temperature may be sufficient to decrease  $C_d$  due to the increased rate of dynamic annealing.

#### 2.4.5 Post-Implantation Annealing

The post-implantation annealing behavior of damaged regions in implanted silicon reveals various stages and temperatures for significant defect recovery, indicating that the damage consists of a hierarchy of several defect structures. As discussed by Corbett *et al.* [10], a single isolated interstitial  $I$  and vacancy  $V$  will diffuse below room temperature, most likely resulting in recombination. The di-interstitial  $I_2$  anneals out at approximately 150°C [54]. Stein *et al.* [55] reported that the divacancy  $V_2$ , which is of greatest significance to the work here, anneals out at 250°C. At a temperature of around

400°C, most of the vacancy-type clusters break up and the released vacancies annihilate with interstitials. The final result of the initial stages of annealing is that most of the Frenkel pairs are removed, leaving only interstitial-type defects whose origin are the extra atoms (or +1 atoms) introduced during the implantation [20].

Depending on the species of ions used, which may substitute for the silicon atoms in the crystal lattice, some of the remaining interstitials may be silicon atoms. Upon further annealing at temperatures above 400°C, the remaining silicon interstitials condense into characteristic rod-shaped defect clusters that lie on {311} planes [56]. If small enough and when annealing above 900°C, these {311} defects may start to dissolve by the evaporation of silicon interstitials from the ends of the rods. However, the larger {311} defects can turn into stable dislocation loops [57], which are essentially extra circular atomic layers of silicon atoms precipitated on {111} planes. These require temperatures above 1100°C to be removed. The disorder created by implantation of light ions recovers faster and to a much greater extent than that produced by heavier ions [58], which create more displacement cascades leading to a higher probability of clustering. Therefore, with heavy ions and/or high doses, dislocation loops are more likely to form upon thermal annealing. The dissolution of these larger defects involves the emission of point defects that diffuse until they are annihilated at the surface.

## 2.5 Optical Properties of Damaged Silicon

This section describes the effects of deliberately introduced defects on the optical properties of silicon. Ion implantation provides a simple technique for modifying the

structure of silicon and is fully compatible with VLSI technology. Of particular importance are the deep levels associated with the silicon divacancy  $V_2$ . The influences of ion implantation damage on optical absorption and refractive index at wavelengths near  $1.55\mu\text{m}$  are discussed in detail.

### 2.5.1 Deep Levels Associated with the Silicon Divacancy

This thesis is focused on describing the effects of low ion implantation doses, well below the amorphization threshold, and hence small-sized defects. Since point defects are extremely mobile in the silicon lattice, most of the single vacancies and interstitials will recombine at room temperature. However, the  $V_2$  is stable at room temperature and, as observed by Coleman, Burrows and Knights [59] (hereafter referred to as CBK), is typically the dominant vacancy-type defect present in moderately irradiated silicon. The structural configuration of the  $V_2$  in the silicon lattice, as declared by Cheng *et al.* [24], is

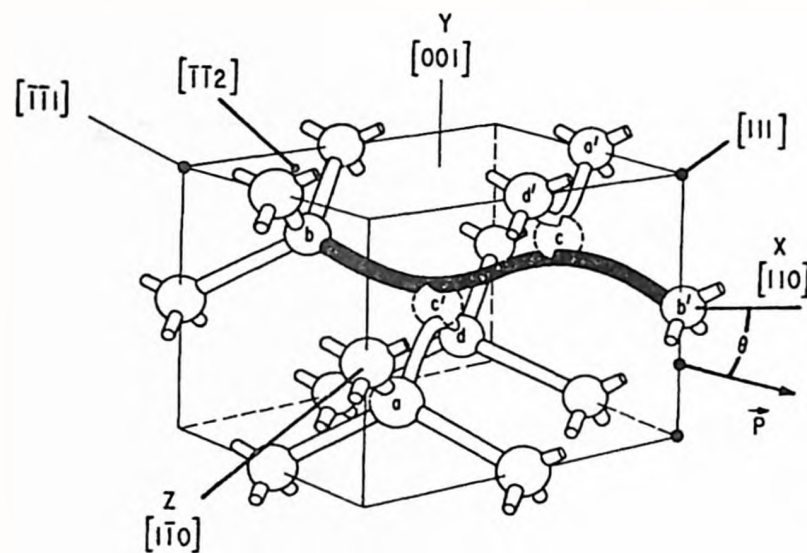


Figure 2.11: Structure of the divacancy in the silicon lattice.

shown in Fig. 2.11. There are essentially two adjacent vacancies designated by the dashed circles  $c$  and  $c'$ . The nearest-neighbor atoms to vacancy  $c$  are labeled  $a'$ ,  $b'$ , and  $d'$  while those to vacancy  $c'$  are labeled  $a$ ,  $b$ , and  $d$ . These authors indicated that the  $V_2$  is symmetric and pair-wise bonding of the vacancy neighbors  $b$  and  $b'$  occurs. The charge state of the  $V_2$  is primarily determined by the filling of the  $b$ - $b'$  orbitals. The  $V_2$  has net charge (+1) for one electron, and charge (0) for two electrons, in the bonding  $b$ - $b'$  orbital. It has charge (-1) for one electron, and (-2) for two electrons, in the antibonding  $b$ - $b'$  orbital. The energy levels in the forbidden bandgap corresponding to these charge states were deduced from Electron Paramagnetic Resonance (EPR) measurements [24] and more recently using High-Resolution PhotoInduced Transient Spectroscopy (HRPITS) [60]. These deep levels, which are indicated in Fig. 2.12, act as carrier traps and provide mechanisms for optical absorption at wavelengths greater than the band-edge. As designated in [60], the levels at  $E_c-0.23\text{eV}$  and  $E_c-0.42\text{eV}$  are electron traps while the level at  $E_v+0.20\text{eV}$  is a hole trap.

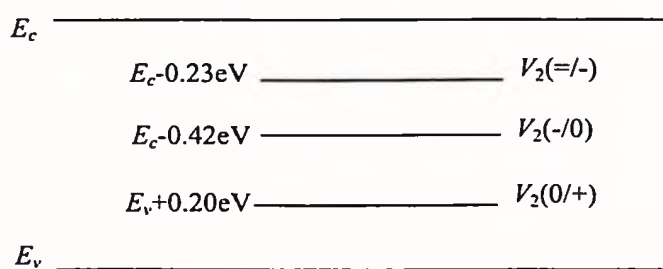


Figure 2.12: Deep levels associated with the silicon divacancy.

### 2.5.2 The 1.8 $\mu\text{m}$ Absorption Band

It has been known for some time that particle irradiation of crystalline silicon creates lattice defects, which in turn cause the absorption of infrared radiation. A prominent absorption band, originally observed by Becker [61] using neutron and deuteron irradiation, is positioned at 1.8 $\mu\text{m}$ . Cheng *et al.* [24] later assigned this band to the silicon divacancy. The 1.8 $\mu\text{m}$  divacancy band was also observed by Stein *et al.* [55] using oxygen implantation, and is shown in Fig. 2.13. Of significance to the work here is the tail of the 1.8 $\mu\text{m}$  band that extends to the absorption edge, which is sharply positioned

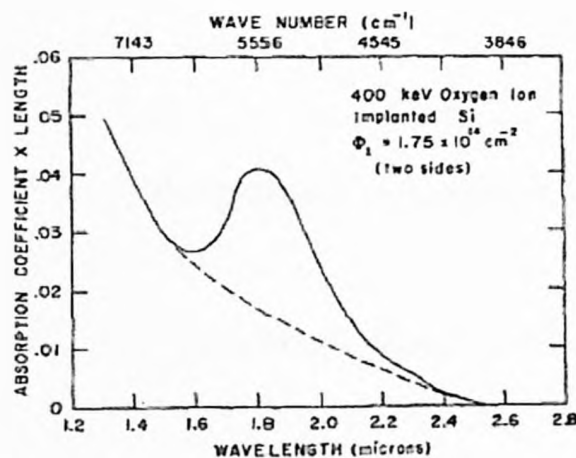


Figure 2.13: The 1.8 $\mu\text{m}$  infrared absorption band associated with silicon divacancies created by implantation of oxygen.

at 1.1 $\mu\text{m}$  in silicon that has not been irradiated. Fan and Ramdas [12] reported that this absorption edge modification is likely due to the presence of divacancies and the associated 1.8 $\mu\text{m}$  band. Since the tail passes through the 1.55 $\mu\text{m}$  telecommunication window, it is of some importance to determine the excess optical absorption in this

wavelength range. It should be noted that ion implantation doses above the threshold value for amorphization, such as those used by de Dood and Polman [18], produce excess absorption at  $1.55\mu\text{m}$  without the distinct  $1.8\mu\text{m}$  divacancy band [62].

### 2.5.3 Implantation-Induced Index Modification

The presence of damage raises the refractive index near the fundamental absorption edge in silicon ( $\lambda=1-2\mu\text{m}$ ), as demonstrated by Baranova *et al.* [11]. The increment of refractive index was measured as a function of implantation dose for a number of different ion species. In each case, the index increases with dose and saturates, behavior similar to that observed for defect accumulation, thus indicating the relationship between defects and refractive index modification. It was suggested that the changes in index are associated with the changes in the relative volume of the amorphous phase within the crystal.

Another consideration is that crystalline defects in silicon induce strain, which alters the refractive index through the photoelastic effect [63]. The strain is a result of the stress that develops due to broken bonds and interstitials produced during the implantation. The change in index is proportional to the strain in the crystal. The photoelastic effect can be considered interrelated to the change in refractive index due to modification of the electronic structure in the presence of defects.

## Chapter 3

# Characterization of Implantation-Induced Defects in Silicon

### 3.1 Beam-Based Positron Annihilation Spectroscopy

The use of Positron Annihilation Spectroscopy (PAS) techniques to characterize defects in shallow regions, where silicon device structures are located, requires monoenergetic beams of slow positrons. This section describes the basics of beam-based PAS before discussing the results of measurements made on ion-irradiated silicon samples. Beam-based PAS is an excellent method for depth profiling of defect concentrations in shallow regions, however it provides only limited information with respect to the exact structure of the vacancy-type defects.

#### 3.1.1 The Positron Beam

One of the most direct methods for determining the concentration of vacancy-type defects in ion-irradiated silicon is the use of a slow positron beam. High energy positrons are produced either by pair production in a target bombarded with very high energy ( $\sim 100$  MeV) electrons or by the decay of radioactive isotopes such as  $^{22}\text{Na}$  [64]. These positrons are moderated, typically with tungsten, to a narrow energy width ( $\sim 1$  eV) before being extracted into a beam and accelerated by a combination of electric and magnetic

fields. The positron penetrates the target sample, thermalizes, and diffuses before possibly becoming trapped in a lattice defect. Eventually, the positron annihilates with an electron resulting in the production of a pair of 511keV  $\gamma$ -quanta. These  $\gamma$ -quanta are detected, giving information about the defects in the sample. Positron beams can have low energies such that very shallow regions ( $<1\mu\text{m}$ ) of the silicon can be probed. The beam energy can be varied such that depth profiling of shallow defected layers can be achieved. This technique has been described in detail previously [65].

Knowledge of positron implantation profiles is important when using low energy beams to analyze thin layers of defects. The implantation profile describes the distribution of positrons in a sample after thermal equilibrium has been achieved. During the slowing down process, positrons lose energy mainly by means of inelastic collisions. Modeling of these collisions requires a statistical approach. Implantation distributions of slow monoenergetic positron beams have been well described in the past. The most widely used model to describe the distribution of implanted positrons as a function of depth  $z$  is the Makhov profile [66], which takes the form of a Gaussian derivative given by:

$$P(z, T) = \frac{mz^{m-1}}{z_0^m} \exp\left[-\left(\frac{z}{z_0}\right)^m\right] \quad (3.1)$$

where  $z_0$  is the mean penetration depth and is given by:

$$z_0 = \frac{AT^r}{\rho\Gamma\left(1 + \frac{1}{m}\right)} \quad (3.2)$$

where  $T$  is the kinetic energy of the positrons in the beam,  $\Gamma$  is the gamma function, and  $\rho$  is the mass density of the sample. The parameters  $r$ ,  $m$ , and  $A$  are empirical values commonly taken to be  $r=1.6$ ,  $m=2$ , and  $A=4.0\mu\text{gcm}^{-2}\text{keV}^{-r}$  for silicon [67]. These parameters have been obtained from Monte-Carlo simulations and were shown to be material dependent [68]. The Monte-Carlo approach was used by Baker *et al.* [69] to fit profiles that differ slightly from the Gaussian derivative form and have an energy dependent  $r$  given by an equation of the form:

$$r(T) = a + b \ln(T) \quad (3.3)$$

where  $a$  and  $b$  are experimental fit parameters. In any case, the positron implantation profile broadens as  $T$  increases, meaning that depth profiling becomes more difficult in deeper regions of the target.

### 3.1.2 Doppler Broadening Technique

Most common in the study of thin layers are positron beams that utilize the Doppler broadening measurement technique. A Doppler shift of the annihilation energy is a result of momentum conservation during the annihilation process. Since the positron is thermalized before it annihilates with an electron, the Doppler shift reflects the electron momentum at the annihilation site. Vacancy-type defect structures are dominated by low-momentum electrons, resulting in a more narrow annihilation energy distribution [27]. Using a line shape parameter  $S$ , which reflects the average momentum of electrons at the annihilation sites, the annihilation energy distribution can be analyzed. In general, an increase in the value of  $S$ , relative to that for a sample that is essentially defect-free,

indicates the presence of open-volume or vacancy-type defects. For consistency, the measured  $S$  parameter is normalized to the value measured for a defect-free reference sample. The amount by which  $S$  increases above unity therefore reflects both the defect size and total concentration within the defected sample.

Assuming that the dominant vacancy-type defects as seen by the positrons are similar in size to the divacancy (i.e. they can be considered similar to point defects) as in the work by CBK [59] and the literature [65], the concentration of defects  $C_d$  at a given depth in the silicon sample can be reliably determined using:

$$S = (1 - F_d)S_b + F_d S_d \quad (3.4)$$

$$F_d = \left(1 + \frac{\lambda_b}{\nu C}\right)^{-1} \quad (3.5)$$

$$C_d = AC \quad (3.6)$$

where  $S$  is the measured data at the depth (or positron energy) of interest,  $S_b$  is the bulk reference value (forced to unity),  $S_d$  is the value characteristic of the divacancy (previously determined to be 1.042),  $F_d$  is the fraction of positrons trapped at divacancies,  $\lambda_b$  is the annihilation rate of positrons in defect-free bulk silicon ( $4.55 \times 10^9 \text{s}^{-1}$ ),  $\nu$  is the defect specific trapping coefficient for positrons at divacancies ( $1 \times 10^{15} \text{s}^{-1}$ ),  $C$  is the defect concentration per atom in the silicon lattice, and  $A$  is the atomic density of silicon ( $4.976 \times 10^{22} \text{cm}^{-3}$ ).

Of significant interest in this study is how the concentration of defects scales with ion implantation dose. This was the principal motivation for the work by CBK, who used the Doppler broadening technique to analyze silicon samples implanted with a wide range

of ion species, doses and energies. This study resulted in the formulation of a simple analytical equation allowing the reliable prediction of vacancy-type defect concentration at half ion range following implantation:

$$C_d = (2.79 \times 10^{10}) \phi_A^{0.63} \quad (3.7)$$

where  $\phi_A$  is the adjusted ion dose, obtained by multiplying the actual dose by a factor equal to the vacancies per ion per angstrom at half ion range determined using TRIM simulations.

### 3.1.3 Beam Measurements made on MeV Ion-Irradiated Silicon

Two different implantation species ( $\text{Si}^+$  and  $\text{H}^+$ ) were used to study the accumulation of defects with ion dose. In both cases, the effects of high energy (MeV) irradiation of ions were investigated using beam-based PAS. All implantations were performed at the University of Western Ontario using their 1.7MV Tandatron accelerator. The circular aperture size was  $5.7\text{cm}^2$ , large enough to expose the entire surface of the samples. The samples were tilted  $7^\circ$  relative to the beam direction in order to minimize the amount of ion channeling. The  $\text{Si}^+$  implantations were carried out at room temperature while the  $\text{H}^+$  implantations were performed with the samples at liquid  $\text{N}_2$  temperature. In both cases, the ion beam currents were kept low enough ( $<3\mu\text{A}$ ) to avoid significant increases in the temperature of the target silicon. Doppler broadening measurements of the line shape parameter  $S$  for positron energies in the range of 0.5 to 30keV were performed at the University of Bath, U.K.

Fig. 3.1 shows data obtained from Doppler broadening measurements made on a set of four samples cleaved from p-type Cz silicon <100> wafers doped with boron and

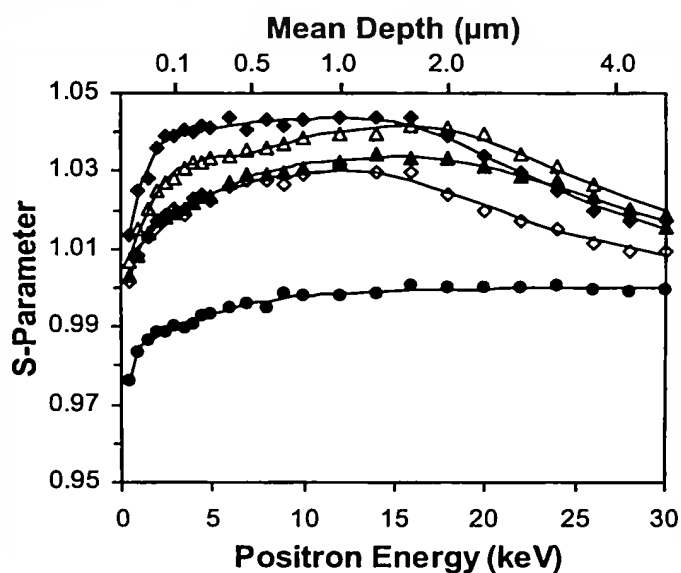


Figure 3.1:  $S$  parameter data obtained for silicon irradiated with 2.8 MeV  $\text{Si}^+$  to doses of  $4 \times 10^{12} \text{cm}^{-2}$  (open diamonds),  $1.6 \times 10^{13} \text{cm}^{-2}$  (closed triangles),  $6.3 \times 10^{13} \text{cm}^{-2}$  (open triangles), and  $2.5 \times 10^{14} \text{cm}^{-2}$  (closed diamonds). Also shown is data for not irradiated silicon (closed circles). The raw data were fitted using VEPFIT (solid lines).

having a resistivity of 1-10  $\Omega\text{cm}$ . These samples were irradiated with 2.8 MeV  $\text{Si}^+$  to doses of  $4 \times 10^{12} \text{cm}^{-2}$ ,  $1.6 \times 10^{13} \text{cm}^{-2}$ ,  $6.3 \times 10^{13} \text{cm}^{-2}$ , or  $2.5 \times 10^{14} \text{cm}^{-2}$ . The  $S$  parameters are normalized to the bulk value for a low-doped, Cz silicon reference sample where the concentration of vacancies is assumed to be well below the sensitivity level of the PAS technique. The data for this reference sample is also shown. For each implantation dose, the measured  $S$  parameter data were well-fitted using VEPFIT software [70]. These fitted curves are shown in Fig. 3.1 by the continuous lines. Extrapolation of these fitted  $S$  parameter curves to zero positron implantation energy yields the value associated with

the silicon surface (here  $\sim 0.95$ ). For incident positron energies above about 10keV, diffusion to the surface is negligible and positrons annihilate with electrons in the bulk of the silicon or in defect sites. The increase in  $S$  above unity at these depths is due to the presence of vacancy-type defects created by the  $\text{Si}^+$  implantation. The  $S$  parameter for 14keV positrons in Fig. 3.1 increases with increasing  $\text{Si}^+$  dose as expected. At the highest dose, the saturation value of  $S$  is above 1.042 (similar to observations of CBK)

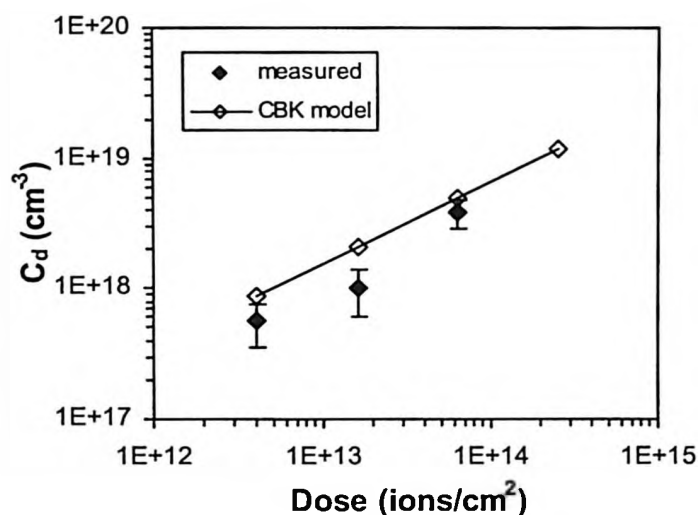


Figure 3.2: Effective divacancy concentration versus ion dose for 2.8MeV  $\text{Si}^+$  irradiation of silicon.

indicating that a small fraction of the defects are somewhat larger than the divacancy. Above 16keV, a significant fraction of the positrons annihilate within the undefected substrate, beyond the end-of-range of the ion implantation, and hence the  $S$  parameter is reduced relative to the peak value. The effective divacancy concentrations were calculated using the values of  $S$  at 14keV in Eqs. 3.4, 3.5, and 3.6. The results are shown in Fig. 3.2 for all the implantation doses (except the highest) used in the experiment. Using the saturated data for the highest dose would lead to  $F_d > 1$ , which is an impossible result. This dose also lies beyond the range for which the CBK model has been verified.

Also shown are the values calculated from the CBK model, given by Eq. 3.7, with which good agreement is found. The dose adjustment factor used in this model was simulated by TRIM to be  $\sim 0.2$ . This is the vacancies per ion per angstrom at a depth of  $1.3\mu\text{m}$ , which is the mean depth probed by  $14\text{keV}$  positrons as calculated using Eq. 3.2.

Doppler broadening measurements were also made on samples irradiated with  $\text{H}^+$  ions. These samples again came from p-type Cz silicon  $\langle 100 \rangle$  wafers doped with boron

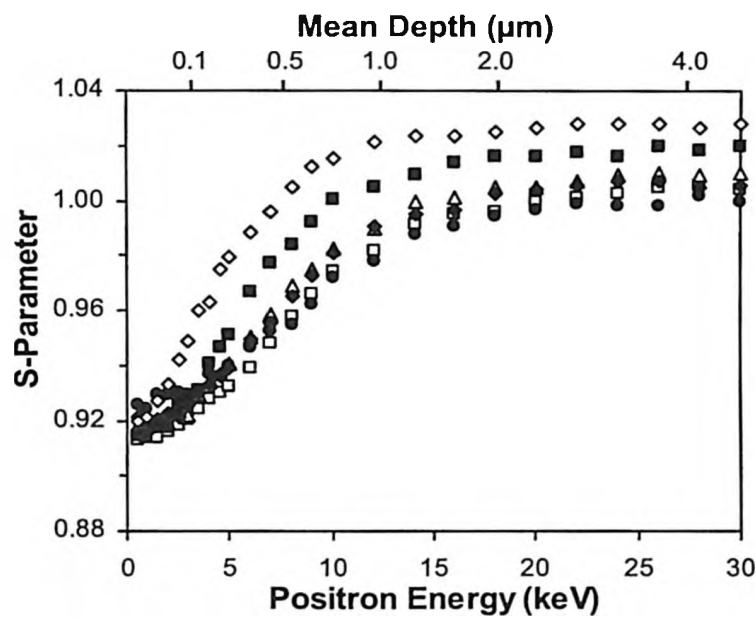


Figure 3.3:  $S$  parameter data obtained for silicon irradiated with  $1.5\text{MeV H}^+$  to doses of  $1 \times 10^{14}\text{cm}^{-2}$  (open squares),  $3 \times 10^{14}\text{cm}^{-2}$  (closed diamonds),  $1 \times 10^{15}\text{cm}^{-2}$  (open triangles),  $3 \times 10^{15}\text{cm}^{-2}$  (closed squares), and  $1 \times 10^{16}\text{cm}^{-2}$  (open diamonds). Also shown is data for not irradiated silicon (closed circles).

and having a resistivity of  $1\text{-}10\Omega\text{cm}$ . In this case, five samples were irradiated with  $1.5\text{MeV H}^+$  to doses of  $1 \times 10^{14}\text{cm}^{-2}$ ,  $3 \times 10^{14}\text{cm}^{-2}$ ,  $1 \times 10^{15}\text{cm}^{-2}$ ,  $3 \times 10^{15}\text{cm}^{-2}$ , or  $1 \times 10^{16}\text{cm}^{-2}$ . For each dose, the measured  $S$  parameter, shown in Fig. 3.3, saturates at a positron energy less than  $30\text{keV}$  and does not fall off after saturation. This is because the end-of-range of  $1.5\text{MeV H}^+$  is much greater than the mean depth of  $30\text{keV}$  positrons. The saturation  $S$

parameter increases with increasing dose and is above unity for all doses indicating the presence of vacancy-type defects created by the  $H^+$  implantation. However, in this case, the saturation values are all significantly less than 1.042, suggesting that there are fewer divacancies in these samples than in the  $Si^+$  irradiated samples. This is an expected result since  $H^+$ , which has a much lower atomic mass than  $Si^+$ , is less likely to produce atomic displacements during the slowing down process. The effective divacancy concentrations were calculated using the values of  $S$  at 30keV in Eqs. 3.4, 3.5, and 3.6. These results are shown in Fig. 3.4 along with the values calculated from the CBK model, this time using the vacancies per ion per angstrom factor at a depth of  $4.5\mu m$ , which is the mean depth calculated by Eq. 3.2 for 30keV positrons. In this case, the factor was simulated by TRIM to be  $\sim 0.00003$ .

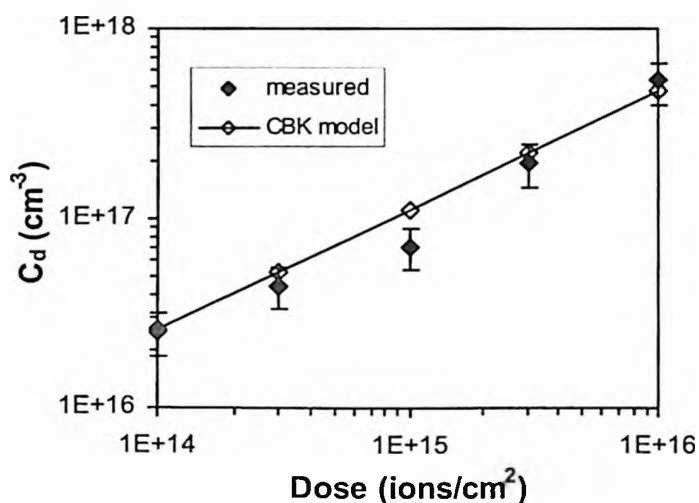


Figure 3.4: Effective divacancy concentration versus ion dose for 1.5MeV  $H^+$  irradiation of silicon.

The agreement of the CBK model with the results of this study is within experimental uncertainty. The data obtained from the  $H^+$  irradiated silicon samples show

a sublinear accumulation of vacancy-type defects with implantation dose and can be fit with an exponent of 0.66, which is very close to that obtained by CBK (0.63). This suggests that the CBK model can be used to reliably predict defect concentrations at depths other than half ion range as long as the proper dose adjustment factor is used from the TRIM simulations. However, as recommended by CBK, caution must be taken since the vacancy-type defect profiles simulated by TRIM may not be accurate for some ion implantation conditions.

### 3.2 Positron Annihilation Lifetime Spectroscopy

Another positron technique used to characterize defects is positron annihilation lifetime spectroscopy (PALS). This section describes the basics of PALS, which typically requires a radioactive positron source placed in close proximity to the sample under study, bypassing the moderation step. The PALS technique is, in principle, more powerful than the Doppler broadening technique as one can accurately determine both the type of defect present and its concentration. However, since radioactive isotopes, such as the conventional  $^{22}\text{Na}$  source, emit positrons with a continuous energy spectrum up to a maximum energy, this technique is normally limited to characterization of defects in bulk materials with no information on defect profiles. In this section, an accurate implantation profile describing positrons emitted from a  $^{22}\text{Na}$  source is suggested and experimentally verified for silicon targets. This profile is then used to perform positron lifetime measurements on defected layers, created by ion-irradiation of silicon.

### 3.2.1 The Lifetime Technique

The positron lifetime measurement is triggered via a 1.27MeV  $\gamma$ -quantum that is emitted simultaneously with the positron in the  $^{22}\text{Na}$  source [64]. The lifetime of a single event can be measured by detecting the time difference between the birth  $\gamma$ -quantum of the  $\beta^+$  decay in the source and one of the annihilation  $\gamma$ -quanta from the sample. The positron lifetime is a function of the local electron density, therefore gives an accurate measurement of the average size of the open volume defects present. Although uncommon, measurements of this sort are desired for characterization of shallow layers in the sample. Since positron beams typically lack an accurate trigger signal due to the low efficiency of the moderation process, the lifetime measurement is difficult to perform using slow positrons. Such measurements are generally limited to highly specialized and high-cost positron beam set-ups [71].

With a  $^{22}\text{Na}$  source placed next to the target sample, the birth  $\gamma$ -quantum (trigger) can be utilized to make reproducible lifetime measurements. The time-dependent positron decay spectrum  $D(t)$  in the bulk target sample is given by:

$$D(t) = \sum_{i=1}^{k+1} I_i \exp\left(-\frac{t}{\tau_i}\right) \quad (3.8)$$

where  $k$  is the number of defect types, with individual positron lifetimes  $\tau_i$  and corresponding intensities  $I_i$  [27]. If no positron traps are present, there will be only one component lifetime  $\tau_b$  that represents the positron lifetime in the defect-free bulk of the sample. The lifetime spectrum  $N(t)$  is the absolute value of the time derivative of  $D(t)$  and is given by:

$$N(t) = \sum_{i=1}^{k+1} \frac{I_i}{\tau_i} \exp\left(-\frac{t}{\tau_i}\right) \quad (3.9)$$

which, when represented on a semi-logarithmic plot, can be decomposed into straight lines that represent the individual lifetime components. Standard software based on Gauss-Newton non-linear fitting routines is available for the decomposition of the measured annihilation spectra. The experimentally obtained spectra differ from the analytical description of Eq. 3.9 mainly by the convolution with the time resolution function, which can be represented by a Gaussian  $G(t)$ , and by an almost constant background contribution. The resolution function is a result of the statistical fluctuations in the time delay of the measurement equipment.

Assuming the vacancy-type defects are homogeneously distributed in the sample volume, and do not interact with each other, their concentration and average size can be determined through the trapping model [72,73]. With further assumption of one defect type, the positrons can annihilate either in the bulk or in the defect, and a two-component fit to the annihilation spectrum results in the following relations:

$$\tau_1 = \tau_{mb} = \frac{1}{\lambda_b + \kappa_d} \quad (3.10)$$

$$\tau_2 = \tau_d = \frac{1}{\lambda_d} \quad (3.11)$$

$$I_1 = I_{mb} = 1 - I_2 \quad (3.12)$$

$$I_2 = I_d = \frac{\kappa_d}{\lambda_b - \lambda_d + \kappa_d} \quad (3.13)$$

$$C_d = A \frac{\kappa_d}{\nu} \quad (3.14)$$

where  $\tau_{mb}$  is the modified bulk lifetime (or the reduced positron lifetime in the bulk),  $\tau_d$  the positron lifetime in the defect,  $\kappa_d$  the positron trapping rate associated with the defect,  $\nu$  the defect specific trapping coefficient ( $1 \times 10^{15} \text{s}^{-1}$  for divacancies), and  $A$  is the atomic density of the sample ( $4.976 \times 10^{22} \text{cm}^{-3}$  for silicon). The annihilation rate of positrons in the defect  $\lambda_d$  is just the reciprocal of the lifetime  $\tau_d$ . When positrons get trapped in open volume defects where the electron density is reduced, the lifetime of the positron will increase relative to the defect-free bulk lifetime. Hence  $\tau_d$  gives a measure of the average size of the open volume defects throughout the entire sample. As the number of defect traps increases,  $\tau_{mb}$  will decrease since the survival time of the positrons in the bulk material is shortened. The defect concentration is directly proportional to the measured trapping rate.

### 3.2.2 Sandwich Configuration with $^{22}\text{Na}$ Source

PALS typically requires a continuous positron source placed in close proximity to the sample under study, providing not only a supply of positrons but also a simultaneous gamma decay, which can be used as a trigger in the lifetime measurement. The positrons must immediately penetrate the target sample after being created, such that their lifetime is characteristic of the sample being measured. Since radioactive sources emit positrons isotropically, this is achieved by placing the  $^{22}\text{Na}$  source directly between two identical samples as shown in Fig 3.5. This is known as the “sandwich” configuration [27].

Scintillator-photomultiplier detectors are situated on both sides of the sandwich to detect the birth  $\gamma$ -quantum (start signal) and the pair of 511 keV  $\gamma$ -quanta (stop signal), which are emitted in opposite directions when a positron annihilates. The lifetime is measured as the time difference between the appearance of the start and stop  $\gamma$ -quanta. By charging a capacitor, a time-to-amplitude converter converts this time difference into a proportional voltage signal. The complete lifetime spectrum  $N(t)$  is stored in a multi-channel analyzer.

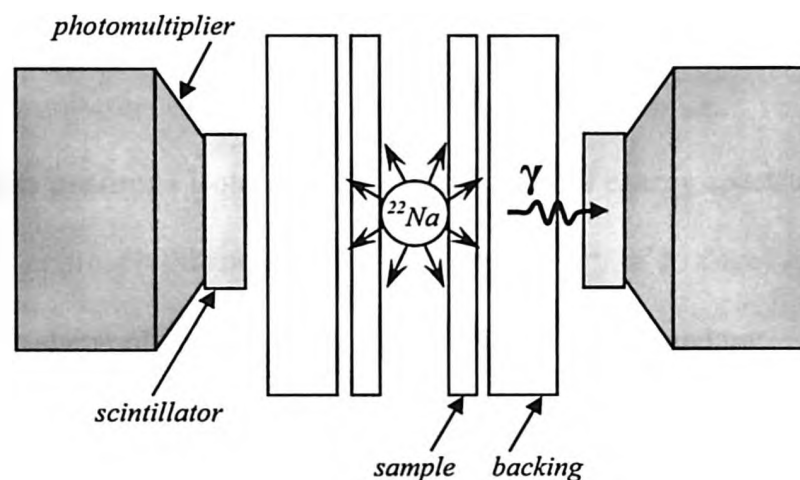


Figure 3.5: The sandwich configuration used in conventional PAS.

Generally, the samples must be thick enough to stop all positrons, such that all annihilations take place in the target material. In the case of silicon, thicknesses  $>400\mu\text{m}$  are required. For smaller sample thicknesses, a backing material can be used in a bi-layer sandwich configuration. This technique is described in detail in section 3.2.4. Since  $^{22}\text{Na}$  sources emit a broad spectrum of positron energies, the implanted positrons will have a broad spatial distribution in the sample. With complete absorption of the positrons and a uniform concentration of defects throughout the sample, the implantation profile of the

positrons is irrelevant. However, when introducing damage via ion implantation, the defects will form in the region from the sample surface to a depth of  $R_p$  + a few  $\Delta R_p$ . In this case, knowledge of the positron implantation profile is important in order to determine the percentage of positrons probing the defected region.

### 3.2.3 Implantation Profile of Positrons from a $^{22}\text{Na}$ Source

The distribution of implanted positrons produced by a continuous radioactive source has no straightforward and accurate analytical description. This is because any such source emits positrons isotropically and over a wide energy spectrum. Nonetheless, one can initially approach this problem by using the theory of  $\beta^+$  decay as in [74] where it is shown that the shape of any  $\beta^+$  emission spectrum is determined by:

$$Q(p, E) = kp^2 (E_{\max} - E)^2 F(p) \quad (3.15)$$

where  $p$  is the momentum of the positron,  $E$  is its total energy,  $E_{\max}$  is the endpoint energy of the spectrum,  $F(p)$  is the Fermi function, and  $k$  is a normalization factor. The Fermi function is approximated by:

$$F(p) \approx \frac{2\pi\eta}{1 - \exp(-2\pi\eta)} \quad (3.16)$$

with:

$$\eta = -\frac{Ze^2 m_0}{4\pi\epsilon_0 \hbar p} \quad (3.17)$$

where  $Z$  is the atomic number of the source material,  $e$  the positron charge,  $m_0$  the positron rest mass,  $\epsilon_0$  the permittivity of free space, and  $\hbar$  the Planck constant. The  $\beta^+$

emission spectrum  $Q(p,E)$  given by Eq. 3.15 is written, for simplicity, in terms of positron momentum and total energy. However, using the relativistic relation:

$$E^2 = (m_0c^2)^2 + (pc)^2 \quad (3.18)$$

and the relation between total energy and kinetic energy:

$$E = T + m_0c^2 \quad (3.19)$$

where  $c$  is the speed of light in free space, Eq. 3.15 can be rearranged to be solely a function of the positron kinetic energy. In this manner, the  $\beta^+$  spectrum, now  $Q(T)$ , can be convoluted with the Makhov profile  $P(z,T)$  given by Eq. 3.1. This convolution represents the implantation profile of positrons emitted from a radioactive source and immediately penetrating the target sample. It is written as:

$$PQ(z) = \int_0^{T_{max}} P(z,T)Q(T)dT \quad (3.20)$$

where the upper limit  $T_{max}$  is the endpoint kinetic energy of the emission spectrum. Eq. 3.20 can be thought of as the superposition of monoenergetic Makhov profiles, weighted appropriately for each positron energy in the  $\beta^+$  emission spectrum. One might be suspicious about the fact that the Makhov profile is normally used to model collimated positrons while radioactive sources emit positrons isotropically. However, collimated positrons rapidly become isotropic when penetrating a dense target [75], suggesting that the implantation profile has no significant dependence on the spatial distribution of the incident positrons. The integration in Eq. 3.20 is quite complex but can be solved numerically.

In the case of a  $^{22}\text{Na}$  source,  $T_{max}=540\text{keV}$  as indicated in [74]. For higher positron energies, the implantation profile becomes broader, possibly leading to increasing uncertainty in the Makhov model. The profile described in the Makhov model has only been thoroughly tested for positron energies  $<50\text{keV}$  [66], and little or no data exists for higher energies. However, the empirically determined parameters of this model are subjective [76,77] and may be altered to better represent experimental data. The employment of an energy dependent  $r$  parameter, as described by Baker *et al.* [69] and shown in Eq. 3.3, will later be revealed as an important feature when fitting Eq. 3.20 to the experimental results of this study.

### 3.2.4 Experimental Verification of New Model

Presented here is the experimental verification of the newly suggested model for the implantation profile of positrons from a  $^{22}\text{Na}$  source given by Eq. 3.20. The simplest form of verification is made by using a bi-layer sandwich configuration consisting of a silicon sample thin enough to allow a significant fraction of the positrons to pass through, and a backing layer (of different material) thick enough to stop all of the transmitted positrons. Knowing the bulk lifetimes of the silicon and backing material,  $\tau_1$  and  $\tau_2$ , respectively, a two-component fit to the annihilation spectrum results in two intensities  $I_1$  and  $I_2$  representing the fractions of positrons annihilating in the silicon and backing material, respectively. The implantation profile in Eq. 3.20 predicts the fraction in the silicon to be:

$$I_{\text{model}} = \int_0^d PQ(z)dz \quad (3.21)$$

where  $d$  is the thickness of the silicon sample. Repeating this bi-layer PALS experiment for several sample thicknesses provides a rigorous test of the positron implantation model. Similar methods have been used previously, for instance to test the transmission of positrons through thin aluminum foils [78].

Generally, the backing material in such an experiment not only has a different positron lifetime than that for silicon, it also has a different mass density. Hence, positron scattering between the silicon sample and the backing must be accounted for. As positrons penetrate through the sample, some will backscatter from the backing and implant into the sample, resulting in more positrons annihilating in the sample than predicted. Also, some positrons will backscatter from the sample and implant into the source, which is usually contained in an aluminum foil. These factors must be considered when verifying the model for the implantation profile. It was shown in [79] that the backscattering coefficient associated with positrons emitted from  $^{22}\text{Na}$  is empirically given by the relation:

$$\beta = 0.342 \log_{10} Z - 0.146 \quad (3.22)$$

where  $Z$  is the atomic number of the backscattering material. This coefficient will decrease, however, in the case where positrons are transmitted (with a concomitant energy loss) through a thin sample before being backscattered. It was demonstrated in [80] that the amount of positron backscattering decreases with decreasing energy. A further complication results from the possibility of multiple scattering between materials

with different densities. This will also effectively decrease the value of  $\beta$  for the backing material. Hence, in this analysis, Eq. 3.22 can be used only as an indication for the maximum fraction of positrons that will backscatter from the backing layer into the sample. If the value of  $\beta$  were accurately known, it would be possible to correct the model for the implantation profile using the equation:

$$I_{1corrected} = I_{1model} + \beta(1 - I_{1model}) \quad (3.23)$$

where  $I_{1corrected}$  is the intensity predicted to be implanted into the sample after accounting for backscattering. However, without accurate knowledge of  $\beta$ , it is sensible to instead use the two extreme limits for  $I_{1corrected}$  and compare these with the experimental measurement. The range of  $I_{1corrected}$  therefore depends on the range of  $\beta$ , which extends from a lower limit of  $\beta=0$  to an upper limit given by Eq. 3.22.

The fraction associated with positrons implanting in the source is typically subtracted from the annihilation spectra using a source correction. In this context, the source is actually considered to be the aluminum container since the thickness of the  $^{22}\text{Na}$  droplet is negligible. Accurately modeling this is difficult given that, as the aluminum foil is normally a few  $\mu\text{m}$  thick, the positrons pass through many times while backscattering from the sample on both sides of the source. For the set-up used in this study, the fraction of positrons annihilating in the source was determined experimentally [81] and is taken as  $\sim 5\%$  for a silicon sample and  $2\mu\text{m}$  aluminum foil.

The samples used in this experiment came from n-type Cz silicon  $\langle 100 \rangle$  wafers doped with phosphorus and having a resistivity of  $5\text{-}10\Omega\text{cm}$ . The starting wafer thickness was  $\sim 388\mu\text{m}$ . This was cleaved into  $1\text{cm}^2$  samples before thinning. To test the

implantation profile properly using the bi-layer sandwich configuration, it was necessary to have two uniform samples of equal thickness. Thinning was attempted using a mechanical polishing process that tended to produce a wedge shape with a uniformity of  $\pm 12\mu\text{m}$ , which was not adequate for this experiment. However, using a chemical etching process, it was possible to thin samples with a uniformity of  $\pm 2\mu\text{m}$ , which was deemed sufficient for proper verification of the implantation profile. To achieve these results, the samples were thoroughly cleaned prior to etching such that any etch-masking contaminants on the surface were eliminated. This was done using a procedure described in [82] that included a solvent clean,  $\text{H}_2\text{O}_2:\text{H}_2\text{SO}_4$  clean, and oxide-removing immersion in buffered HF. The etching was performed using a solution containing 30g of KOH and 100mL of DI water placed in a water bath maintained at  $80^\circ\text{C}$ . In order to produce a pair of samples of equal thickness, two were etched simultaneously in the same solution. To achieve a high level of uniformity, it was necessary to ensure that the samples were subject to the same etch rate across the entire surface and on both sides. Since the etch

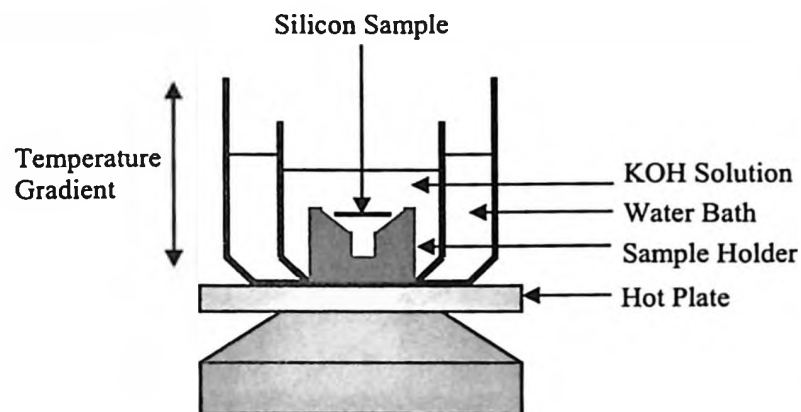


Figure 3.6: Setup required for optimum etching uniformity. Since the sample is perpendicular to the temperature gradient and exposed on both surfaces, the etch rate is constant across the surface on both sides of the sample.

rate is strongly dependent on temperature, any temperature gradient across the surface would produce a non-uniform sample, especially when etching for long periods of time as required in this experiment. The water bath was heated with a hot plate, which generates a significant temperature gradient in the vertical direction, as shown in Fig. 3.6. Therefore the samples were placed horizontally in the solution such that their surfaces were perpendicular to this temperature gradient. In order to expose both sides properly, a custom-built sample holder, also shown in Fig. 3.6, was made from a block of Teflon. This consisted of a countersunk hole through the top, designed to wedge in the sample such that both surfaces were exposed, and another hole through the side, which allowed the KOH solution to flow and replenish the active ions near the bottom surface of the silicon sample.

Each sample etch was timed followed by a thickness measurement using a  $\pm 1\mu\text{m}$  BATY<sup>®</sup> micrometer. With these measurements, an etch rate was estimated and used for each successive sample etch. In this fashion, ten sample thicknesses were produced ranging from  $\sim 388\mu\text{m}$  to  $\sim 60\mu\text{m}$ . The micrometer was used at several points across the

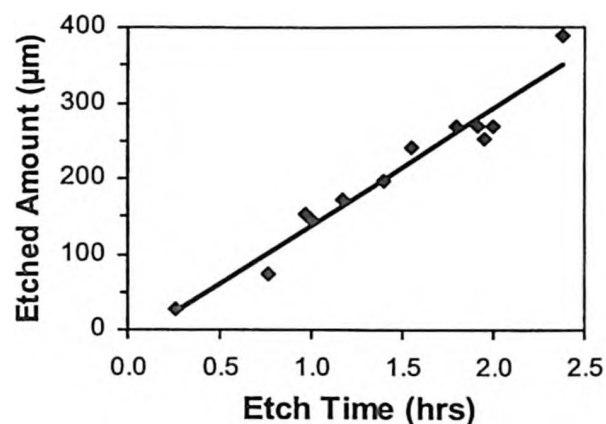


Figure 3.7: Etch rate of silicon using the setup shown in Fig. 3.6 with a 23% KOH solution at  $80^{\circ}\text{C}$ . The slope of the linear fit to the data is  $155\mu\text{m/hr}$ .

surface of each sample, and an average uniformity of  $\pm 2\mu\text{m}$  was determined. Considerable etch times (on the order of hours) were necessary to remove these large amounts of silicon. Since typical applications of chemical etching require etch times on the order of seconds, the degree of uniformity achieved in this experiment is noteworthy. As is shown in Fig. 3.7, the etched amount is a linear function of etch time with a slope of  $\sim 155\mu\text{m/hr}$  (or  $\sim 77.5\mu\text{m/hr}$  per side). Remarkably, this plot indicates that the etch rate remains essentially constant for  $>2\text{hrs}$ .

Once the silicon samples were thinned and ready for PALS measurements, they were placed in the bi-layer sandwich configuration using copper as the backing material. Copper was chosen since its mass density is much larger than that of silicon, and hence its positron lifetime is inherently much shorter [27]. With a high contrast in lifetimes, the positron intensity components are easily separated from the annihilation spectra. The slabs of copper, which were  $\sim 600\mu\text{m}$  thick (sufficient to stop all transmitted positrons), were cleaned using a solution containing 33%  $\text{HNO}_3$ . For each silicon thickness, four lifetime spectra with at least  $6 \times 10^6$  counts were accumulated using a spectrometer with a resolution function  $G(t)$  having a FWHM of 230ps. These spectra were analyzed using code from PATFIT-88 [83,84]. A measurement was made with the  $^{22}\text{Na}$  source directly deposited on the copper, resulting in an average lifetime component of  $116 \pm 2\text{ps}$ . This was also performed using silicon, double stacked to stop all positrons, resulting in a  $220 \pm 2\text{ps}$  lifetime. With the bulk lifetimes fixed at these values, each spectrum was decomposed using a two-component fit, allowing the fractions of positrons annihilating in the silicon and copper to be determined for each sample thickness. These fits included

a 5% source correction to account for the positron annihilations in the  $2\mu\text{m}$  aluminum foil. Following measurements performed in [81], it was known that the foil used in this experiment contained lifetime components of 155ps and 256ps having relative intensities of 28% and 72%, respectively.

In order to visually analyze the results, a plot of positron fraction versus silicon thickness was created from our positron implantation model. Hence  $I_{1model}$  was solved using Eq. 3.21 for each thickness  $d$  used in this experiment. To account for the upper and lower limits of backscattering, these intensities were then used to determine the values of  $I_{1corrected}$  from Eq. 3.23 with the corresponding  $\beta$  values. By means of Eq. 3.22, with  $Z=29$  for copper, a value of  $\beta=0.354$  was calculated for the upper limit backscattering coefficient. The lower limit was taken as  $\beta=0$ . The measured annihilating fractions are plotted along with the upper and lower limits of  $I_{1corrected}$  (solid curves) as a function of silicon thickness in Fig. 3.8(a). For an acceptable fit, the experimental data would sit somewhere between the curve with minimum backscattering and the curve with

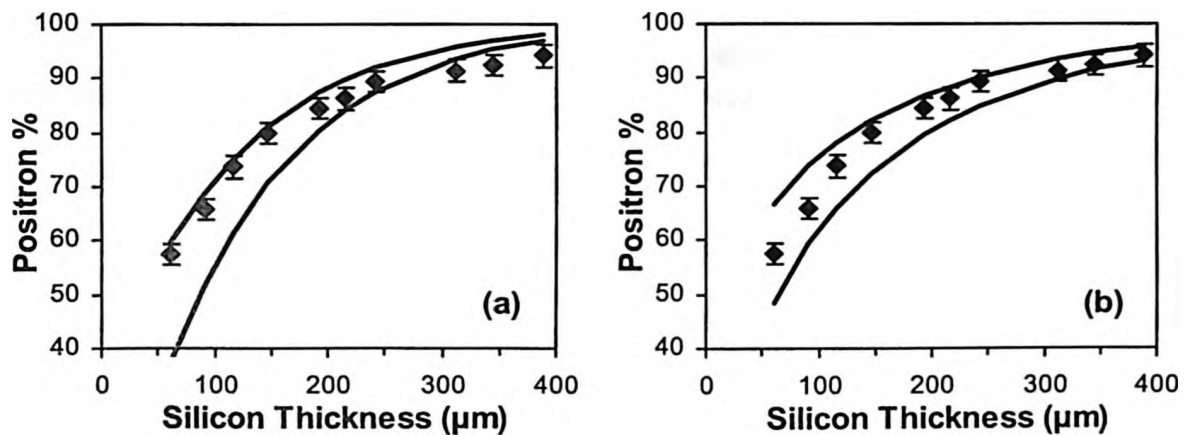


Figure 3.8: Measured fraction of positrons annihilating in various thicknesses of silicon used in the bi-layer sandwich configuration. The solid curves represent the upper and lower limits of the implantation model with (a)  $r=1.6$  and (b)  $r(T)=0.49+0.194\ln(T)$ .

maximum backscattering. This is true except for thicknesses above  $\sim 300\mu\text{m}$ , suggesting that the positron implantation model is not completely optimized. This can be explained by the possible "breakdown" of the Makhov profile for higher positron energies. As mentioned in the previous section, the Makhov distribution has only been verified for  $<50\text{keV}$  positrons whereas the  $^{22}\text{Na}$  emission spectrum extends to  $540\text{keV}$ . Hence, the Makhov profile was modified such that the model given by Eq. 3.20 would better represent the data measured in this experiment. The parameter  $r$ , which is fixed at  $r=1.6$  in the Makhov distribution, was shown to be energy dependent by Baker *et al.* [69], therefore was used for adjustment here. The energy dependence was assumed to follow the form given in Eq. 3.3. Repeating the integrations using this altered Makhov profile, led to the  $I_{\text{corrected}}$  curves shown in Fig. 3.8(b). The data are now observed to fall in the acceptable range for all silicon thicknesses. The two solid curves in this plot represent Eq. 3.3 with  $a=0.49$  and  $b=0.194$ , however there are multiple  $a$ - $b$  combinations that could be used to produce two curves completely enclosing the experimental data. Hence, the measurements obtained in this work support the argument that  $r$  is energy dependent and of the same form as given in Eq. 3.3. It is suggested that the Makhov profile (using  $r=1.6$ ) is sufficient for low energy positron implants but must be adjusted when modeling the implantation of positrons emitted over a broad energy spectrum.

Fig. 3.9(a) shows the implantation profile given by Eq. 3.20 with  $r(T)=0.49+0.194\ln(T)$ . Also plotted is an exponential distribution. The implantation of positrons from a continuous  $^{22}\text{Na}$  source has been modeled previously with an exponential profile, and an empirical relation for the positron absorption coefficient for a

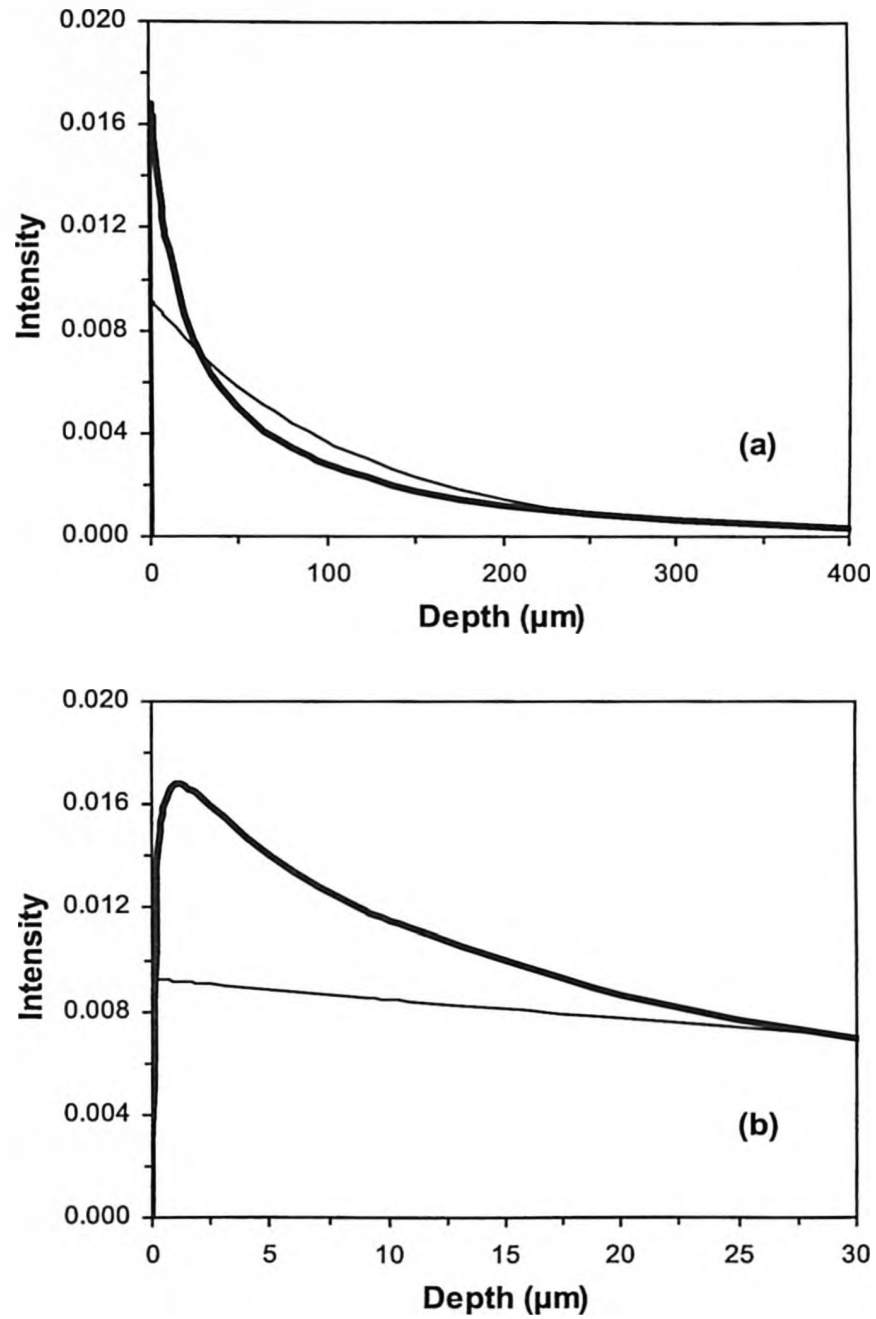


Figure 3.9: Implantation profile of positrons emitted from a  $^{22}\text{Na}$  source, modeled using Eq. 3.20 (thick curve) and an exponential (thin curve). Plot (a) shows the profiles to a depth of  $400\mu\text{m}$  while plot (b) is zoomed in to  $30\mu\text{m}$  to emphasize the differences in the shallow region of the silicon.

number of targets was derived in the literature [85]. The exponential shown here uses an absorption coefficient based on the atomic number and mass density of silicon. There are a few significant discrepancies between the two profiles. It was alluded to in [78] that the exponential model underestimates the amount of positrons absorbed in thin samples. The implantation profile suggested in the work here has a greater integrated area over small depths, possibly accounting for this underestimation. Fig. 3.9(b) compares the two profiles in the shallow region of the silicon sample. The most obvious distinction is the peak at  $2\mu\text{m}$  appearing in the newly suggested profile. Physically, this is expected since the positrons must travel some distance before thermalization, thus forming a peak beneath the surface of the sample. The fraction, or probability, at the silicon surface must therefore be zero (or very small if surface-state annihilations are considered). This is not the case in the exponential profile. Although it is less complex, another disadvantage of the exponential model is that it lacks fitting flexibility since there is only one parameter that can be used for adjustment.

### 3.2.5 Lifetime Measurements made on MeV Ion-Irradiated Silicon

Previously, PALS has been used to observe defects in bulk silicon  $>400\mu\text{m}$  in thickness. This section focuses on the development of a technique that allows the use of PALS to study defects in silicon introduced via ion implantation. The thickness of the defected layer characterized here is  $\sim 30\mu\text{m}$  (created by  $1.5\text{MeV H}^+$  irradiation) but it is suggested that the technique would be applicable for  $\sim 10\mu\text{m}$  layers, or even thinner for samples with larger mass densities. The key to accurate measurements is the newly

suggested implantation profile of positrons from a continuous  $^{22}\text{Na}$  source. This model can reliably predict the percentage of positrons probing the defected layer if the depth of the layer is known. A similar approach was demonstrated by Kauppinen and Corbel [25], however, using an exponential distribution of positrons.

TRIM simulations can be used to accurately predict the range (but not concentration) of vacancy-type defect formation in a material bombarded with an ion beam of known energy. With this range established, the intensity of positrons annihilating in the vicinity of the damage, hereafter referred to as  $I_{probed}$ , can be determined from the positron implantation model. The sandwich configuration can be employed using silicon samples thick enough to stop all positrons. This analysis is similar to the bi-layer situation since there are effectively two layers; the defected layer and the defect-free bulk. However, there will be three positron lifetime components; the defect lifetime  $\tau_d$ , the bulk silicon lifetime  $\tau_b$ , and the modified bulk lifetime  $\tau_{mb}$ . This, of course, is assuming one defect type. In this case, the positron fractions are determined by performing a three-component fit to the measured annihilation spectrum. The lifetime in the bulk silicon is fixed at 220ps with an intensity of  $1-I_{probed}$ , while the other two components are easily distinguished knowing that  $\tau_{mb} < 220\text{ps}$  and  $\tau_d > 220\text{ps}$ . With the measured modified bulk lifetime, one can use Eq. 3.10 to determine the defect trapping rate and hence the defect concentration. Alternatively, one may utilize the measured defect intensity component  $I_d$ . This intensity must be normalized (via division by  $I_{probed}$ ) before using in Eq. 3.13 to calculate the trapping rate. This normalization makes  $I_d$

equivalent to that obtained in a two-component bulk analysis. The defect concentration found using either of these methods should, in theory, give the same result.

The samples used in this case were the same 1.5MeV H<sup>+</sup> irradiated silicon samples used for the positron beam measurements in section 3.1.3. Thus, unique comparisons between the PALS results and the beam-based results could be made. The depth of the damaged silicon layer was simulated by TRIM to be 33±2μm, and the mean value of vacancies per ion per angstrom over the entire layer was determined to be ~0.00009. This factor is 3 times greater than that at 4.5μm, the mean depth probed by the 30keV positron beam. By solving the integral given by Eq. 3.21 with  $d=33\mu\text{m}$ , the positron implantation model predicts  $I_{probed}=37\%$ . This calculation used  $r(T)=0.49+0.194\ln(T)$  in the Makhov profile, conforming to the measured positron implantation profile of this work.

The lifetime measurements were made with the same <sup>22</sup>Na source, spectrometer, and software used for the (thinned silicon / copper) bi-layer experiment in section 3.2.4. With a sample thickness of ~388μm, double stacking was necessary to ensure complete positron absorption in the silicon. Since there was no change in mass density between the layers in this case, backscattering at the interfaces was neglected. The annihilation spectra were analyzed using a three-component fit as outlined above. Since measured values of either  $\tau_{mb}$  or  $I_d$  can be used to calculate the trapping rate, both calculations were performed iteratively in order to attain consistent results. The spectra were fit with several defect lifetime values until optimal agreement (within 8%) between the two trapping rate calculations was achieved. The mean value of  $\tau_d$  for all samples was

determined to be  $309 \pm 11$  ps. For  $H^+$  doses equivalent to the range used in this experiment, Kauppinen and Corbel [25] reported that the most dominant vacancy-type defect structure formed was the silicon divacancy with a lifetime of 300 ps, consistent with the results here. These measurements therefore strengthen the argument that divacancies are the dominant vacancy-type defect produced by moderate irradiation of silicon (i.e. doses well below the amorphization threshold). As mentioned in section 3.1.2, the trapping coefficient for the neutral silicon divacancy is commonly taken as  $1 \times 10^{15} s^{-1}$  and the atomic density of crystalline silicon is  $4.976 \times 10^{22} cm^{-3}$ . Using these values, the divacancy concentration was calculated using Eq. 3.14 and plotted versus ion dose on logarithmic scales in Fig. 3.10. In order to compare to the CBK model in this case, a dose adjustment factor of 0.00009 was used. Also plotted are the beam-based results. The PALS data can be fitted with an exponent of 0.64, which is consistent with the CBK value (0.63) as well as the beam-based measurements (0.66).

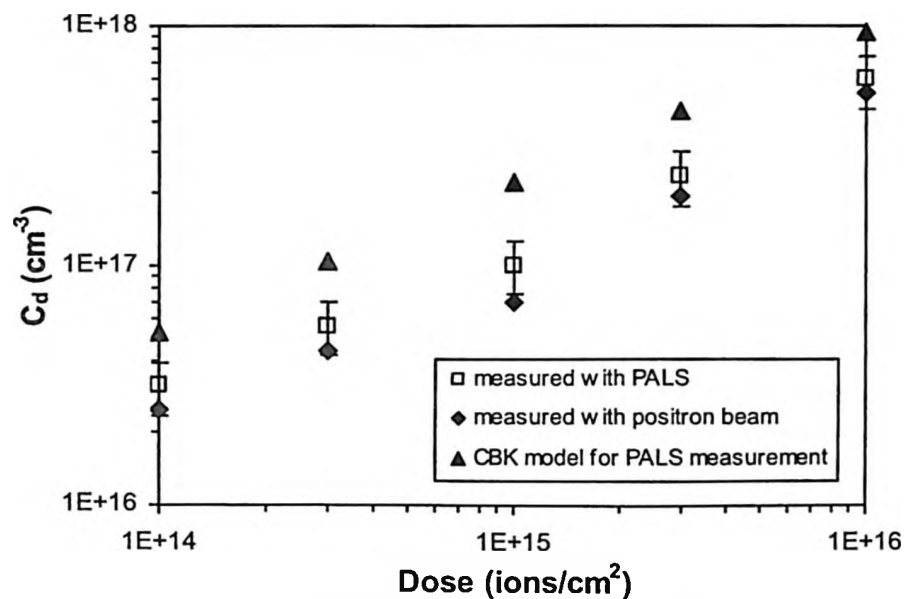


Figure 3.10: Concentration of divacancies in 1.5 MeV  $H^+$  irradiated silicon, measured using PALS and a positron beam and calculated using the CBK formula (modeled for PALS measurement).

Although the sublinear rate of defect accumulation with implantation dose is similar to the expected rate, the actual defect concentrations measured by the lifetime technique are significantly less than that predicted by the CBK model. This can be attributed to the likelihood that some of the divacancies in close proximity to the projected range become "masked" by nearby hydrogen, thereby decreasing the amount detected by the lifetime technique. This was the same phenomenon credited to the experimental discrepancy found by Kauppinen and Corbel [25]. Fig. 3.11 shows the TRIM simulation of the vacancy-type defect profile in silicon irradiated with 1.5MeV protons to a dose of  $3 \times 10^{15} \text{cm}^{-2}$ . Also shown is the implantation profile of the protons.

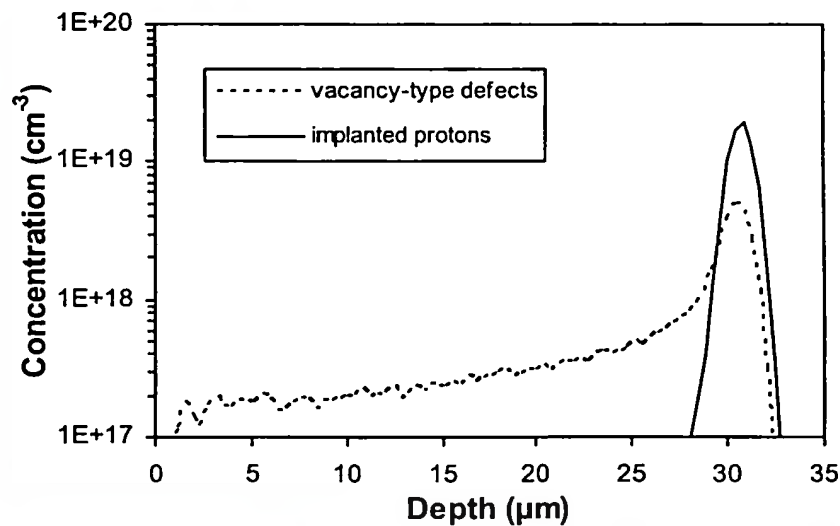


Figure 3.11: Vacancy distribution in silicon obtained from TRIM. The solid curve represents the implantation of 1.5MeV  $\text{H}^+$  ions. The dashed curve represents the formation of divacancies after recombination.

Since TRIM does not account for recombination, realistic room temperature vacancy concentrations cannot be simulated. It can be approximated that the number of vacancies surviving recombination at room temperature is on the order of 1% [86]. For illustrative

purposes, Fig. 3.11 assumes a recombination survival percentage of exactly 1%. This plot indicates a significantly greater concentration of vacancy-type defects near the projected range of the ion. Since the entire  $\sim 30\mu\text{m}$  defective layer was probed using the lifetime technique, it was expected that the mean concentration would be much greater than that measured by the beam and closer to that calculated using the CBK model. However, if all of the divacancies near the projected range were masked by hydrogen, then the mean concentration would be only slightly greater than the beam measurement. It is reasonable to assume that divacancy masking is not a factor when probing with a 30keV positron beam, since there are no  $\text{H}^+$  ions located in the shallow region around  $4.5\mu\text{m}$  as shown in Fig. 3.11. The reliable beam results thus serve as a lower limit to the range of acceptable results obtained by the lifetime measurements. It is problematic to deduce the number of undetected divacancies, but the PALS results shown in Fig. 3.10 are above the lower concentration limit and are therefore satisfactory. It is also difficult to deduce the mechanism of the divacancy masking, or passivation, phenomenon since there are a number of means by which the presence of  $\text{H}^+$  ions can alter the positron lifetime measurement. As stated by Fujinami *et al.* [87], there are a number of different hydrogen-vacancy complex structures ( $V_m\text{H}_n$  where  $m=1-2$  and  $n=1-4$  typically) that can form in silicon during post-implantation diffusion. Furthermore, Kauppinen and Corbel [25] suggested the possibility that hydrogen can be trapped at vacancy defects, preventing positron trapping and thereby masking the vacancy distribution from the positrons in the region near the proton stopping range.

It is possible to obtain limited information about the interactions between the  $H^+$  ions and the vacancies by exploring the thermal evolution of the lifetime (associated with the defect component) and the defect concentration. This was achieved by isochronal annealing of the silicon sample irradiated to a dose of  $3 \times 10^{15} \text{cm}^{-2}$ . The sample was heated in steps of  $50^\circ\text{C}$ , in the temperature range of 150 to  $600^\circ\text{C}$ , for 10min at each step. The annealing was performed in a box-furnace with the sample placed on a carbon plate, which was monitored using an exposed junction CHROMEGA-ALOMEGA<sup>®</sup> thermocouple. The uncertainty of the silicon temperature was determined to be  $\pm 10^\circ\text{C}$ . The annealing response was investigated with PALS using the same three-component analysis outlined above.

Fig. 3.12 presents the annealing response of the defect concentration (a) and the associated positron lifetime (b). As expected, the defect concentration generally decreases with annealing temperature. In these plots, there appear to be two annealing stages; a rapid decline in the range of  $150\text{-}250^\circ\text{C}$  and a more gradual decline in the range

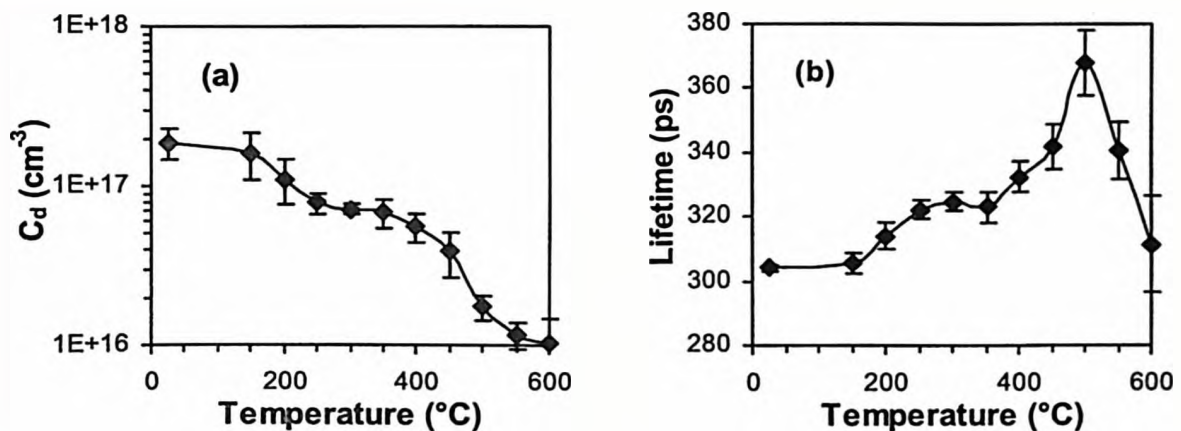


Figure 3.12: Annealing response of defect concentration (a) and positron lifetime (b) for silicon irradiated with  $1.5\text{MeV } H^+$  to a dose of  $3 \times 10^{15} \text{cm}^{-2}$ . The solid lines are visual guides.

of 350-500°C. These annealing stages are separated by a plateau, which is also apparent in the lifetime plot in the 250-350°C range. The defect concentration essentially vanishes at around 600°C. After annealing at 150°C, the measured lifetime of 305ps is still compatible with divacancies. The plateau has a lifetime of around 324ps, consistent with the value found for the hydrogen treated silicon samples tested by Uedono *et al.* [26]. This implies that the incorporation of H<sup>+</sup> ions leads to the evolution of a hydrogen-vacancy complex structure with greater open volume size than that of the divacancy. It is suggested that the initial rapid decrease in concentration represents the removal of divacancies, which are dominant in the region outside of the proton peak. This temperature range is consistent with the annealing temperature of divacancies in silicon as mentioned by Corbett *et al.* [10]. It is possible that in the region of the proton peak, a more stable complex becomes dominant. As proposed in the literature [88,89] hydrogen-vacancy complexes can form by hydrogen terminating the dangling silicon bonds of partially dissociated multivacancy defects, which are caused by the implantation. The plots in Fig. 3.12 suggest that the hydrogen-terminated defects observed here are stable and immobile up to a temperature of around 350°C, consistent with the work of Fujinami *et al.* [87]. After this, they start to become mobile and possibly form clusters during the second annealing stage. At 500°C, the bound hydrogen begin to release from the clusters and are almost completely released at 600°C, also as found by Fujinami *et al.* [87]. Since the measurements in this temperature range show that the lifetime rapidly decreases back to that of the divacancy, there is reason to believe that the release of bound hydrogen causes the defects to migrate apart from the clusters. This analysis is highly speculative

and a detailed study of the  $H^+$ /defect interactions is beyond the scope of this thesis. However, the results obtained here propose a topic for further exploration.

### 3.3 Fourier Transform Infrared Spectroscopy

Fourier Transform InfraRed (FTIR) spectroscopy is a commonly used technique to determine the composition of a material by observing its various infrared absorption (or transmission) peaks. It is one of the preferred techniques for applications that require fast, high signal-to-noise, non-destructive measurements. This section describes the basics of FTIR and how it is used to characterize defects in semiconductors. Measurements made on ion-irradiated silicon are discussed.

#### 3.3.1 Observation of Defects using FTIR

When a beam of infrared light is aimed onto a semiconducting material, some of its energy is transferred to the sample through a combination of mechanisms as discussed in section 2.1.3. This can be useful for detecting vibrational modes of the bonds present in the sample, which are strongly excited by long-wavelength photons in the mid infrared (5-40 $\mu$ m) and/or far infrared (40-350 $\mu$ m) parts of the spectrum. This excitation is the absorption mechanism described as a direct phonon transition. Infrared spectroscopy techniques are also used for observing absorption bands associated with defects in bulk material. As reported by Fan and Ramdas [12], defects can alter the vibrational modes of the lattice, resulting in shifts of the mid and/or far infrared absorption bands. These authors also showed that lattice defects, which act as carrier traps, can introduce bands in

the near infrared (0.7-5 $\mu$ m) and that these bands arise from electronic excitations to higher energies. Since this thesis is primarily interested in near infrared wavelengths, deep level trapping is the most significant absorption mechanism. By measuring the intensity of the transmitted light as a function of wavelength, the principal defects present in the sample are identified by the locations of the absorption peaks. The height, or intensity, of each peak is an indication of the defect concentration.

The basis of the FTIR measurement is an interferometer (typically a Michelson interferometer for near infrared wavelengths), which splits the source beam into two separate beams that travel different path lengths before being recombined and directed towards the sample [90]. The path length difference  $l$  is varied with an adjustable mirror. The recombined beam produces an interference pattern or an interferogram  $I(l)$ , which is a cosine function. The shape of the interferogram depends on the frequency of the light. In general, the function of the interferometer is to disperse the radiation provided by the IR source into its component frequencies. Therefore, with polychromatic light,  $I(l)$  is the sum of all the cosine functions. The sample, which absorbs certain frequencies by different amounts, changes the shape of the interferogram. By measuring  $I(l)$  for all possible  $l$  and computing its cosine Fourier Transform, this gives the transmission spectrum  $T(f)$ . The cosine Fourier Transform is given by:

$$T(f)S(f) = \int_{-\infty}^{\infty} [I(l) - I(0)/2] \cos(2\pi fl) dl \quad (3.24)$$

where  $S(f)$  is the known spectral intensity of the IR source and  $I(0)$  is the detected interferogram intensity at zero path length difference. Thus, the interferogram contains

the basic information on frequencies and intensities characteristic of the transmission spectrum but in a form that is not directly interpretable. This information is converted to a more familiar form, a spectrum, using Fourier Transform methods.

### 3.3.2 FTIR Measurements made on MeV Ion-Irradiated Silicon

As discussed in section 2.5.2, there exists a prominent near infrared absorption band located at  $1.8\mu\text{m}$ , which is associated with the silicon divacancy. As an example of this phenomenon, Fig. 3.13 shows the FTIR absorption spectrum for a double-side polished, high resistivity ( $>1000\Omega\text{cm}$ ), FZ  $\langle 100 \rangle$  silicon sample irradiated with 3MeV protons to a dose of  $2 \times 10^{16}\text{cm}^{-2}$  at 77K. Protons at this energy create defects in silicon to a depth of  $\sim 100\mu\text{m}$ . The measurements were made using a Work-IR spectrometer with an InAs detector having a sensitivity range in the near infrared of approximately  $1.3\mu\text{m} < \lambda < 2.6\mu\text{m}$ . The spectrum has arbitrary units normalized to give a value of zero at

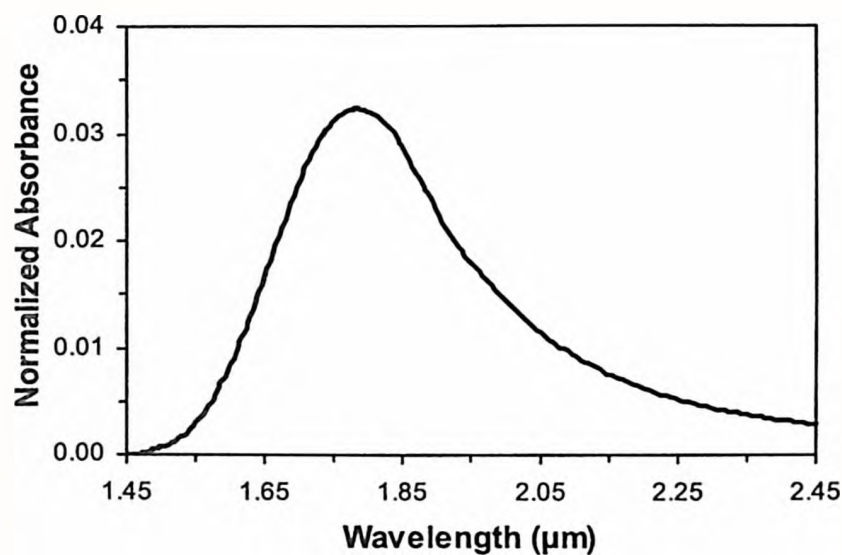


Figure 3.13: FTIR absorption spectrum for silicon irradiated with 3MeV protons to a dose of  $2 \times 10^{16}\text{cm}^{-2}$ .

a wavelength of  $1.45\mu\text{m}$ . The absorption peak centered at  $1.8\mu\text{m}$  is clearly observed in Fig. 3.13. The plotted response is consistent with that measured by Fan and Ramdas [12] for samples containing silicon divacancies. Hence, the absorption peak in Fig. 3.13 must be the result of deep levels associated with divacancies created by the  $3\text{MeV H}^+$  implantation. Fan and Ramdas [12] attributed the broad width of this peak to lattice vibrations and the Frank-Condon principle, which states that electronic transitions take place in times that are very short compared to the time required for the atomic nuclei to readjust their positions. Of significance to this thesis is the tail of the broad  $1.8\mu\text{m}$  band, which extends to shorter wavelengths towards the absorption edge. In particular, excess absorption is observed at the  $1.55\mu\text{m}$  telecom wavelength.

Similar FTIR measurements were made on a double-side polished, high resistivity ( $>1000\Omega\text{cm}$ ), FZ  $\langle 100 \rangle$  silicon sample irradiated with  $9.8\text{MeV Si}^+$  to a dose of  $7.9 \times 10^{13}\text{cm}^{-2}$  at room temperature. Using  $\text{Si}^+$  ions at this energy results in a defect

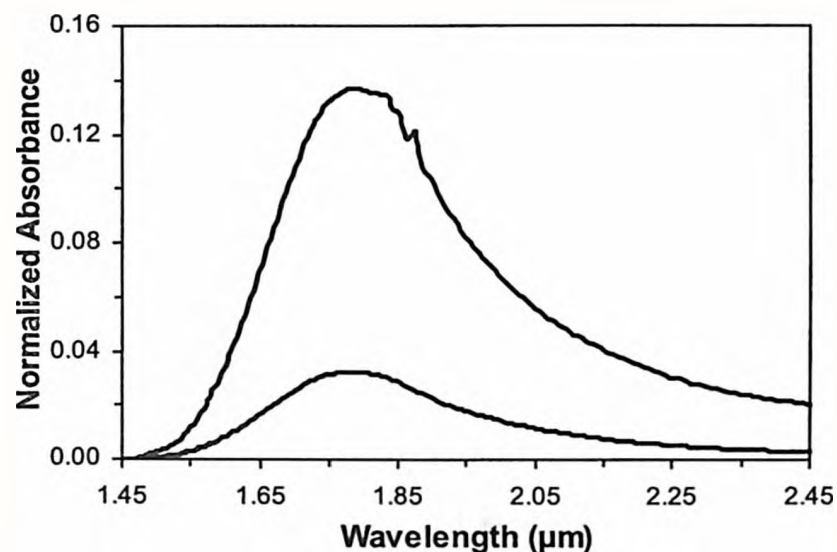


Figure 3.14: FTIR absorption spectra for silicon irradiated with  $9.8\text{MeV Si}^+$  to a dose of  $7.9 \times 10^{13}\text{cm}^{-2}$  (higher peak) and  $3\text{MeV H}^+$  to a dose of  $2 \times 10^{16}\text{cm}^{-2}$  (lower peak).

layer of  $\sim 5\mu\text{m}$  in thickness (5% of the thickness created by 3MeV protons). The absorption spectrum is shown in Fig. 3.14 along with that obtained from the  $\text{H}^+$  irradiated sample. The same  $1.8\mu\text{m}$  band is observed. Despite a lower dose by almost three orders of magnitude, the  $\text{Si}^+$  irradiation created considerably more divacancies than the  $\text{H}^+$  irradiation, as observed by the relative heights of the two peaks. From a processing standpoint, the use of  $\text{Si}^+$  is therefore a better choice of implantation species for creating small volumes of high optical absorption in this wavelength range. Also, with self-irradiation, passivation by hydrogen or any other implanted impurity is not an issue.

To explore the thermal response of the  $1.8\mu\text{m}$  band, isochronal annealing of the self-irradiated sample was performed. The sample was heated in steps of  $50^\circ\text{C}$ , in the temperature range of 150 to  $300^\circ\text{C}$ , for 10min at each step using the same setup described in section 3.2.5. An FTIR measurement was made following each annealing

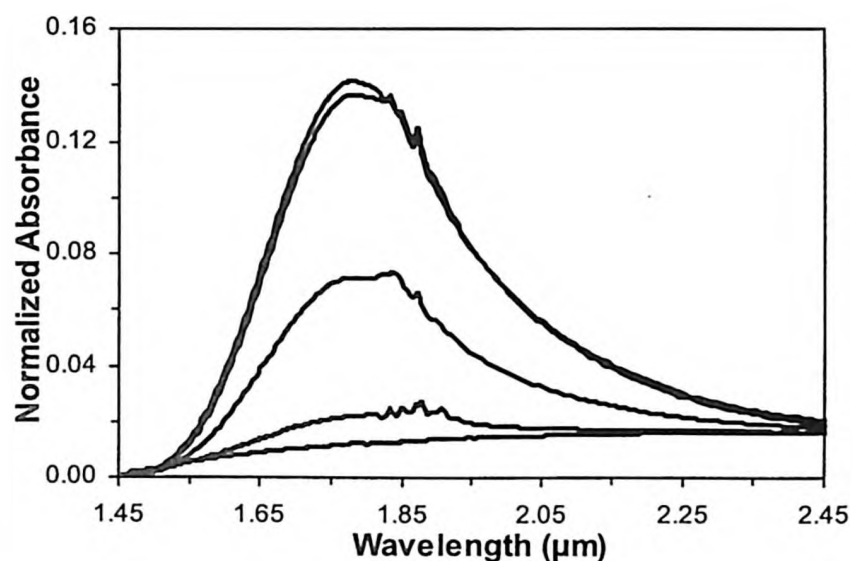


Figure 3.15: Annealing response of  $1.8\mu\text{m}$  absorption band for silicon sample irradiated with  $9.8\text{MeV Si}^+$  to a dose of  $7.9 \times 10^{13}\text{cm}^{-2}$ . The highest peak is measured at room temperature. The peak height decreases with increasing annealing temperatures of  $150^\circ\text{C}$ ,  $200^\circ\text{C}$ ,  $250^\circ\text{C}$ , and  $300^\circ\text{C}$ .

stage. These results are plotted in Fig. 3.15. As expected, the height of the peak decreases with temperature, signifying the removal of divacancies. The most significant decreases occur at 200 and 250°C, consistent with the divacancy annealing response found by Corbett *et al.* [10]. Hence, the infrared absorption measurements made here further strengthen the argument that divacancies are the dominant vacancy-type defect produced by moderate irradiation of silicon. As the height of the 1.8 $\mu\text{m}$  peak decreases, there is a corresponding reduction of the tail steepness, meaning that excess optical absorption at wavelengths around 1.55 $\mu\text{m}$  decreases as well. To represent the complete thermal response of the divacancies, Fig. 3.16 shows the total optical absorption found by integrating under the peak for each annealing temperature.

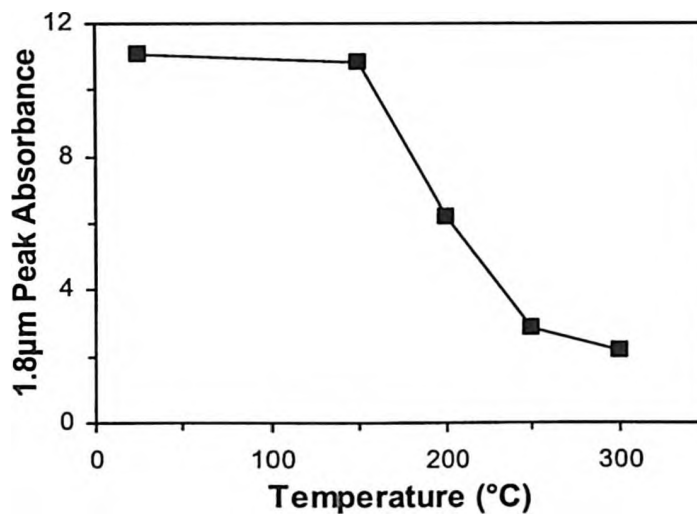


Figure 3.16: Total absorption determined by integrating under the 1.8 $\mu\text{m}$  divacancy peaks in Fig. 3.15.

## Chapter 4

# Defect-Engineered SOI Rib

## Waveguide Devices

### 4.1 Design and Fabrication

This section presents the techniques used to fabricate the waveguide devices used in this study. It discusses the processing of the SOI rib waveguides, the ion implantation methods used to create defects inside the waveguides, and the design considerations associated with the implantation mask. The preparation of the waveguide end facets, which play a vital role in waveguide loss measurements, is also discussed.

#### 4.1.1 Waveguide Processing

Low-loss optical waveguides in the rib geometry were fabricated using an SOI wafer that was prepared using the bonding and etch-back technique. This SOI consisted of a low-doped ( $<10^{15}\text{cm}^{-3}$ ),  $5\mu\text{m}$  thick,  $<100>$  overlayer on a  $1\mu\text{m}$  thick buried oxide. Three samples of approximately  $2\text{cm}^2$  were cleaved from the 6" wafer. These were cleaned by immersion in  $\text{H}_2\text{O}_2:\text{H}_2\text{SO}_4$ , followed by  $\text{H}_2\text{O}_2:\text{HCL}$ , and finally buffered HF. The samples were dried and baked at  $110^\circ\text{C}$  to remove moisture before a  $100\text{nm}$  oxide was deposited at  $300^\circ\text{C}$  using PECVD. A waveguide pattern consisting of fifteen individual ridges per sample was photolithographically defined and etched into the oxide

layer using buffered HF. Following removal of the photoresist, the waveguide pattern was transferred to the silicon via a KOH based wet etch, using the oxide as a hard etch mask. KOH predominantly etches the  $\langle 100 \rangle$  crystal plane in silicon and cannot permeate the  $\langle 111 \rangle$  plane [91]. This results in the characteristic sidewall slope of  $54.7^\circ$  relative to the surface. Following removal of the oxide layer, the rib heights were measured using a surface profilometer to range from  $1.2$  to  $1.3\mu\text{m}$ . With a nominal rib width of  $4\mu\text{m}$  at the base, this height measurement ensured that the waveguides were single mode, according to the model by Soref *et al.* [31]. Fig. 4.1 shows a contoured profile of the fundamental TE mode at a wavelength of  $1.55\mu\text{m}$ , simulated using

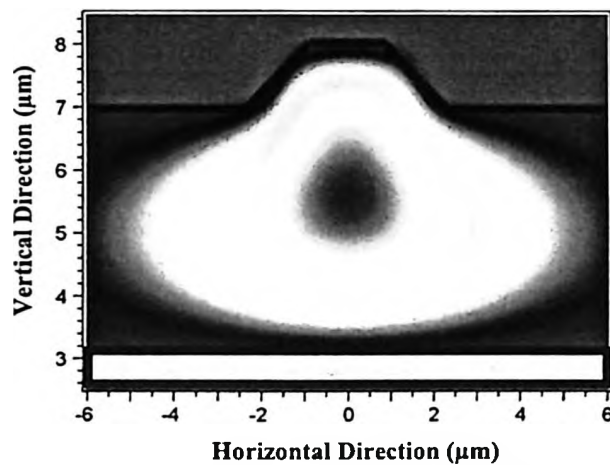


Figure 4.1: BPM simulation of the fundamental TE mode propagation in the fabricated waveguides used in this study.

commercial BeamProp software [28]. Although this simulation neglects the uncertainties in the actual waveguide dimensions, it is assumed to be a rigorous approximation of the optical mode shape. It can be estimated from the simulation that the optical power decays to around 5% of the maximum (which is located under the center of the rib) at a distance of  $6\mu\text{m}$  in the horizontal direction from the center of the rib.

#### 4.1.2 Incorporation of Defects into Waveguides

Following fabrication of the waveguide structure, photolithography was used to define an ion implantation mask with open regions coincident with the fifteen waveguides on each of the three samples. These windows varied in length from 10 to 2000 $\mu\text{m}$  and were 40 $\mu\text{m}$  in width centered on the waveguides. The use of photoresist as an implantation mask was convenient since it only requires a single deposition stage. A viscous photoresist (Shipley SE1827) specifically developed for use with ion implantation was employed, providing a masking thickness of  $\sim 5\mu\text{m}$ . Each sample was subsequently implanted at room temperature with 2.8MeV  $\text{Si}^+$  ions to a dose of  $4.0 \times 10^{12} \text{cm}^{-2}$ ,  $6.3 \times 10^{13} \text{cm}^{-2}$ , or  $2.5 \times 10^{14} \text{cm}^{-2}$ . The ion beam current and sample temperature were monitored carefully to ensure photoresist integrity during the implantation.

The maximum energy that can be used during selective ion implantation is limited by the thickness and density of the implant mask [38]. In this case,  $\sim 5\mu\text{m}$  of photoresist limited the  $\text{Si}^+$  implantation to 2.8MeV. The distribution of vacancy defects following 2.8MeV self-irradiation of silicon was simulated using TRIM code [39]. As shown in Fig. 2.10, the damage is created to a depth of  $\sim 2.6\mu\text{m}$  from the surface, whereas the silicon overlayer in which the waveguides are formed is  $5\mu\text{m}$  thick. This implies an incomplete overlap of the implantation damage with the optical mode of the undefected waveguide, as shown in Fig. 4.2. In order to achieve a complete overlap, it would be necessary to use higher energy ions and consequently a thicker photoresist mask. For the case of self-ion implantation into the waveguides described here, an energy of  $\sim 10\text{MeV}$  is

required to completely overlap the damage with the optical mode. This is at the high-end of production tool capability and exceeds the capabilities of many ion implanters. This also necessitates the use of a photoresist mask  $\sim 9\mu\text{m}$  in thickness.

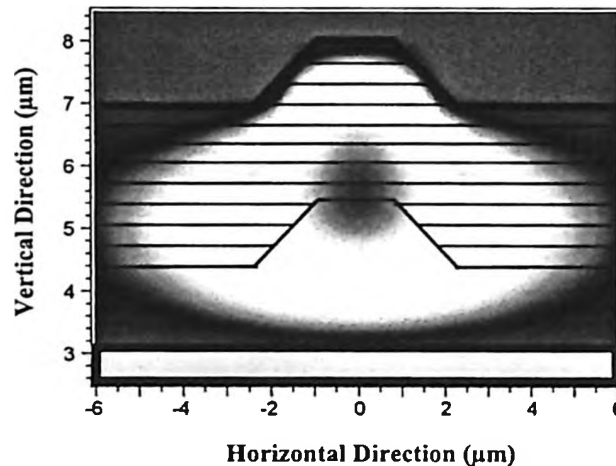


Figure 4.2: Overlap of damaged region (hatched area) with fundamental TE mode.

### 4.1.3 Process Considerations of Implantation Mask

In an analogous approach to high density packing of integrated devices in silicon microelectronics, there already exists a trend to smaller photonic structures. The necessities for high implantation energies and thick photoresist masks are eliminated as waveguide dimensions are reduced, and hence the optical mode moves closer to the device surface. For example, with a  $1\mu\text{m}$  thick silicon overlayer, the required implantation energy for a complete damage/mode overlap would be  $<0.6\text{MeV}$  and the required thickness of the photoresist mask would be  $<2\mu\text{m}$ . However, there are other limitations when using photoresist as an implantation mask. For instance, the sidewalls of developed photoresist tend to be curved and therefore a sharp demarcation to the

implantation is difficult to achieve [38]. Overdeveloping around the mask edges, which leads to excess implantation into the device, is another concern. In terms of optimization of mask thickness, there is a lack of reliable measurements and calculations of ion ranges and data on photoresist shrinkage under irradiation [92]. The irradiation of ions causes the photoresist to further polymerize and harden. If the ion dose is over  $\sim 10^{14} \text{cm}^{-2}$ , then the photoresist becomes difficult to remove from the silicon. It is possible to strip the photoresist off with a solvent such as  $\text{H}_2\text{SO}_4:\text{H}_2\text{O}_2$  however this will also strip off any metal deposited on the chip. An implantation dose of over  $\sim 10^{15} \text{cm}^{-2}$  will cause the photoresist mask to crack and ultimately fail. These dose constraints impose limits on the concentration of defects in the silicon that can be created with this method of masking.

Due to these photoresist issues, one must consider alternative implantation mask designs when fabricating small-scale silicon photonic devices that utilize implantation-induced defects. If attempting to develop VLSI-compatible defect-engineered IOCs and manufacturing in high volume, one must also consider at what stage in the fabrication sequence the defect introduction will be performed. Since silicon divacancies are completely removed at around  $300^\circ\text{C}$ , whereas most deposition and etching stages in VLSI fabrication require processing temperatures  $>300^\circ\text{C}$  [20], this designates the defect introduction of this study as a back-end technology, i.e. it must be performed in the last stage of the entire fabrication process.

The last stage in the fabrication of an integrated device is the deposition of a passivation layer, usually  $\text{Si}_3\text{N}_4$ , which provides electrical isolation and a barrier against water and sodium diffusion [20]. This insulator film is easily deposited using PECVD

methods, which provide good thickness uniformity and step coverage, and can be anisotropically etched in a plasma of  $\text{CF}_4/\text{H}_2$  leading to essentially vertical sidewalls. Also,  $\text{Si}_3\text{N}_4$  has a relatively high density and can be deposited below  $300^\circ\text{C}$ . Therefore, it may be beneficial to use the passivation layer as the implantation mask for creating IOCs that rely on divacancies. For ion implantation masking, this layer would be required to be thicker than that needed for passivation purposes. The open windows in the mask could be filled in with a thin  $\text{Si}_3\text{N}_4$  cap layer after the implantation.

Although  $\text{Si}_3\text{N}_4$  films provide excellent passivation, they have a large mechanical tensile stress [93]. This is normally accommodated by first depositing a thin layer of  $\text{SiO}_2$  before depositing the  $\text{Si}_3\text{N}_4$  layer. It is important to know what effects the irradiation of ions will have on the  $\text{Si}_3\text{N}_4$  mask, especially when it is left on the IOC as a passivation layer after the implantation. One of the most significant changes is, in fact, stress. It was demonstrated in the literature [94] how ion implantation, and its damage mechanisms, alters the stress in  $\text{Si}_3\text{N}_4$  films deposited onto silicon. The stress buildup is compressive as the measurements indicated a decrease in tensile stress with dose and then a change from tensile to compressive. At a certain threshold dose that depends on the mass of the ion, the compressive stress saturates. For higher atomic numbers, the compressive stress reaches saturation at lower doses, indicating that heavier ions produce more stress per ion. Since the stress in non-implanted  $\text{Si}_3\text{N}_4$  films is tensile, ion implantation can potentially result in a stress-compensated implantation mask that can remain on the chip without disrupting device functionality. This is illustrated in Fig. 4.3. By fabricating the  $\text{Si}_3\text{N}_4$  mask thicker than required to stop all ions, it will essentially

have two layers. The implanted layer will be compressive, as long as the dose is above the threshold, and the non-implanted layer will be tensile. If the thicknesses of these layers are chosen properly, based on the Stoney formula [95], the strain of the overall

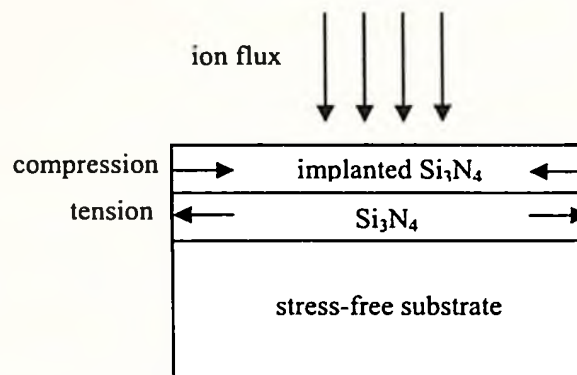


Figure 4.3: Configuration of stress-compensated ion implantation mask.

film will have a net value of zero. This means that the silicon (or SOI) substrate will also be strain-free and the IOC will operate as expected. The film will be stress-compensated as long as the implantation dose is above that required for compressive saturation. In principle, this technique would work for high doses and would therefore be suitable for creating devices that require high concentrations of implantation-induced defects.

#### 4.1.4 Facet Preparation

Optical quality waveguide end facets were prepared using a Loadpoint Microace dicing saw along with a fine grit Disco diamond blade. The procedure developed in this work does not require subsequent polishing or post-dicing facet preparation of any kind and has been found to result in facets of quality comparable with those produced via cleaving or dicing and polishing. The dicing procedure consisted of a shallow cut

approximately  $40\mu\text{m}$  from the top surface of the sample using a slow feed rate (1mm/s) and fast spindle rate (40krpm) and then stepping approximately  $20\mu\text{m}$  (i.e. less than the width of the shallow cut) away from the facet to cut through the entire substrate. It was discovered that any sort of blade wobbling or vibration caused “chipping” which negatively influenced the facet quality. This chipping was diminished after re-mounting the blade, ensuring proper tightness, and using a lower pressure in the water coolant stream. This process was able to produce facets with consistent coupling loss across the fifteen waveguides, permitting the subsequent measurement of loss associated with injected defects as described in section 4.2.1. Using a low loss, tapered optical fiber to butt couple light into and out of the rib waveguides, a total coupling loss of  $13\pm 2\text{dB}$  was determined for each of the three samples. This was more consistent than the total coupling loss of facets made by a cleaving method, which was typically around  $18\pm 8\text{dB}$ . Fig. 4.4 shows a Scanning Electron Microscope (SEM) image of an end facet made using the dicing procedure described above. Striations due to the blade are observed but are on a scale that is insignificant compared to the wavelength of the coupled light.

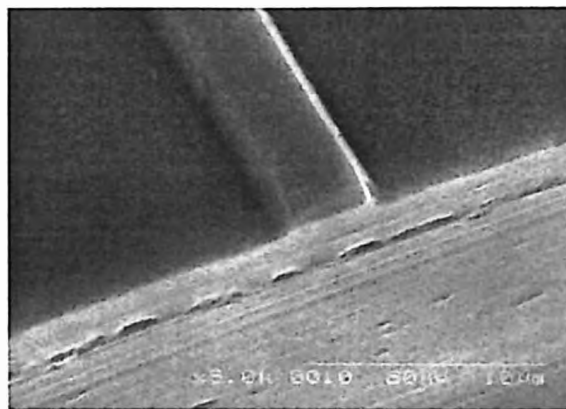


Figure 4.4: SEM image of a typical waveguide end facet made by a careful dicing procedure.

## 4.2 Static Attenuators

This section discusses the optical loss measurements made on the defected rib waveguides. Since each waveguide has a different defected length, according to the fifteen photoresist windows, the optical loss per unit length ( $\text{dBcm}^{-1}$ ) can be determined accurately. The response of this attenuation to isochronal annealing is also investigated. Finally, the loss mechanisms are analyzed so that predictions of static attenuation due to vacancy-type defects can be achieved during device design.

### 4.2.1 Measurement of Optical Loss

Using a Thor Labs broadband source with a wavelength range of 1.53 to  $1.61\mu\text{m}$ , optical loss measurements were performed for the fifteen waveguides on each of the three implanted samples. The setup used to make these measurements is shown in Fig. 4.5.

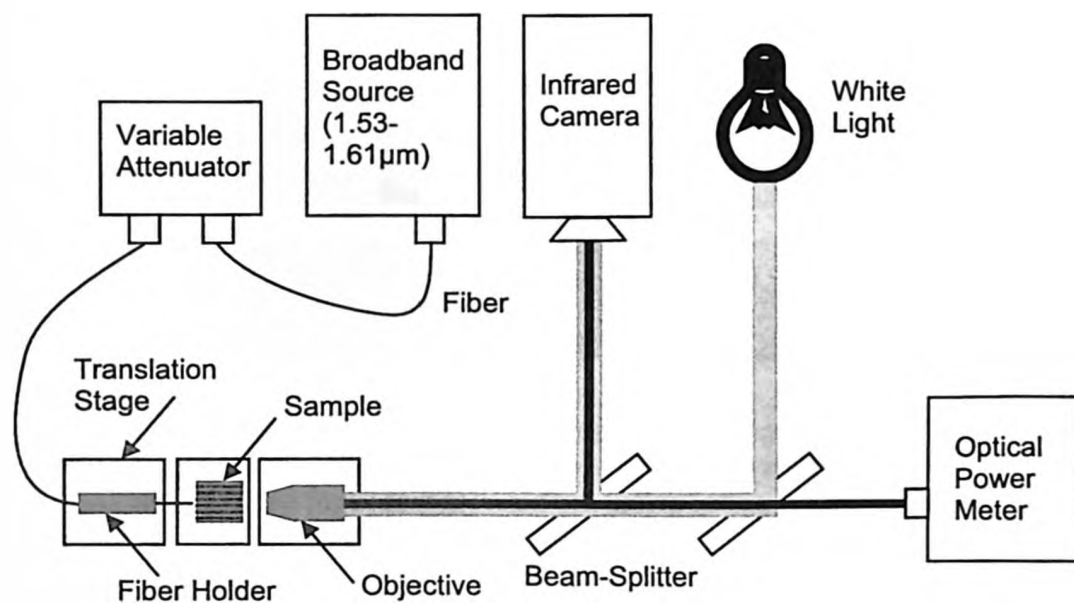


Figure 4.5: Setup used to make waveguide loss measurements.

The output power from the source (determined previously to be 11.5dBm) was butt coupled into the rib waveguides using low-loss, tapered optical fiber, which first passed through a variable attenuator to achieve 0dBm at the end of the fiber as a reference. The fiber was aligned with each waveguide using a Newport ULTRAlign manual translation stage. The output signal was collected with a 10x objective lens, and successful waveguiding was confirmed by imaging the waveguide output mode with an ElectroPhysics MicronViewer infrared camera. The objective lens was first aligned to the output end of the rib waveguide by directing a beam of white light through the opposite end of the objective and viewing the reflected waveguide image on the camera. The fiber position was adjusted using the translation stage until the peak transmitted signal power was determined using an ILX Lightwave free-space optical power meter. Once the peak power was found, the output objective was replaced with another fiber in order to determine the total fiber-to-fiber loss. Fig. 4.6 shows images obtained from the

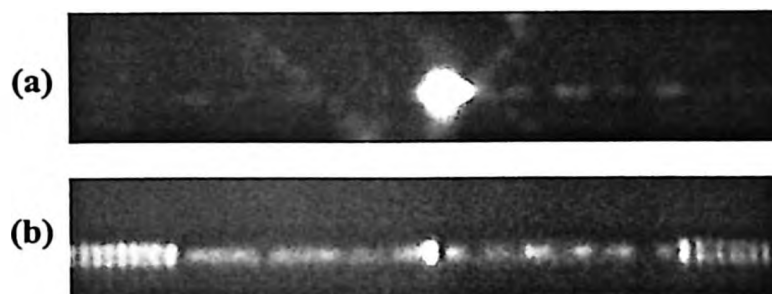


Figure 4.6: Infrared camera images of the output mode from a waveguide with no defects (a) and the output mode from a defected waveguide (b).

infrared camera, illustrating the differences between (a) attenuation in a waveguide without deliberately introduced defects and (b) that having received a 2.8MeV  $\text{Si}^+$

implantation dose of  $6.3 \times 10^{13} \text{cm}^{-2}$  over 10% of its length. In the defected waveguide, much of the fundamental mode power is absorbed and directed away from the waveguide through scattering and/or radiation.

All of the implanted waveguides suffered from optical loss in excess of the value for low-doped silicon of  $<0.1 \text{dBcm}^{-1}$  [3]. This loss was dependent on the processing conditions (the same for each waveguide on a particular sample) and the length of the thick photoresist window (used to define the defected region in the waveguide) through which the  $\text{Si}^+$  implantation was made. The total measured loss of the optical mode may be summarized by the relationship:

$$\text{Loss} = (\alpha_a + \alpha_s + \alpha_r)W + \alpha_i L + c \quad (4.1)$$

where  $\alpha_a$  is the absorption loss per length due to the absorption cross-section of the injected vacancy-type defects,  $\alpha_s$  and  $\alpha_r$  are the scattering and radiation losses per length, respectively, resulting from the defected volume,  $W$  is the length of the photoresist window,  $\alpha_i$  is the intrinsic loss per length of the low doped silicon,  $L$  is the total length of the waveguide and  $c$  is a constant related to the total coupling loss [23]. It should be noted that any optical signal scattered or radiated out of the waveguide due to the defected volume was not collected by the output fiber, and was therefore included in the measured loss. Hence, the total modal attenuation resulting from the defects can be written as  $\alpha_d$  where  $\alpha_d = \alpha_a + \alpha_s + \alpha_r$ . In the present case, it is possible to ignore the term  $\alpha_i L$  in Eq. 4.1 such that the determination of  $\alpha_d$  is via a straightforward measurement of the slope of a plot of loss versus implantation window length. The intercept is the total coupling loss of the measurement. In this way,  $\alpha_d$  for each of the three samples was

determined. Fig. 4.7 shows the results of the modal loss versus the length of the photoresist window for these samples. The measured loss in dB exhibits a linear behavior with the implant window length as expected from Eq. 4.1. The values of  $\alpha_d$  were determined from the fitted slopes to be  $150 \pm 5 \text{ dBcm}^{-1}$  for a  $2.8 \text{ MeV Si}^+$  implantation dose of  $4.0 \times 10^{12} \text{ cm}^{-2}$ ;  $430 \pm 15 \text{ dBcm}^{-1}$  for  $6.3 \times 10^{13} \text{ cm}^{-2}$ ; and  $1090 \pm 25 \text{ dBcm}^{-1}$  for

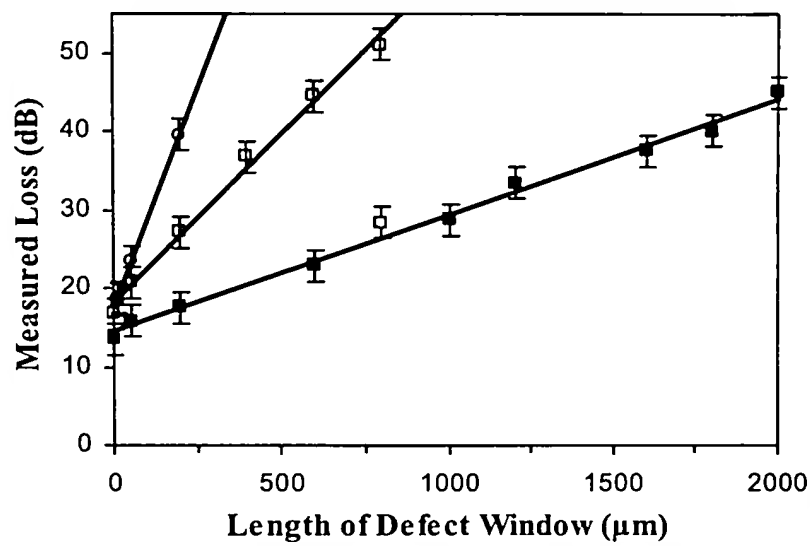


Figure 4.7: Measured loss in  $\text{Si}^+$  implanted waveguides versus length of implant window. Closed squares dose= $4 \times 10^{12} \text{ cm}^{-2}$ ; open squares dose= $6.3 \times 10^{13} \text{ cm}^{-2}$ ; open circles dose= $2.5 \times 10^{14} \text{ cm}^{-2}$ .

$2.5 \times 10^{14} \text{ cm}^{-2}$ . In the case of doses  $6.3 \times 10^{13} \text{ cm}^{-2}$  and  $2.5 \times 10^{14} \text{ cm}^{-2}$ , the loss could not be measured for window lengths  $>800 \mu\text{m}$  and  $>200 \mu\text{m}$ , respectively, since the output mode was too faint to be observed on the infrared camera. The values of  $c$  obtained from the linear fits range from 15 to 18 dB, greater than the average coupling loss measured before the samples underwent the  $\text{Si}^+$  implantation. It is suggested that this increase may be due to an additional coupling term associated with the mode mismatch at the interfaces

between the defected and undefected waveguide at the beginning and end of the implant window, an effect acknowledged by de Dood and Polman [18].

#### 4.2.2 Response of Attenuation to Thermal Annealing

The sample irradiated to a dose of  $6.3 \times 10^{13} \text{cm}^{-2}$  was used to explore the optical loss response to isochronal annealing. This sample was sequentially annealed for 10 minutes in steps of  $50^\circ\text{C}$  using a box-furnace in the temperature range 150 to  $300^\circ\text{C}$ . Measurements of optical loss were taken after each annealing stage in a manner identical to that described in section 4.2.1. The annealing results of optical loss versus implant window length are shown in Fig. 4.8. For all temperatures, the modal loss remains linear with length of defect window signifying a uniform change in the defect concentration and/or defect structure with a concomitant reduction in optical loss.

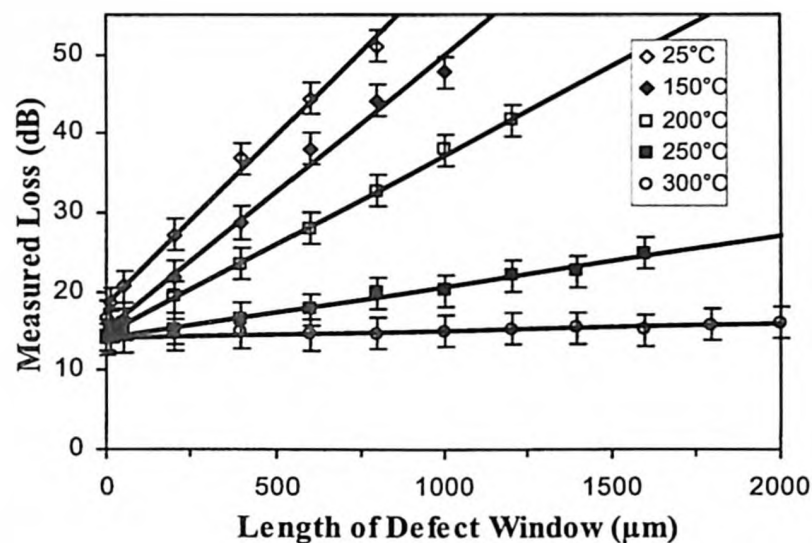


Figure 4.8: Annealing results for the sample self-irradiated to a dose of  $6.3 \times 10^{13} \text{cm}^{-2}$ .

The values of modal attenuation  $\alpha_d$  versus annealing temperature are shown in Fig. 4.9. A significant reduction in  $\alpha_d$  is observed for temperatures between 150°C and 250°C, with complete recovery of the low-loss characteristics of the SOI rib waveguide after annealing at 300°C. This response to annealing temperature is consistent with the

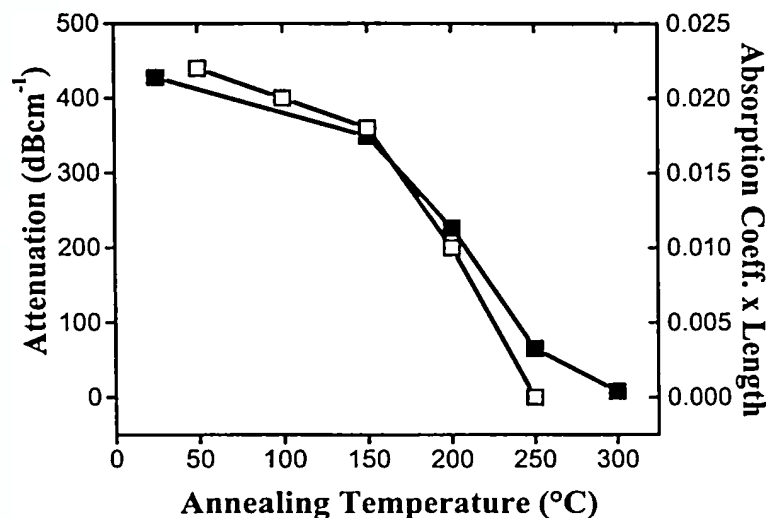


Figure 4.9: Modal attenuation versus temperature (closed squares), found by the slope of each linear fit in Fig. 4.8. Also shown are the results from Stein *et al.* [55] (open squares).

annealing characteristics of the silicon divacancy determined previously by Stein *et al.* [55] who used the 1.8 $\mu$ m band to measure the product of absorption coefficient and length of defected layer for oxygen-irradiated bulk silicon. These results, which are also shown in Fig. 4.9 for comparison, confirm that the increase in modal loss observed in the self-irradiated SOI rib waveguides is due to the introduction of silicon divacancies. The thermal stability of a static attenuator or any device utilizing this implantation process may therefore be deduced from the activation energy for divacancy annealing, which was

reported by Cheng and Lori [96] to be 1.25eV. The results here are in contrast to the thermal response of optical loss measured by de Dood and Polman [18] for ion implantation resulting in the creation of completely amorphous waveguiding layers in SOI. They found that a subsequent 500°C anneal for 3 hours caused a negligible effect on the loss characteristics of their waveguides. This indicates that a dose of  $6.3 \times 10^{13} \text{cm}^{-2}$  using 2.8MeV Si<sup>+</sup> is below the silicon amorphization threshold.

### 4.2.3 Analysis of Modal Loss Mechanisms Due to Defects

It was discussed in section 2.3 that loss in semiconductor waveguides can arise from absorption, scattering, and radiation. It is of some interest to dissect  $\alpha_d$  into its components and attempt to quantify the losses due to absorption  $\alpha_a$ , scattering  $\alpha_s$ , and radiation  $\alpha_r$ . Optical scattering due to defects is difficult to calculate, whereas the predictions of absorption and radiation loss are somewhat easier.

Absorption of infrared wavelengths in ion-irradiated silicon (bulk as opposed to waveguide structures) has been observed previously. In particular, Cheng *et al.* [24] identified the broad absorption band at 1.8 $\mu\text{m}$ , with associated absorption extending to the band-edge, to be a consequence of divacancies. In addition to this, Cheng and Lori [96] derived a value of divacancy concentration per unit absorption coefficient of  $7.7 \times 10^{16} \text{cm}^{-2}$  for the peak absorption around 1.8 $\mu\text{m}$ . In principle, this should permit a prediction of absorption if the concentration of divacancies is known. However, the measurement of divacancy concentration following ion implantation is generally not straightforward. Experimental results in sections 3.1.3 and 3.2.5 demonstrated the

satisfactory agreement between divacancy concentrations measured directly using PAS methods and those calculated using the CBK model for vacancy-type defect concentrations [59]. This model can therefore be used to predict the value of optical absorption for a given adjusted implantation dose using the equation:

$$\alpha_a = 4.35 \times \frac{(2.79 \times 10^{10}) \phi_d^{0.63}}{7.7 \times 10^{16}} \quad (4.2)$$

where the factor 4.35 converts the units from  $\text{cm}^{-1}$  to  $\text{dBcm}^{-1}$ . The numerator is the divacancy concentration as derived from the CBK model and the denominator is the value obtained from Cheng and Lori [96]. Fig. 4.10 shows a plot of  $\alpha_a$  as a function of implantation dose determined using Eq. 4.2 with a dose adjustment factor of 0.2

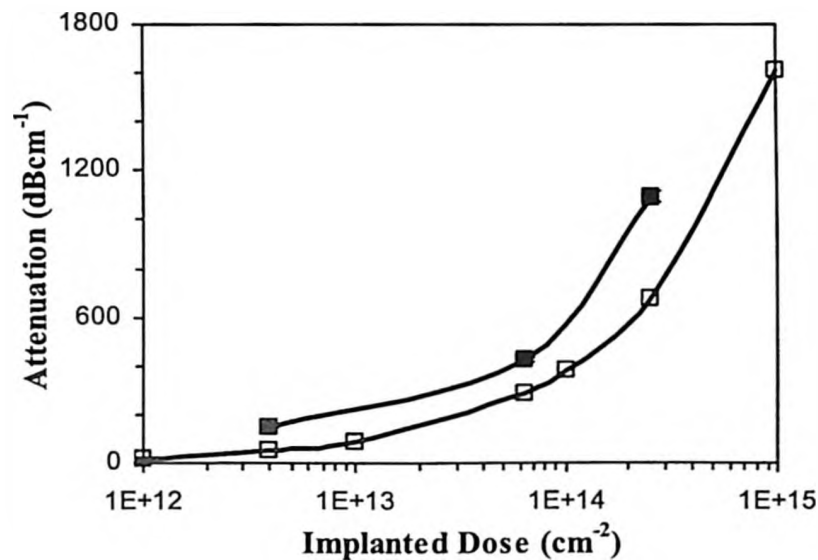


Figure 4.10: Optical absorption  $\alpha_a$ , derived from Eq. 4.2, versus implantation dose for 2.8MeV  $\text{Si}^+$  ions (open squares) and total attenuation  $\alpha_d$  measured in the irradiated SOI rib waveguides (closed squares). The solid lines are visual guides.

(determined previously for 2.8MeV  $\text{Si}^+$ ). Also shown are the measured  $\alpha_d$  values for the 2.8MeV  $\text{Si}^+$  implanted SOI rib waveguides. The calculated values of  $\alpha_a$  are

systematically less than the measured total attenuation values. This discrepancy is likely due to the additional  $\alpha_s$  and  $\alpha_r$  components obtained in the measurements as well as the incomplete overlap of the implantation damage with the optical mode. Other minor discrepancies result from the measurement wavelength range (1.53 to 1.61 $\mu\text{m}$ ), the application of the CBK model to end-of-range as opposed to half-range defects (although this gives a good approximation of mean concentration), and the additional losses via defects that are not divacancies.

Modeling the loss associated with scattering or radiation from the defected waveguides is complex, however, it is related to the changes in the real part of the refractive index accompanied by the ion implantation. Baranova *et al.* [11] demonstrated that the index of crystalline silicon increases with ion dose and then saturates upon amorphization. Microscopically, index perturbations caused by local defects can result in Rayleigh scattering of light. However, the size of a divacancy is much smaller than the wavelength of propagation ( $\sim 1.55\mu\text{m}$ ) therefore Rayleigh scattering, in this case, is considered negligible. Macroscopically, average index changes in waveguide structures can lead to the introduction of leaky modes and therefore radiation loss. Hence, for the self-irradiated SOI rib waveguides in this study, it was assumed that  $\alpha_r \gg \alpha_s$  and therefore  $\alpha_f \approx \alpha_a + \alpha_r$ . Since the irradiated layer did not completely overlap the fundamental mode, as shown in Fig. 4.2, the index profile of the waveguide over the implanted lengths was altered and radiation modes were introduced, as in the literature [35].

The average increase in refractive index  $\Delta n_R$  for a 2.8MeV  $\text{Si}^+$  dose of  $6.3 \times 10^{13} \text{cm}^{-2}$  was derived from experimental values measured by Baranova *et al.* [11],

who used 80keV Ar<sup>+</sup> implantation in bulk silicon. By determining the dose adjustment factor from the TRIM simulation of vacancy-type defect concentration for 80keV Ar<sup>+</sup> irradiation, the equivalent implantation dose was calculated using the CBK model. The mean vacancies per ion per angstrom factor was 0.6, giving an equivalent dose of  $2.1 \times 10^{13} \text{cm}^{-2}$  (i.e. the mean concentration of defects is equivalent to that created by a dose of  $6.3 \times 10^{13} \text{cm}^{-2}$  using 2.8MeV Si<sup>+</sup>). According to the work of Baranova *et al.* [11], the irradiation of silicon to a dose of  $2.1 \times 10^{13} \text{cm}^{-2}$  with 80keV Ar<sup>+</sup> causes the index to increase by  $\Delta n_R \approx 0.01$ .

The influence of implantation-induced index modification on mode propagation in SOI rib waveguides was simulated using BeamProp. This simulation used waveguide dimensions representative of this study. The depth of the irradiated layer was fixed at 2.6 $\mu\text{m}$  below the silicon surface (corresponding to the end-of-range of 2.8MeV Si<sup>+</sup>) and the width was 40 $\mu\text{m}$  (corresponding to the width of the photoresist windows) centered about the waveguide rib. Using a value of  $\Delta n_R \approx 0.01$ , Fig. 4.11 shows the mode evolution after propagating various distances through the index-modified region of the waveguide. It is observed that the light spreads out in the plane of the silicon overlayer, exciting other modes and forming a beat pattern due the interference of multiple modes. This light dispersion is initiated by the irregular shape of the defected cross-section, illustrated in Fig. 4.2, and is therefore a result of performing the implantation after the fabrication of the rib. The coupling of light back into the fundamental mode (of the undefected waveguide) depends on the mode overlap integral and is hence a function of the mode beat period and the length of the defected region. The simulated mode shapes are similar

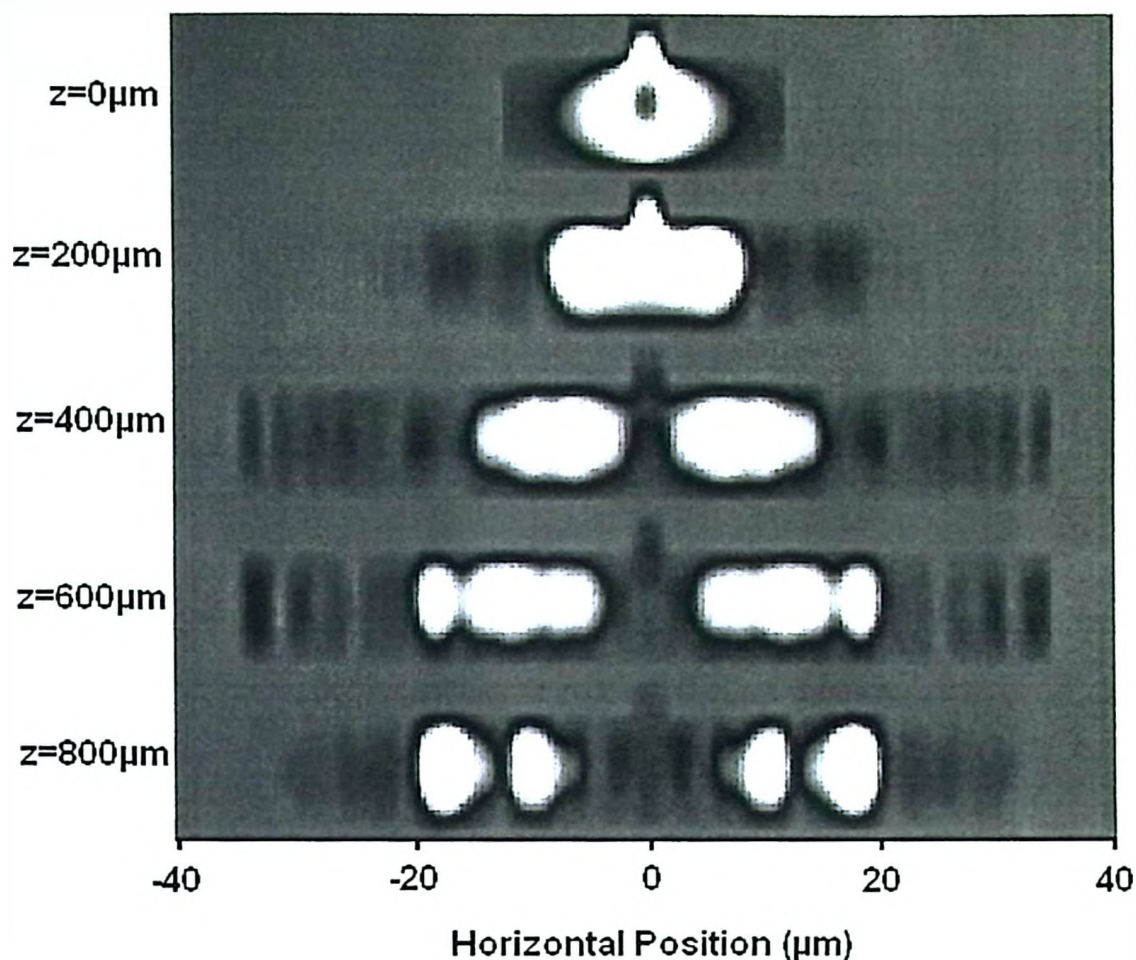


Figure 4.11: BeamProp simulation of mode evolution due to the increase in the real part of the index of the defected layer in the SOI rib waveguide.

to those observed at the waveguide output using the infrared camera, shown by the image in Fig. 4.6(b). The leaky modes most likely remained excited while propagating through the undefected waveguide towards the output. The power contained in these modes contributes to the  $\alpha_r$  term. By monitoring the optical power within  $10\mu\text{m}$  of the center of the waveguide rib (i.e. within the region that contains the entire mode of the undefected waveguide),  $\alpha_r$  was simulated to be  $185\text{dBcm}^{-1}$  as given by the fitted slope in Fig. 4.12.

Using Eq. 4.2 at a dose of  $6.3 \times 10^{13} \text{ cm}^{-2}$ ,  $\alpha_a$  was calculated to be  $282 \text{ dBcm}^{-1}$ . The total attenuation is therefore predicted to be  $\alpha_d \approx \alpha_a + \alpha_r = 467 \text{ dBcm}^{-1}$ . Although this is close to the measured value of  $430 \pm 15 \text{ dBcm}^{-1}$ , the overestimation is likely due to the incomplete

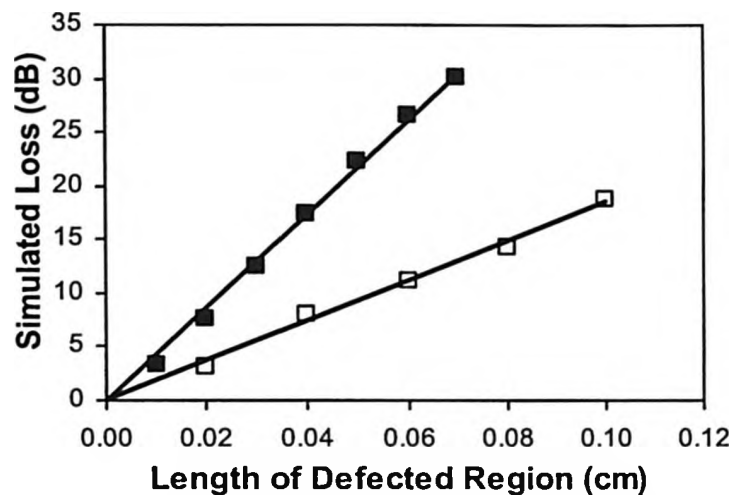


Figure 4.12: BeamProp simulation of radiation loss (open squares) and total loss (closed squares) versus length of defected region using an implantation dose of  $6.3 \times 10^{13} \text{ cm}^{-2}$ .

overlap of the implantation damage with the optical mode. Despite the fact that the mode changes shape throughout the defected region, a fraction of the optical power always propagates below the irradiated part of the waveguide and is not absorbed. Another simulation of optical power loss was performed, this time with the addition of a term representing the change in the imaginary part of the index  $\Delta n_i$ . Using Eq. 2.25 with  $\alpha_a = 282 \text{ dBcm}^{-1} = 65 \text{ cm}^{-1}$  and  $\lambda_0 = 1.55 \mu\text{m}$ , this was calculated to be  $\Delta n_i \approx 0.0008$ . The results of this simulation are also plotted in Fig. 4.12 and a total attenuation of  $434 \text{ dBcm}^{-1}$  was determined from the fitted slope. This is within 2% of the measured value of  $\alpha_d$ , owing to the reliability of this analysis.

It is concluded from this analysis that when designing a static attenuator or a similar device that makes use of this process, the optimal technique would be to irradiate the full depth of the silicon overlayer and attempt to create a uniform concentration of defects. This can be achieved by utilizing multiple implantation energies and/or smaller waveguide dimensions. In this fashion, the implantation-induced index change would result in negligible radiation loss. Thus, the loss would be purely due to absorption, minimizing radiation and subsequent coupling of light into other devices on the chip.

### **4.3 Other Devices for Future Work**

This section demonstrates the concepts of other devices that could potentially use defects caused by the irradiation of ions. Predictions of absorption coefficients based on measurements in bulk silicon are used to compare integrated optical barriers that utilize defect-engineering with those that rely on the free carrier effect. Also discussed is how a volume of defects between two closely spaced SOI rib waveguides could reduce crosstalk or, with different defect volume dimensions, instigate enhanced coupling.

#### **4.3.1 Integrated Optical Barriers**

As a result of the high optical absorption at  $1.55\mu\text{m}$ , implantation-induced damage can be used as an optical barrier between telecommunication devices integrated on the same substrate. This can help minimize optical noise (undesired interference signals) introduced by the leakage of optical power from one device to another. In order to maximize the optical absorption in SOI structures, ion implantation energies that

produce damage down to the buried oxide must be used. Using Eq. 4.2, it is possible to estimate the implantation dose required to create an integrated optical barrier of any given width, capable of producing the desired reduction of optical power. For example, using a  $5\mu\text{m}$  thick silicon overlayer, a 10dB barrier with a width of  $1000\mu\text{m}$  would require a 9.5MeV self-implantation dose of  $2.3 \times 10^{13} \text{cm}^{-2}$ . Using a  $5\mu\text{m}$  overlayer, irradiating down to the buried oxide with  $\text{Si}^+$  ions requires an energy approaching the production tool limit, hindering the feasibility of the optical barrier. Lighter ions can be used at the expense of greater implantation doses and the possibility of defect passivation. For instance,  $\text{He}^+$  ions would only require an energy of 1.3MeV. The trade-off is that, assuming negligible passivation of defects, a dose of  $6.1 \times 10^{14} \text{cm}^{-2}$  would be needed to produce a 10dB barrier with a width of  $1000\mu\text{m}$ . Nevertheless, as waveguide and other optical device dimensions are reduced to thicknesses approaching  $1\mu\text{m}$ , defect-engineered optical barriers become a very attractive method.

The alternative to damage mediated on-chip absorption is the creation of regions with high carrier concentration fabricated via the implantation of, for example, phosphorus [2]. The free carrier component of the absorption coefficient in semiconductors is given by the Drude-Lorenz model (Eq. 2.27). This model was compared with experimental results in [21] and it was found that, for a wavelength of  $1.55\mu\text{m}$ , the absorption coefficients predicted by the model are  $\sim 0.5$  of the measured values for p-type silicon, and  $\sim 0.25$  of the measured values for n-type silicon. Using these results, it can be shown that for implantation of phosphorus, i.e. n-type silicon, a free carrier (electron) concentration of  $2.7 \times 10^{18} \text{cm}^{-3}$  is needed to create a 10dB barrier

with a width of  $1000\mu\text{m}$ . Using an overlayer thickness of  $5\mu\text{m}$ , this would require an implantation dose of  $1.4 \times 10^{15} \text{cm}^{-2}$ , two orders of magnitude greater than that required for the defect-engineered barrier using  $\text{Si}^+$  irradiation. Another disadvantage of the free carrier effect is that high temperature annealing is required to activate the carriers.

### 4.3.2 Barriers Between Waveguides

A particular device that may utilize integrated optical barriers is the arrayed waveguide grating used for optical (de)multiplexing. This has many waveguiding channels in close proximity, each one carrying a slightly different wavelength. When considering the crosstalk performance of an optical (de)multiplexer, or any device with multiple waveguiding channels, the figure of merit is often the Optical Signal-to-Noise Ratio (OSNR) [97]. By injecting optical absorbing defects between two closely spaced SOI rib waveguides, it is anticipated that the noise in one waveguide, resulting from the optical power in the other, will be reduced. However, due to the change in the index profile induced by the defects, it is likely that radiation modes will cause the signal

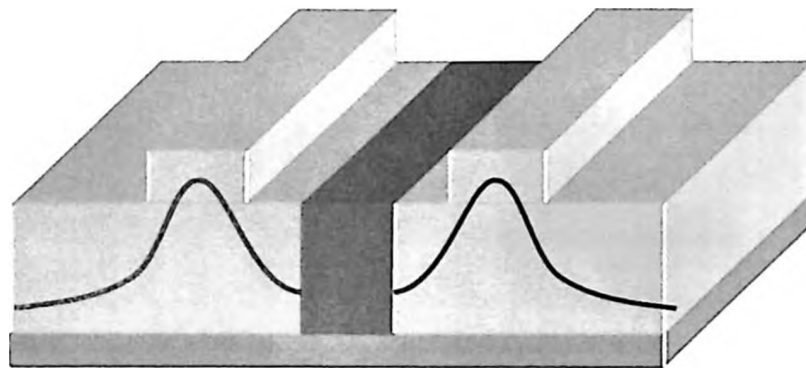


Figure 4.13: Design of an optical barrier between adjacent waveguides. The black region represents a volume of implantation-induced damage.

strength to reduce as well. For a well-designed optical barrier, the damage would be created to the full depth of the silicon overlayer, as illustrated in Fig. 4.13, in order to maximize absorption. The practicality of the defected volume, however, will depend on the OSNR of the adjacent waveguides. This will be a function of many parameters including the dimensions of the waveguides, the waveguide spacing, the width of the defected volume, and the implantation species, dose, and energy.

### 4.3.3 Directional Couplers

Since the real part of the index is increased, a volume of defects could potentially enhance the coupling between two waveguides. If the damaged region between the waveguides is made comparatively close to the device surface, then the optical power could radiate through the overlayer without extensive absorption. This concept is similar to the phenomenon observed in section 4.2.3, where radiation modes induced in the defected SOI rib waveguides caused the light to rapidly disperse in the slab. Fig. 4.14 illustrates a design possibility for utilizing this phenomenon in a directional coupler. In

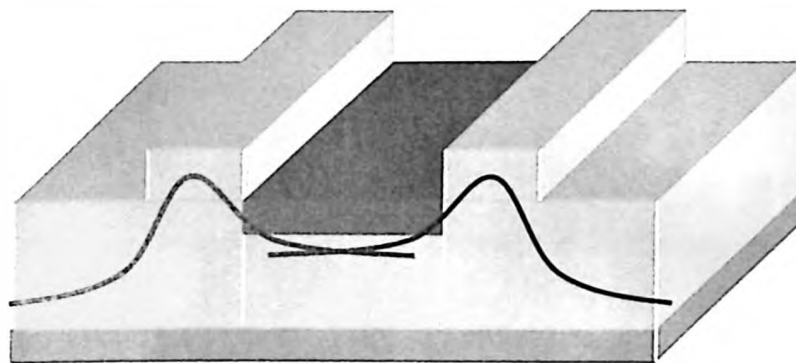


Figure 4.14: Design for enhanced coupling between adjacent waveguides. The black region represents a volume of implantation-induced damage.

this case, the damaged region would act mainly to increase the effective index of the overlayer between the waveguides, weakening their modal confinement. This would induce radiation loss from one waveguide and the optical mode would rapidly couple into the other, decreasing the natural coupling length. In this way, a defected volume in the silicon overlayer can be used to create much shorter directional couplers. Also, coupling between distant waveguides can be achieved with this sort of technique.

## Chapter 5

### Summary

#### 5.1 Characterization of Defects

Using a low energy positron beam along with the Doppler broadening technique, we have characterized bulk silicon samples irradiated with 2.8MeV Si<sup>+</sup> and others irradiated with 1.5MeV H<sup>+</sup>. These measurements indicated that the dominant vacancy-type defects were similar in size to divacancies and that their concentrations were consistent with those calculated using the CBK model. For the H<sup>+</sup> irradiated samples, the rate of defect accumulation with dose was found to have a sublinear dependence with an exponent of 0.66, close to the CBK value of 0.63.

By convolving the Makhov distribution for monoenergetic positrons with the normalized positron emission spectrum for radioactive <sup>22</sup>Na, we have modeled the implantation profile of positrons from <sup>22</sup>Na in close proximity to a silicon target. This model was successfully verified using PALS measurements performed on thinned silicon (down to a minimum of ~60μm) with copper backing in the bi-layer sandwich configuration. The experimental data were used to optimize the positron implantation model, which used upper and lower limit positron backscattering coefficients of  $\beta=0.354$  and  $\beta=0$ , respectively. It was shown that, for high energy positrons, the  $r$  parameter in the Makhov distribution is energy dependent and of the form  $r(T)=a+b\ln(T)$ . We have also suggested that our model is more accurate than the previously used exponential

model since it has a shallow peak (at a depth of approximately  $2\mu\text{m}$ ) and accounts for the underestimation of positron fractions absorbed in thin samples.

Using the positron implantation profile described here, PALS measurements were performed on the  $\sim 30\mu\text{m}$  thick defected layers created in the bulk silicon samples irradiated with  $1.5\text{MeV H}^+$ . A defect component lifetime of  $309\pm 11\text{ps}$  was found, corresponding to divacancies. The rate of defect accumulation with dose was found to have a sublinear dependence with an exponent of 0.64, similar to that measured using the positron beam. The actual divacancy concentrations were less than the predicted values, most likely due to defect-masking in the vicinity of the projected range of the protons. FTIR measurements further confirmed the existence of divacancies and the characteristic absorption band centered at  $1.8\mu\text{m}$ . Due to the broad width of this band, excess optical absorption at  $1.55\mu\text{m}$  was identified.

## 5.2 Defect-Engineered SOI Rib Waveguide Devices

We have described the effect of defect introduction via ion implantation on the optical loss in SOI rib waveguide structures for wavelengths around  $1.55\mu\text{m}$ . For waveguides fabricated using a silicon overlayer thickness of  $5\mu\text{m}$  and rib height of  $1.2\text{--}1.3\mu\text{m}$ , we were able to increase the optical attenuation to  $430\pm 15\text{dBcm}^{-1}$  using sub-amorphising self-ion implantation at an energy of  $2.8\text{MeV}$  and a dose of  $6.3\times 10^{13}\text{cm}^{-2}$ . The annealing response of the optical loss was consistent with that of the  $1.8\mu\text{m}$  band, found with FTIR measurements performed on bulk silicon. This suggests that the defect

primarily responsible for the optical attenuation at  $1.55\mu\text{m}$  in the SOI rib waveguides is the silicon divacancy.

Using  $\text{Si}^+$  irradiation of the waveguide structure described here, we have demonstrated that implantation energies approaching  $10\text{MeV}$  are necessary to achieve a complete overlap of the damage distribution with the fundamental optical mode. This may not be practical since it exceeds the capabilities of many ion implanters and necessitates the use of a  $\sim 9\mu\text{m}$  thick photoresist mask. However, as we advance towards sub-micron waveguide heights, the maximum  $\text{Si}^+$  energy is reduced to  $<600\text{keV}$ . Due to the incomplete damage/mode overlap, radiation effects were a major component of the total optical attenuation. Using a prediction of the refractive index change induced by the implantation, these radiation effects were simulated. The simulation demonstrated the mode evolution through the defected waveguides as being similar to actual images from an infrared camera. The absorption component of the total optical attenuation was predicted using a simple analytical expression based on the CBK model. This expression allows prediction of absorption for a wide range of implantation conditions such as ion species, ion energy and implantation dose. It was concluded that when designing a static attenuator, or any SOI device that utilizes optical absorbing defects, the optimal technique would be to use multiple implantation energies in an attempt to create a uniform concentration of defects throughout the silicon overlayer. In this fashion, the optical attenuation would be entirely due to the absorption component, and therefore radiation into other devices on the chip would not be an issue.

Finally, the practicality of using defect-engineered optical barriers was explored. It was suggested that such devices might be suitable for reducing optical noise between densely packed silicon photonic components. This may be a useful technique to improve the crosstalk performance of optical (de)multiplexers, which have many waveguiding channels in close proximity. The divacancy-related optical absorption was compared with free carrier absorption, indicating that a defect-engineered 10dB barrier with a width of 1000 $\mu\text{m}$  could be fabricated using an ion implantation dose two orders of magnitude lower. Also, high temperature activation of free carriers would not be required, benefiting the processing thermal budget.

## Bibliography

- [1] L. Eldada, *Review of Scientific Instruments*, **75**, 575 (2004).
- [2] R. A. Soref, *Silicon-based Optoelectronics*, *Proc. of IEEE*. **81**, 1687 (1993).
- [3] G. Reed and A. P. Knights, *Silicon Photonics: An Introduction* (John Wiley and Sons, New York, 2004).
- [4] L. Pavesi and D. J. Lockwood, *Silicon Photonics* (Springer-Verlag, Berlin, 2004).
- [5] D. Flandre, *Microelectronic Engineering*, **54**, 49 (2000).
- [6] S. G. Johnson, S. Fan, P. R. Villeneuve, J. D. Joannopoulos, and L. A. Kolodziejski, *Phys. Rev. B*. **60** 5751(1999).
- [7] M. Loncar, D. Nedeljkovic, T. Doll, J. Vuckovic, A. Scherer, and T. Pearsall, *Appl. Phys. Lett.* **77** 1937 (2000).
- [8] I. E. Day, A. A. House, J. Drake, and M. Asghari, *Proc. of NFOEC*. 943 (2001).
- [9] A. Liu, R. Jones, L. Liao, D. Samara-Rubio, D. Rubin, O. Cohen, R. Nicolaescu, and M. Paniccia, *Nature*, **427**, 615 (2004).
- [10] J. W. Corbett, J. P. Karins, and T. Y. Tan, *Nucl. Instrum. Methods Phys. Res.* **182**, 457 (1981).
- [11] E. C. Baranova, V. M. Gusev, Y. V. Martynenko, C. V. Starinin, and I. B. Haibullin, *Radiat. Eff.* **18**, 21 (1973).
- [12] H. Y. Fan and A. K. Ramdas, *J. Appl. Phys.* **30**, 1127 (1959).
- [13] Z. L. Wang, Q. T. Zhao, K. M. Wang, and B. R. Shi, *Nuclear Instruments and Methods in Physics*, **115**, 421 (1996).
- [14] E. Chason and S. T. Picraux, J. M. Poate, J. O. Borland, M. I. Current, T. D. delaRubia, D. J. Eaglesham, O. W. Holland, M. E. Law, C. W. Magee, J. W. Mayer, J. Melngailis, and A. F. Tasch, *J. Appl. Phys.* **81**, 6513 (1997).
- [15] D. C. Sawko and J. Bartko, *IEEE Trans. Nucl. Sci.* **30**, 1756 (1983).
- [16] W. L. Ng, M. A. Lourenco, R.M. Gwilliam, S. Ledain, G. Shao, and K. P. Homewood, *Nature*, **410**, 192 (2001).
- [17] A. P. Knights, A. House, R. MacNaughton and F. Hopper, *Proc. of OFC.* **2**, 705 (2003).
- [18] M. J. A. de Dood and A. Polman, *J. Appl. Phys.* **92**, 649 (2002).
- [19] R. G. Hunsperger, *Integrated Optics: Theory and Technology*, 5<sup>th</sup> edn. (Springer-Verlag, Berlin, 2002).
- [20] J. D. Plummer, M. Deal, and P. B. Griffin, *Silicon VLSI Technology* (Prentice Hall, Upper Saddle River, NJ, 2000).
- [21] R. A. Soref and B. R. Bennett, *IEEE Journal on Quantum Electronics*, **23**, 123 (1987).
- [22] P. G. Kik, A. Polman, S. Libertino, and S. Coffa, *J. Lightwave Tech.* **20**, 862 (2002).
- [23] A. P. Knights and G. F. Hopper, *Electronics Lett.* **39**, 1648 (2004).
- [24] L. J. Cheng, J. C. Corelli, J. W. Corbett, and G. D. Watkins, *Phys. Rev.* **152**, 761 (1966).

- [25] H. Kauppinen and C. Corbel, *Phys. Rev. B.* **55**, 9598 (1997).
- [26] A. Uedono, T. Mori, K. Morisawa, and K. Murakami, *J. Appl. Phys.* **93**, 3228 (2003).
- [27] R. Krause-Rehberg and H. S. Leipner, *Positron Annihilation in Semiconductors: Defect Studies* (Springer-Verlag, Berlin, 1999).
- [28] R. Scarmozzino, A. Gopinath, R. Pregla, and S. Helfert, *IEEE Journal of Selected Topics in Quantum Electronics*, **6**, 150 (2000).
- [29] B. E. A. Saleh and M. C. Teich, *Fundamentals of Photonics* (John Wiley and Sons, New York, 1991).
- [30] E. Hecht, *Optics*, 4<sup>th</sup> edn. (Addison-Wesley, San Francisco, 2002).
- [31] R. A. Soref, J. Schmidtchen, and K. Petermann, *J. Quant. Electron.* **27**, 1971 (1991).
- [32] R. Scarmozzino, A. Gopinath, R. Pregla, and S. Helfert, *IEEE Journal of Selected Topics in Quantum Electronics*, **6**, 150 (2000).
- [33] J. Nayyer, Y. Suematsu, and H. Tokiwa, *Opt. Quant. Electron.* **7**, 481 (1975).
- [34] P. K. Tien, *Appl. Opt.* **10**, 2395 (1971).
- [35] H. C. Huang and T. C. Lo, *J. Appl. Phys.* **74**, 1521 (1993).
- [36] A. Yariv, *Quantum Electronics*, 3<sup>rd</sup> edn. (Wiley, New York, 1989).
- [37] S. Somekh, *Theory, fabrication and performance of some integrated optical devices*, PhD Thesis, California Institute of Technology (University Microfilms, Ann Arbor, MI 1974) p. 46.
- [38] G. Dearnaley, *Ion Implantation*, (North-Holland Publishing Company, Amsterdam, 1973).
- [39] J. F. Ziegler, J. P. Biersack, and U. Littmark, *The Stopping and Range of Ions in Solids* (Pergamon, New York, 1985).
- [40] J. W. Corbett, *Solid State Physics Vol. 7.* (Academic, New York, 1966).
- [41] J. A. Brinkman, *J. Appl. Phys.* **25**, 961 (1954).
- [42] J. M. Haile, *Molecular Dynamics Simulations: Elementary Methods* (Wiley, New York, 1992).
- [43] G. H. Kinchin and R. S. Pease, *Rep. Prog. Phys.* **18**, 1 (1955).
- [44] K. B. Winterbon, P. Sigmund, J. B. Sanders, and K. D. Vidensk. Selsk. Mat. Fys. Medd. **37**, 14 (1970).
- [45] B. L. Crowder, R. S. Title, M. H. Brodsky, and G. D. Pettit, *Appl. Phys. Lett.* **16**, 205 (1970).
- [46] J. E. Westmoreland, G. W. Mayer, F. H. Eisen, and B. Welch, *Appl. Phys. Lett.* **15**, 3088 (1969).
- [47] S. T. Picraux, J. E. Westmoreland, J. W. Mayer, R. R. Hart, and O. J. March, *Appl. Phys. Lett.* **14**, 7 (1969).
- [48] S. U. Campisano, S. Coffa, V. Raineri, F. Priolo, and E. Rimini, *Nouv. J. Chim.* **80**, 514 (1993).
- [49] K. W. Wang, W. G. Spitzer, G. K. Hubber, and D. K. Sadana, *J. Appl. Phys.* **58**, 4553 (1985).
- [50] O. W. Holland, *Appl. Phys. Lett.* **54**, 320 (1989).
- [51] G. Bai and M. A. Nicolet, *J. Appl. Phys.* **70**, 649 (1991).

- [52] E. C. Baranova, V. M. Gusev, Y. V. Martynenko, and I. B. Haibullin, *Radiat. Eff.* **25**, 157 (1975).
- [53] O. W. Holland, D. Fathy, J. Narayan, and O. S. Oen, *Radiat. Eff. Defects Solids.* **90**, 127 (1985).
- [54] W. Jung and H. S. Nwell, *Phys. Rev.* **132**, 648 (1963).
- [55] H. J. Stein, F. L. Vook, and J. A. Borders, *Appl. Phys. Lett.* **14**, 328 (1969).
- [56] D. J. Eaglesham, P. A. Stolk, H. J. Gossmann, and J. M. Poate, *Appl. Phys. Lett.* **65**, 2305 (1994).
- [57] A. Claverie, B. Colombeau, F. Cristiano, A. Altibelli, and C. Bonazos, *Nucl. Instrum. Methods Phys. Res. B.* **186**, 281 (2002).
- [58] M. J. Caturla, T. D. de la Rubia, L. A. Marqués, and G. H. Gilmer, *Phys. Rev. B.* **54**, 16683 (1996).
- [59] P. G. Coleman, C. P. Burrows, and A. P. Knights, *Appl. Phys. Lett.* **80**, 947 (2002).
- [60] P. Kaminski, R. Kozłowski, and E. Nossarzewska-Orłowska, *Nuclear Instruments and Methods in Physics Research B*, **186**, 152 (2002).
- [61] M. Becker, Ph.D. thesis, Purdue University, 1951 (unpublished); M. Becker, H. Y. Fan, and K. Lark-Horovitz, *Phys. Rev.* **85**, 730 (1952); H. Y. Fan, *Repts. Progr. in Phys.* **19**, 107 (1956).
- [62] H. J. Stein, F. L. Vook, D. K. Brice, J. A. Borders, and S. T. Picraux, in the *Proceedings of First International Conference on Ion Implantation*, edited by L. Chadderton and F. Eisen (Gordon and Breach, New York, 1971), pp. 17–24.
- [63] M. Fukuzawa and M. Yamada, *Journal of Crystal Growth*, **229**, 22 (2001).
- [64] P. Asoka-Kumar, K. G. Lynn, and D. O. Welch, *J. Appl. Phys.* **76**, 4935 (1994).
- [65] A. P. Knights and P. G. Coleman, *Defects and Diffusion Forum*, **41**, 183 (2000).
- [66] S. Valkealahti and R. M. Nieminen, *Applied Physics A*, **32**, 95 (1983).
- [67] A. Vehanen, K. Saarinen, P. Hautojarvi, and H. Huomo, *Phys. Rev. B.* **35**, 4606 (1987).
- [68] V. J. Ghosh, *Appl. Surf. Sci.* **85**, 187 (1995).
- [69] J. Baker, N. Chilton, K. Jensen, A. Walker, and P. Coleman, *Journal of Physics: Condensed Matter.* **3**, 4109 (1991).
- [70] A. van Veen, H. Schut, J. de Vries, R. A. Hakvoort, and M. R. Ijpma, *AIP Conf. Proc.* **218**, 171 (1990).
- [71] P. Coleman, *Positron Beams and their Applications* (World Scientific Publishing, Singapore, 2000).
- [72] W. Brandt and R. Paulin, *Phys. Rev. B.* **5**, 2430 (1972).
- [73] W. Frank and A. Seeger, *Appl. Phys.* **3**, 66 (1974).
- [74] H. A. Enge, *Introduction to Nuclear Physics* (Addison-Wesley, Massachusetts, 1966).
- [75] C.D. Beling, R.I. Simpson, M. Charlton, F.M. Jacobsen, T.C. Griffith, P. Moriarty, and S. Fung, *Applied Physics A*, **42**, 111 (1987).
- [76] J. A. Baker, N. B. Chilton, and P. G. Coleman, *Appl. Phys. Lett.* **59**, 164 (1991).
- [77] P. Asoka-Kumar and K. G. Lynn, *Appl. Phys. Lett.* **57**, 1634 (1990).
- [78] J. Mahony, T. Friessnegg, G. Tessaro, P. Mascher, and W. Puff, *Applied Physics A*, **63**, 299 (1996).

- [79] I. K. MacKenzie, C. W. Shulte, T. Jackman, and J. L. Campbell, *Phys. Rev. A*, **7**, 135 (1973).
- [80] P. Coleman, L. Albrecht, K. Jensen, and A. Walker, *Journal of Physics: Condensed Matter*, **4**, 10311 (1992).
- [81] J. Mahony, M. Eng. Thesis, McMaster University, 1996 (unpublished).
- [82] W. Kern, *Handbook of Semiconductor Cleaning Technology* (Noyes Publishing, Park Ridge, NJ, 1993).
- [83] P. Kirkegaard, N. J. Pedersen, and M. Eldrup, *PATFIT-88: A Data Processing System for Positron Annihilation Spectra on Mainframe and Personal Computers* (Risø National Laboratory, Denmark, 1989).
- [84] W. Puff, *Comput. Phys. Commun.* **30**, 359 (1983).
- [85] M. Mourino, H. Lobl, and R. Paulin, *Phys. Lett. A*, **71**, 106 (1979).
- [86] A. P. Knights, F. Malik, and P. G. Coleman, *Appl. Phys. Lett.* **75**, 466 (1999).
- [87] M. Fujinami, R. Suzuki, T. Ohdaira, and T. Mikado, *Phys. Rev. B*, **58**, 559 (1998).
- [88] K. Murakami, K. Ishioka, M. Kitajima, S. Tateishi, K. Nakanoya, T. Mori, and S. Hishita, *Physica B*, **273**, 188 (1999).
- [89] T. Akiyama and A. Oshiyama, *J. Phys. Soc. Jpn.* **70**, 1627 (2001).
- [90] J. R. Ferraro and L. J. Basile, *Fourier Transform Infrared Spectroscopy: Applications to Chemical Systems* (Academic Press, Orlando, 1985).
- [91] R. A. Wind, H. Jones, M. J. Little, and M. A. Hines, *J. Phys. Chem. B*, **106**, 1557 (2002).
- [92] V. Gran'ko, F. F. Komarov, and A. V. Leont'ev, *Russian Microelectronics*, **31**, 4 (2002).
- [93] T. Sugano, *Applications of Plasma Processes to VLSI Technology*, (John Wiley and Sons, Rochester, 1985).
- [94] E. P. Eernisse, *Journal of Applied Physics*, **48**, 8 (1977).
- [95] M. Ohring, *Materials Science of Thin Films*, (Academic Press, Pittsburgh, 1992).
- [96] L. J. Cheng and L. Lori, *Phys. Rev.* **171**, 856 (1968).
- [97] X. Lin and L. Yan, *IEEE Photonics Technology Letters*, **16**, 2637 (2004).